

Continuous fluidized bed crystallization

Dissertation
zur Erlangung des akademischen Grades

Doktoringenieur
(Dr.-Ing.)

von Dipl. Chem. Daniel Binev
geb. am 09.11.1975 in Pleven, Bulgarien

genehmigt durch die Fakultät für Verfahrens- und Systemtechnik
der Otto-von-Guericke-Universität Magdeburg

Promotionskommission: apl. Prof. Dr. Heike Lorenz (Vorsitz)
Prof. Dr.-Ing. Andreas Seidel-Morgenstern (Gutachter)
Prof. Dr.-Ing. Ulrich Teipel (Gutachter)
Prof. Dr.-Ing. Stefan Heinrich (Gutachter)

eingereicht am: 03.11.2014

Promotionskolloquium am: 30.01.2015

Schriftliche Erklärung

Ich erkläre hiermit, dass ich die vorliegende Arbeit ohne unzulässige Hilfe Dritter und ohne Benutzung anderer als der angegebenen Hilfsmittel angefertigt habe.

Die aus fremden Quellen direkt oder indirekt übernommenen Gedanken sind als solche kenntlich gemacht.

Insbesondere habe ich nicht die Hilfe einer kommerziellen Promotionsberatung in Anspruch genommen. Dritte haben von mir weder unmittelbar noch mittelbar geldwerte Leistungen für Arbeiten erhalten, die im Zusammenhang mit dem Inhalt der vorgelegten Dissertation stehen.

Die Arbeit wurde bisher weder im Inland noch im Ausland in gleicher oder ähnlicher Form als Dissertation eingereicht und ist als Ganzes auch noch nicht veröffentlicht.

Magdeburg, _____

(Unterschrift)

Abstract

In this work, systematic studies on the continuous crystallization were conducted in a fluidized bed crystallizer. The impact of the inlet flow rates on the crystal size distributions was studied under the influence of a continuous generation of seed crystals using ultrasound (US). The experiments were conducted with three industrially relevant substances (fine chemicals) in a newly developed pilot-plant setup, featuring a conical shaped fluidized bed crystallizer possessing seven outlets. These substances differ in their crystal shape and in other essential chemical and physical properties (e.g. solubility equilibria, metastable zone widths etc.). By changing the inlet fluid flow rate, the desired crystal size distribution was shifted and eventually concentrated to a certain product outlet position. The size of the product crystals could be significantly influenced by the sizes of the initially added seed crystals. The application of US to trigger de-agglomeration and to provide seeds by crystal breakage was used as an alternative to the classical application of wet milling. A pilot-plant setup comprising two coupled fluidized bed crystallizers was constructed. In this pilot-plant unit continuous selective (“preferential”) crystallization of two ternary systems was performed successfully.

In order to quantify the process in steady state, a Richardson-Zaki force balance model and a simplified dynamical population balance model were formulated and applied. The first model allows estimating average positions of a particle with respect to the height of the fluidized bed. It is limited only to constant particle diameters. The simplified dynamic model does not only provide information with respect to the fluidization of the particle but provides full particle number distribution at every time and position in the fluidized bed crystallizer.

Primarily, the thesis provides a proof of concept and a feasibility study regarding the application of two coupled fluidized bed crystallizers for kinetically controlled continuous selective crystallization in the metastable region of the phase diagram of the components of interest.

Kurzzusammenfassung

In dieser Arbeit wurden systematische Untersuchungen zur kontinuierlichen Kristallisation in einem Wirbelschichtkristallisator durchgeführt. Der Einfluss des Einlassvolumenstroms der fluiden Phase auf die Kristallgrößenverteilung kontinuierlicher Erzeugung von Impfkristallen mit Ultraschall (US) wurde untersucht. Die Versuche erfolgten mit drei industriell relevanten Substanzen (Feinchemikalien) in einer in Rahmen dieser Arbeit aufgebauten Pilotanlage. Herzstück der Anlage ist ein konusförmiger Wirbelschichtkristallisator, der mit sieben Produktauslässen ausgestattet ist. Die untersuchten Substanzen unterschieden sich in ihrer Kristallform und in anderen wichtigen chemischen und physikalischen Eigenschaften (z.B. Löslichkeitsgleichgewichte, metastabile Zonen etc.). Durch Veränderung der Durchflussrate konnte die Kristallgrößenverteilung verschoben und an bestimmten Produktauslass-positionen konzentriert werden. Die Größe der Produktkristalle wurde wesentlich durch die Größe der am Anfang zugegebenen Impfkristalle beeinflusst. Der Einsatz von US konnte erfolgreich für die De-Agglomeration und die Kristallzerkleinerung als Alternative zur klassischen Anwendung der Nassvermahlung demonstriert werden. Eine weitere Pilotanlage wurde konstruiert, die mit zwei gekoppelten Wirbelschichtkristallisatoren ausgestattet wurde. In dieser Anlage konnte eine kontinuierliche selektive („bevorzugte“) Kristallisation von einem chiralen und einem achiralen ternären Systemen erfolgreich durchgeführt.

Um den Prozess im stationären Zustand quantitativ zu beschreiben, wurden das auf Kräftebilanzen basierende Richardson-Zaki-Modell und ein vereinfachtes dynamisches Populationsbilanzmodell formuliert und eingesetzt. Ersteres ermöglicht die Vorhersage der Position eines Teilchens mit einer bestimmten Größe in der Wirbelschicht, ist aber auf konstante Partikeldurchmesser begrenzt. Das detailliertere dynamische Modell erlaubt Aussagen bezüglich der Fluidisierung der Partikel und Vorhersagen zur Partikelanzahlverteilung zu jeder Zeit und an jeder Höhe im Wirbelschichtkristallisator.

Wesentliches Ergebnis dieser Arbeit ist ein „Proof of Concept“ bezüglich der Anwendung von zwei miteinander gekoppelten Wirbelschichtkristallisatoren für die kinetisch kontrollierte, kontinuierliche selektive Kristallisation zweier Komponenten in metastabilen Bereich des Phasendiagramms.

Acknowledgements

This thesis was done during my work at the Max Planck Institute for Dynamics of Complex Technical Systems in Magdeburg in the period 15.09.2009 – 30.08.2014.

Several people have contributed to the success of this work. At first I would like to thank Professor Andreas Seidel-Morgenstern for offering me a research position at the institute and for his support in many ways throughout the years. Also I appreciate a lot his trust in my capabilities.

Further on I would like to thank Dr. Heike Lorenz for many fruitful discussions, inspiring ideas and support throughout my entire work.

Most of the work done would have been impossible without the support of our lab technicians Jacqueline Kauffmann, Luise Borchert and Stefanie Leuchtenberg who helped a lot during the experimental part of this work. A great part of the experiments used in the final version of the thesis have been carried out by students. I would like to thank Kathrin Würfel and Tenyo Kolev for providing valuable results and ideas for this work and wish them all the best.

I would like to thank the people from the IT department, mechanical and electronic workshops for their support throughout the years.

Additionally I would like to thank all the people from our lunch group for the inspiring and stimulating discussions.

At the end I would like to thank my parents, my sister and my girlfriend for their constant support in many ways during my time in Magdeburg.

This list will never be completed so I would like to thank all other people not mentioned explicitly here who contributed to this work and made my time in Magdeburg a pleasant and thrilling experience.

Table of Contents

1. Introduction	1
2. Theoretical background	4
2.1 Crystallization as a process to separate mixtures	4
2.1.1 Thermodynamics: Solubility equilibria	5
2.1.1.1 Solubility phase diagrams	5
2.1.1.2 Supersaturation, metastable zone and supersaturation	11
2.1.2 Crystallization kinetics	14
2.1.2.1 Nucleation	14
2.1.2.2 Crystal growth	16
2.1.3 Polymorphism	19
2.1.4 Cooling crystallization	19
2.1.4.1 Batch crystallization	20
2.1.4.2 Continuous crystallization	21
2.1.5 Seeding	23
2.2 Enantiomers and their isolation	25
2.2.1 Enantiomers and racemic mixtures	25
2.2.2 Preferential crystallization of simple eutectic systems	29
2.2.2.1 Preferential crystallization in a batch crystallizer	30
2.2.2.2 Continuous preferential crystallization in coupled crystallizers	32
2.3 Crystallization in fluidized bed	35
2.3.1 Principle and hydrodynamics	35
2.3.2 Segregation	37
2.3.3 Application	38
2.3.4 Force balance model for evaluation of particle position	42
3. Experimental	49
3.1 Selected model compounds	49
3.1.1 Glutamic acid	49
3.1.2 Asparagine monohydrate	51
3.1.3 Aminobenzoic acid	53
3.2 Methods, procedures and experimental setups	54
3.2.1 Preliminary experiments	55
3.2.1.1 Solubility equilibria and metastable zone width	55

3.2.1.2 Seed preparation by sieving.....	57
3.2.1.3 Ultrasound-forced breakage of crystals	57
3.2.2 Experiments in single fluidized bed crystallizer	59
3.2.2.1 Equipment used and description of the process.....	59
3.2.2.2 Crystal size distribution measurements	62
3.2.3 Experiments in coupled fluidized bed crystallizer	64
3.3 Analytical techniques	67
4. Results and discussion.....	80
4.1 Simplified dynamic model of the fluidized bed crystallization process	80
4.2 Solubility equilibria and metastable zone width determination	86
4.3 Generation of seeds by ultra-sonication	99
4.4 Experiments in a single fluidized bed.....	102
4.4.1 Influence of selected parameters on the crystal size distribution	102
4.4.1.1 Influence of the feed flow rate.....	103
4.4.1.2 Influence of the ultrasound seed generation	105
4.4.1.3 Influence of the various seed sizes.....	107
4.4.1.4 Comparison with the Richardson-Zaki force balance model	110
4.4.2 Temporal approach to steady state operation	117
4.4.3 Summary	119
4.5 Experiments in two coupled fluidized beds	120
4.5.1 Continuous crystallization of aminobenzoic acid stereomers	121
4.5.2 Continuous crystallization of asparagine enantiomers	129
4.5.3 Summary	134
4.6 Equipment based recommendations	135
5. Conclusions	138
References.....	142
Nomenclature	151
Appendices	156

1. Introduction

Both in the chemical and in the pharmaceutical industry, crystallization is a proven method of product purification and product design. Product properties such as the purity of the crystals, the crystal size distribution and the crystal habit are thereby significantly influenced by the crystal growth process. Hence crystal growth in the presence of impurities is for several decades an important issue in crystallization research. Moreover the impurities affect not only the crystal purity, but have in general significant influence on the substance properties and the crystal habit. In medicine it has been known for some time that two enantiomeric forms of a chiral substance may have completely different pharmacological effects when administered to living organisms. Often the enantiomer with the desired physiological impact has a "mirror image" showing no effect or even being harmful. Therefore enantiomers with high purity are becoming more and more important for pharmaceutical products needed to have the desired medical effect and to minimize the undesirable side effects. Hence the research should be emphasized on the direct production of pure enantiomers. This can be done for example through synthesis of only one of the two enantiomeric forms, or by the separation or purification of racemic or non-racemic mixtures. Moreover the strong similarity of the two enantiomers at molecular level and possible interactions between the two isomers (especially for chiral compound-forming systems) make their purification a special case of the enantioselective crystallization process. For a certain type of them and especially conglomerate-forming systems a rather straightforward technique can be applied. Usually the crystal production is batch-wise realized, where the crystallization process is kinetically determined [Myerson2002, Hoffman2005]. Hence for conglomerate-forming systems a novel technique of this process can be applied by coupling together two batch-crystallizers and while exchanging the mother liquor between them, simultaneously yielding both enantiomers [Elsner2007, Elsner2009, Elsner2011].

One of the possible ways to increase productivity and quality of the product while maintaining a continuous crystallization process is to use fluidized bed

crystallizers. The performance of such separation process is elaborated and technically proved with some industry relevant amino acid systems, forming simple eutectic [Midler1975, Midler1976]. The process concept is based on the idea that a defined quantity of crystals, placed under appropriate conditions inside a fluidized bed crystallizer, behaves as a fluid due to the uprising solution flow. To keep the continuity of the process, seeds have been constantly generated by ultrasonic comminution of the crystals at the bottom of the crystallizer. Despite the increasing number of publications on crystallization-based enantioseparation, the crystallization in fluidized bed in general is little studied so far and in particular there is lack of enough quantitative experimental data needed to create a general conceptual model [Perry1997, Tai1999, Mullin2001, Yang2003, Epstein2003, Tung2009]. However, acquiring more experimental data could permit in connection with the knowledge of the appropriate thermodynamic data to optimally design and control the enantioselective crystallization process from the point of productivity and product quality. Motivated by this knowledge gap, it is the intention of this study, based on systematic study of some chiral model systems and through targeted enantioselective crystallization to extend the knowledge by contributing to this topic.

The objectives of this thesis are to demonstrate and evaluate crystallization process, where product crystals with high purity and tight crystal size distributions are continuously and robustly obtained by maintaining a fluidized bed crystallizer in a steady state regime. Moreover, the “proof of principle” of the kinetically controlled continuous selective preferential crystallization process should be demonstrated in two coupled fluidized bed crystallizers for selected ternary systems. In order to run the process continuously, the necessary seeds provision should be by a fragmentation of already grown crystals externally of the crystallizer using ultrasonic comminution.

The thesis is structured as follows:

In the following chapter 2, a theoretical background is given, concerning all aspects relevant for this thesis. Along with an introduction to enantiomers and racemates, the crystallization basics are summarized. This includes solubility equilibria and crystallization kinetics, the production of single enantiomers using

crystallization and preferential crystallization in particular. Another section is dedicated to special crystallization techniques available for increased recovery of enantiomers like continuous crystallization in single and coupled batch crystallizers. The chapter is concluded with the principle of the fluidized bed and its application, where in detail the crystallization mechanism along with a basic scheme and the simple force balance model of the process are illustrated.

In chapter 3, the experimental and characterization techniques and methods as well as the experimental and analytical setups used are described. The first part of the chapter includes a description of the model substances used, followed by preliminary experiments on their solubility and MSZW. A novel fluidized bed reactor setup is introduced with a detailed description of its operational parts. The operating conditions of the single fluidized bed crystallizer are then described along with the initial start-up. Further, information is provided about the construction of the second more advanced experimental setup, featuring two coupled fluidized bed crystallizers. In the last part of the chapter, a description of the analytics used is given along with the corresponding experimental conditions.

The results of the experiments and their detailed discussion are comprised in chapter 4. Before this, in the beginning of the chapter, a simplified dynamical population balance model is introduced, which combines crystallization kinetics with fluidization process. In the preliminary experiments given afterwards, the solubility and metastable zone widths of the model substances are given as well as results regarding the generation of seeds by ultra-sonication. Further in chapter 4.4, results from the influence of selected parameters on the crystal size distribution in the single fluidized bed crystallizer are presented. A comparison of the collected experimental results is made with the results from the introduced in chapter 2.3.4 simple force balance model. An experimental “proof of principle”, comprising the continuous preferential crystallization of two ternary systems in two coupled fluidized bed crystallizers, is provided in chapter 4.5.

Finally, concluding remarks and recommendations are given in chapter 5.

2. Theoretical background

The object of this chapter is to outline some important aspects of the crystallization theory and practice, along with some relevant topics, emphasizing some special chiral substances and their purification. Particular attention has been paid to recently developed processing methods, including some, yet to be proved adaptable to the large-scale production of crystals.

2.1 Crystallization as a process to separate mixtures

The need for efficient high-throughput techniques for the production of pure compounds is growing in conjunction with the increasing structural complexity of new drug molecules. Hence, the identification and characterization of the different kinetic phenomena in the crystallization process, e.g. solubility of the substance, nucleation or polymorphism, is relevant for process understanding. Moreover, an adequate process modelling gives the possibility to optimize and control the crystallization process, thus allowing robust operations and appropriate process design.

Crystallization is a solubility-related process and it represents one of the basic processes in the process engineering. That is, a solid crystal or precipitate is formed when a solute exceeds its solubility in the solution. The crystallization refers also to the separation of solid, crystalline phases from melts or gases. Some thermal processes, which involve crystallization, are separation of mixtures of substances, purification of materials, recovery of solvents or concentration of solutions. The diversity of the crystallization processes is due to the variety of material systems, operating conditions and product specifications, such as crystal purity, crystal size distribution, and crystal shape.

The most important mechanisms of crystallization are nucleation and crystal growth. Moreover, agglomeration and breakage of crystals are two crucial factors in addition to them. Frequently, cooling crystallization is applied as crystallization technique and for this reason it will be discussed in detail. Furthermore, fluidized beds have been applied successfully. Their principle will be also explained below.

2.1.1 Thermodynamics: Solubility equilibria

2.1.1.1 Solubility phase diagrams

The solubility equilibrium represents the thermodynamic equilibrium between a liquid and a solid phase. The equilibrium states are represented in phase diagrams. The latter describe the equilibrium and represent the pressure and temperature dependence of the solubility equilibria on the composition. The binary solution system consists of a solid component to be dissolved and a solvent, preferably water. The curve in a phase diagram is the dependence of the solution composition of a given substance at a specific pressure on the temperature. The diagrams have a different waveform depending on the miscibility in the liquid or in the solid state [Predel1982].

- Binary phase diagrams

The thermal state of one-component systems is completely described through three variables: volume or density, pressure and temperature. In two-component systems (AB) another variable is added - the composition of the system. This can be expressed by the mole fraction or weight percentage of the components A and B. Shown are the equilibrium conditions in phase diagrams, the so called melt or solubility diagrams. These represent the solid and liquid phases which are in equilibrium as a function of the temperature at a specific pressure. In a two-component system, only the mole input of just one component is necessary for the total mole fraction.

$$\chi_A = 1 - \chi_B \quad (2.1)$$

In eq. 2.1, χ_A is the mole fraction of a component A and χ_B - the mole fraction of component B. The mole fraction χ_A of the component A in system with N components can be calculated using the following equation.

$$\chi_A = \frac{n_A}{\sum_i^N n_i} \quad (2.2)$$

In eq. 2.2, n_A is the molar amount of component A and $\sum_i^N n_i$ is the sum of the molar amounts of all N components i [Mullin2001]. The representation of the

Ch. 2 | Theoretical background

phase diagrams is based on the Gibbs' phase rule, which determines the number of degrees of freedom, i.e. the number of independent variables.

$$P + F = C + 2 \quad (2.3)$$

In eq. 2.3, P represents the number of phases, F is the number of degrees of freedom, and C is the number of independent components. Since the binary systems, involved in the crystallization processes, usually have a pressure of one atmosphere (1 atm), which can be considered constant, the phase rule can be rewritten:

$$F = C - P + 1 \quad (2.4)$$

For binary mixtures of two chemically independent components, $C = 2$ so that $F = 3 - P$. In a single phase ($P = 1$) condition of such two-component system, two variables ($F = 2$), such as temperature and composition, can be chosen independently to be any pair of values consistent with the phase. However, if the temperature and composition combination ranges to a point where the homogeneous one phase system undergoes a separation into two phases ($P = 2$), F decreases from 2 to 1. When the system enters the two-phase region, it becomes no longer possible to independently control temperature and composition. The phase diagrams differ depending on the miscibility of the components in the solid or liquid state and the type of composition of the resulted solid phases. Based on that, there are a number of different types of phase diagrams representing different cases.

In fig. 2.1 are shown the most important two-component systems, which are completely miscible in the liquid phase [Beckmann2013]. In the diagrams the pure components are indicated as A and B, a solution as AB, and mixed crystals as A_xB_y or B_xA_y .

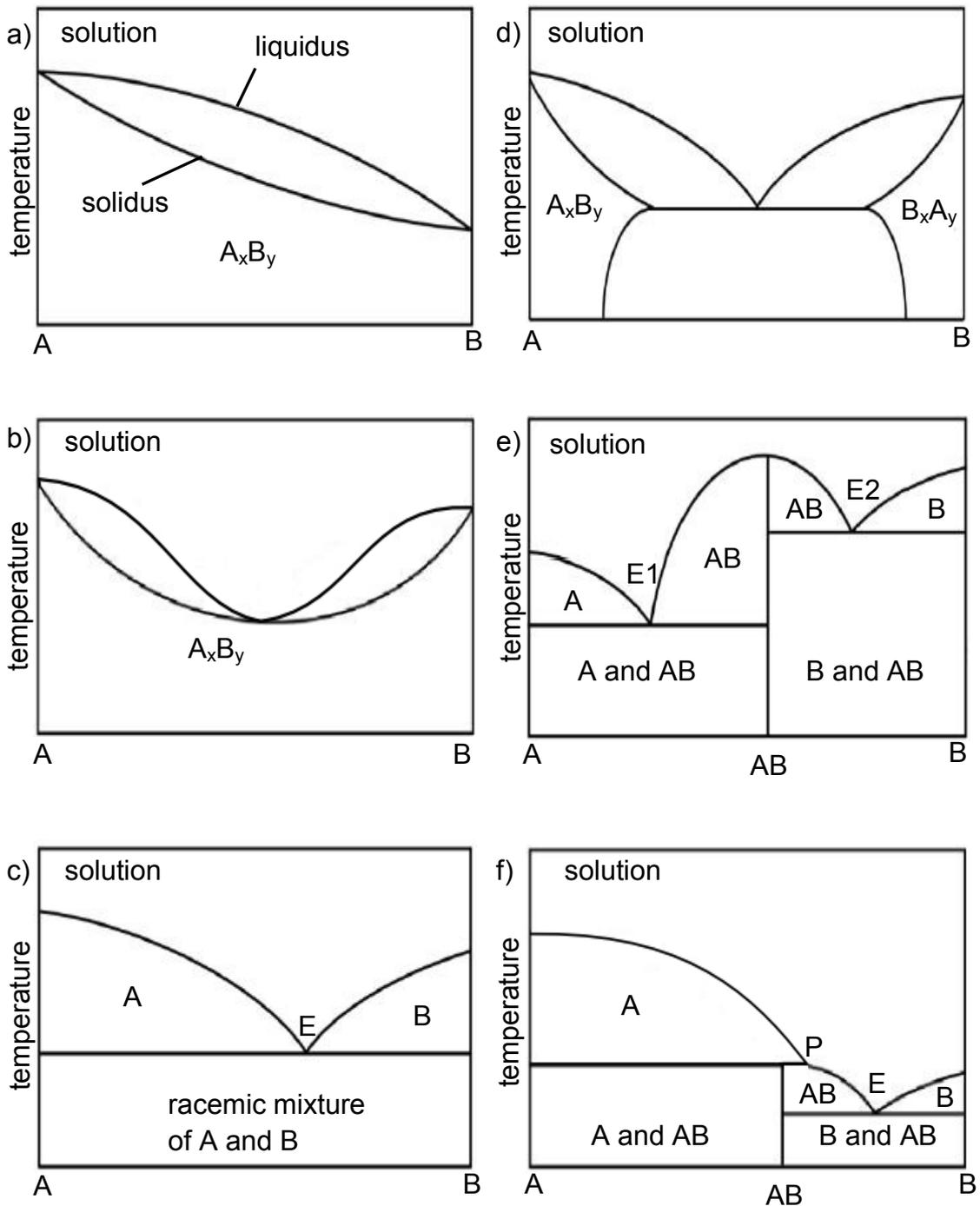


Fig. 2.1 A representation of the most common binary melt phase diagrams: a) complete solid solution; b) solid solution with a minimum; c) eutectic; d) partial solid solution with eutectic; e) compound-forming with eutectic; f) compound-forming with peritectic. Adapted from [Lorenz2013].

In fig. 2.1a, the phase diagram represents a complete solid solution formation. Depending on the degree of cooling, mixed crystals with different composition of the two components can be formed. If the temperature is quickly lowered,

Ch. 2 | Theoretical background

inhomogeneous solid solution crystals are formed, which have a concentration gradient in their structure from inside to the outside. On the contrary, homogeneous solid solution crystals can be formed by slowly cooling the solution, because of the balanced concentration differences during the cooling process. Besides this simple case, phase diagrams can have maximums or minimums. In Fig. 2.1b, a diagram is shown that includes a minimum. Here the diagram is formally divided into two areas of the type as in Fig. 2.1a. The solution solidifies at the shown minimum as mixed crystals without changing the composition.

In Fig. 2.1c is shown a system having a complete miscibility in the liquid state and a complete immiscibility in the solid state. This complete miscibility gap creates an eutectic, denoted with point E in the diagram. The characteristic feature here is that no mixed crystals are formed, but the components A and B are present in the solid state as a heterogeneous mixture. In the two areas marked as A and B, pure components A or B respectively are formed during the cooling process until the point where the two solubility curves intersect the eutectic line. A mixture of crystals of both components forms at this boundary line with the eutectic composition.

Systems considering complete insolubility in the solid state practically hardly occur. Predominantly, eutectic systems can be found having high or low solubility of the two components into one another. This very common system is shown in Fig. 2.1d. In the solid state, the system has a miscibility gap. In the considered single-phase regions of the phase diagram mixed crystals of types A_xB_y and B_xA_y ($x > y$) are formed. Furthermore, between the two single-phase regions, there is a miscibility gap region, where a heterogeneous mixture of the mixed crystals of A_xB_y and B_xA_y occur.

Only pure components or mixed crystals as solid phases appear in the systems considered so far. However, the two components can often form one or more chemical compounds together. Such phase diagram with compound-formation (shown as AB) is shown in Fig. 2.1e. The diagram can be formally seen as it consists of two phase diagrams of type, shown in fig. 2.1c.

If a phase transformations takes place in the system, at least one of the phases will experience a change in the composition, whereby the composition of the

solute in solution does not match that of the solid. This incongruent transformation happens at the so-called peritectic point, denoted by P in the Fig. 2.1f. At this point, the composition of the solid phase and the dissolved solute does not stoichiometrically match [Beckmann2013].

- Ternary phase diagrams

The phase equilibria in ternary systems can be affected by four variables – temperature, pressure and the concentration of any two of the three components. This fact can be deduced from the Gibbs phase rule.

$$P + F = 3 + 2 \tag{2.5}$$

Thus, a one-phase ternary system will have four degrees of freedom. In order to represent it graphically on an equilateral triangular diagram, the pressure should be considered constant. An exemplarily ternary phase diagram is shown on Fig. 2.2.

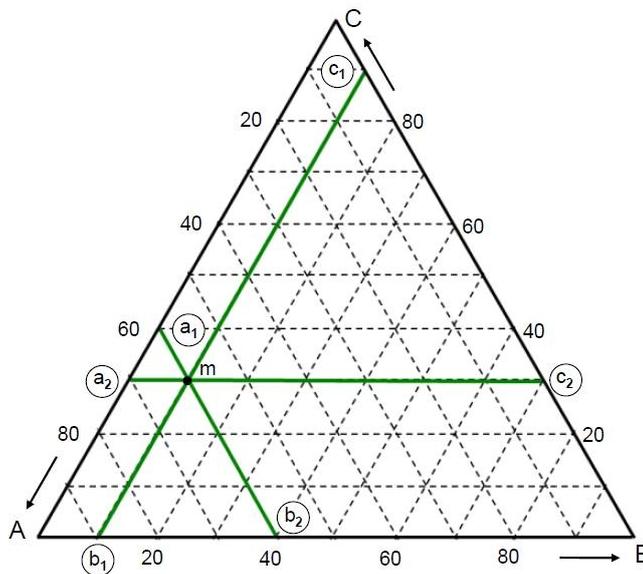


Fig. 2.2 An exemplarily ternary phase diagram with an intersection point m, representing the composition of the three substances A, B and C in isothermal equilibria.

The vertices of the triangle represent the pure components A, B and C. The points on the side of the triangle stand for binary systems – AB, BC and AC, while the point m within the triangle represents a ternary system ABC. The scales of the component concentration can be any convenient unit, e.g. mass

Ch. 2 | Theoretical background

percentage, like in the example shown. The composition of the whole system is defined by specifying at least two compound concentrations and for the third compound applies the rule:

$$\chi_A + \chi_B + \chi_C = 100 \quad (2.6)$$

Generally, the parallel lines to the sides of the triangle correspond to a constant concentration of the component on the opposite triangle corner, e.g. lines a_1b_2 , b_1c_1 and a_2c_2 . The percentage composition of a mixture can thus be based on the intersection point determined by two lines. This intersection corresponds to the mixing point of the three components. In the case from fig. 2.2, M consists of 60% of component A, 10% of component B, and 30% of component C [Mullin2001].

Usually in a ternary phase diagram, a representation of only one temperature is considered, thus it corresponds to an isothermal section, although plotting of more isotherms is sometimes useful, especially when comparing solubility equilibria at different temperatures.

A special case of the ternary solubility phase diagrams, found for most of the enantiomeric systems, is shown schematically in figure 2.3 [Roozeboom1899]. The diagrams represent a mixture of two enantiomers (D and L) added in a solvent (S) at a constant pressure and temperature. More information about enantiomers can be found in section 2.2.

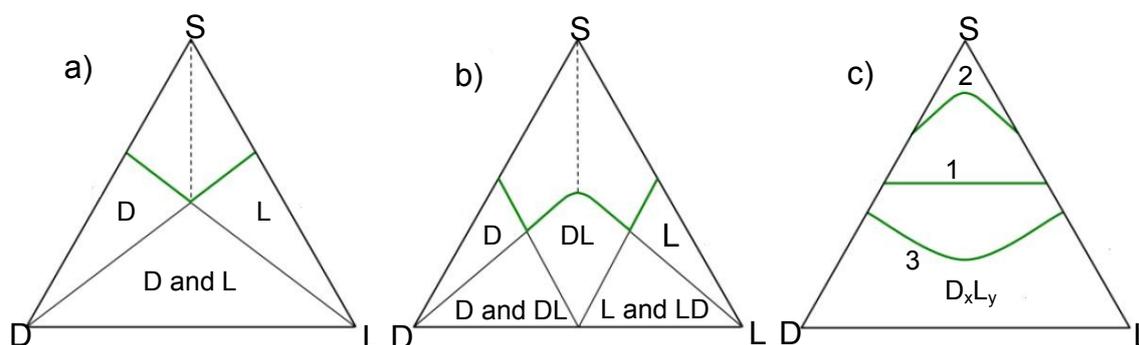


Fig. 2.3 Ternary solid-liquid phase diagrams of chiral systems, where liquidus is shown in green: a) conglomerate-forming; b) compound-forming; c) solid solution-forming, where 1 – for ideal system, 2 – system with a solubility minimum, 3 – system with a solubility maximum [adopted from Sistla2011].

Depending on the chiral system in the ternary phase diagram, various two- or three-phase regions are located below the solubility isotherms (shown in green), while a one-phase region is located above the solubility isotherms. In these multiphase regions various stable crystalline phases can be seen. The pure enantiomers (D and L) and pure solvent (S) correspond to the triangle vertices and the points on the side of the triangle edges correspond to binary mixtures DS, LS and DL. The one-phase region is located above the solubility isotherms in all three diagrams. Here, the existing solutions are undersaturated with respect to the components L and D. Conglomerate-forming systems are shown in Fig. 2.3a and represent the formation of crystal mixtures having a racemic composition. In comparison, by the compound-forming systems (shown in Fig. 2.3b) crystals from racemic compounds DL are formed as well. In addition, there are two eutectic points. The third diagram, shown in Fig. 2.3c, represents a complete solid solution formation. Here, both enantiomers integrate into the crystal lattice regardless of their mixing ratio. Solid solution formation occurs as an ideal system (line 1 in Fig. 2.3c), a system with solubility minimum (curve 2) and a system having a maximum solubility (curve 3).

2.1.1.2 Supersaturation, metastable zone and supersaturation

Solubility is the property of a solid, liquid, or gaseous chemical substance called solute to dissolve in a solid, liquid, or gaseous solvent to form a homogeneous solution of the solute in the solvent [Hill1999]. The solubility of a substance fundamentally depends on the physical and chemical properties of the used solute and solvent as well as on temperature, pressure and the pH of the solution. The extent of the solubility of a substance in a specific solvent is measured as the saturation concentration, where adding more solute does not increase the concentration of the solution and begin to precipitate the excess amount of solute. Most often, the solvent is a liquid, which can be a pure substance or a mixture. Solubility is commonly expressed as a concentration, which may have units of mass percent, g/l, molality, mole fraction, mole ratio, and other. The solubility of a given solute in a given solvent typically depends on temperature. For many solids dissolved in liquid water, the solubility increases with temperature up to 100 °C [Hill1999]. This is especially valid for the

dissolution of solid organic compounds. A few exceptions exist, such as certain cyclodextrins, which possess a negative solubility coefficient (higher temperature decreases the solubility) [Filippone2002, Plazanet2006].

There are three possible conditions inside a solution, distinguished by the dissolution ratio of the solid. The condition, which corresponds to an undersaturated solution, is the case when the concentration of the solute is less than its solubility in the solvent at a specified temperature. A saturated solution is achieved when the concentration corresponds to the maximum solubility and a thermodynamic equilibrium at the specified temperature is established. The latter is reached when the substance to be dissolved in the solvent can no more dissolve. However, if the temperature is lowered, than the solubility of the solute is lowered and as a consequence the concentration becomes greater than represented by the equilibrium saturation. At these conditions, the solution is supersaturated. A diagram, representing the possible conditions in a solution is depicted in fig. 2.4.

The supersaturation of the system is the driving force and is therefore crucial for crystallization. It can vary depending on temperature difference, by evaporation of solvent or by addition of other soluble substances. The degree of supersaturation is dependent on the crystallization kinetics and properties of the material, such as nucleation and crystal growth, as well as energy and material transfer. The crystallization kinetics is introduced separately in section 2.1.2.

The saturation and supersaturation are concentration dependent and are strongly influenced by the temperature. This means that a saturated liquid phase at a certain temperature is in the thermodynamic equilibrium to a certain concentration with a solid phase.

Among the most common expressions of supersaturation are the concentration driving force (Δc), the supersaturation ratio (S) and the relative supersaturation (σ). These quantities for a component i are defined by:

$$\Delta c_i = c_i - c_i^* \quad (2.7)$$

$$S_i = \frac{c_i}{c_i^*} \quad (2.8)$$

$$\sigma = \frac{\Delta c_i}{c_i^*} = S - 1 \quad (2.9)$$

where c_i is the solution concentration of the component i , and c_i^* is the equilibrium concentration of the component i at the given temperature. Of the above three expressions for supersaturation only Δc is dimensional, unless the solution composition is expressed in mole fraction or mass fraction. It is very important to quote the temperature, since the equilibrium saturation concentration is temperature dependent. For practical purposes, supersaturation is generally expressed directly in terms of solution concentration (e.g. molarity (mol / l) or molality (mol / kg)).

The state of supersaturation is one of the essential requirements for all crystallization operations. Ostwald first introduced the terms “labile” and “metastable” solution in 1897, while Miers and Isaac represented diagrammatically the metastable zone on a solubility-supersolubility diagram, see Fig. 2.4 [Mullin2001].

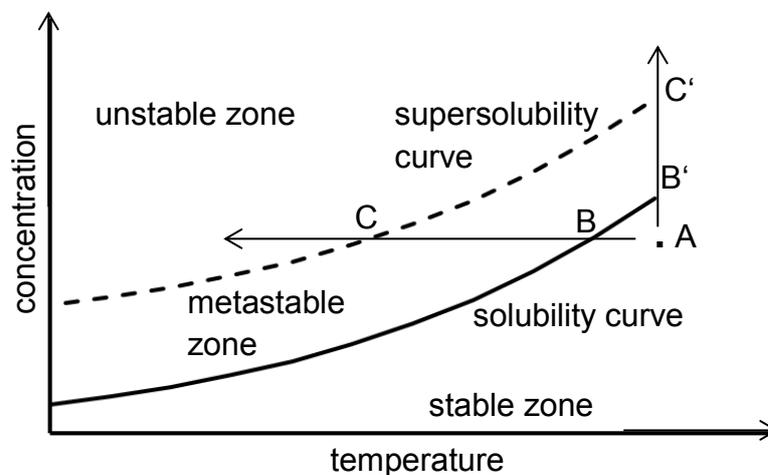


Fig. 2.4 The solubility diagram with an illustration of the metastable zone [adapted from Jones2002].

In the diagram two curves are shown, forming the borders of the metastable zone. The lower continuous curve represents the solubility of the given substance, while the upper broken curve, also called supersolubility curve, represents temperatures and concentrations at which spontaneous crystallization occurs. The latter is not well defined and is affected by, amongst other things, the rate at which supersaturation is generated, the intensity of agitation and the

presence of impurities. The diagram can be therefore divided into three zones [Jones2002]:

1. Stable (undersaturated) zone, where no crystallization could occur and if seed crystals of the substance are introduced into solution, then they are dissolved.
2. Metastable (supersaturated) zone, which lies between the solubility and supersolubility curve, where spontaneous crystallization is improbable, although secondary and primary heterogenic nucleation could happen. If seed crystals are introduced into solution, then they will grow.
3. Unstable or labile zone above the supersolubility curve, where spontaneous crystallization (or nucleation shower) occurs.

The most common crystallization processes are represented also in fig. 2.4. If a solution represented by point A is cooled without loss of solvent (line ABC), spontaneous crystallization will occur at point C. For a controlled crystallization process, seeds should be introduced between points B and C in the metastable zone. Supersaturation can be also achieved by removing some of the solvent from the solution by evaporation. The line AB'C' represents such an operation carried out at constant temperature.

2.1.2 Crystallization kinetics

In order to build up an understanding of the crystallization processes it is necessary to become familiar with the concepts involved. Thus, in the following are listed a number of subsections describing the crystallization kinetics as: nucleation, seeding and crystal growth. The knowledge of these is crucial to understand and properly operate the crystallization process.

2.1.2.1 Nucleation

Supersaturation on his own is not sufficient in order a system to begin to crystallize. Before crystals can develop, in the supersaturated solution there must be some solid bodies, nuclei or seeds, which then act as centers of crystallization. Nucleation may occur spontaneously or it may be induced artificially. It can often be induced by agitation, mechanical shock or friction within the solution. Some external influences such as electric or magnetic fields, UV-light, X-rays, sonic and ultrasonic irradiation have also been studied

[Khamskii1969]. Recent studies have shown that ultrasonic irradiation can reduce the induction time of the nucleation [Patel2009]. Ultrasound has also been used to replace seeding in some difficult-to-nucleate systems [Patil2008, DeCastro2007].

Different nucleation mechanisms can be distinguished based on the origin of the forming nuclei (see fig. 2.5). The homogeneous ‘primary’ nucleation can happen in solutions, where the molecules arrange themselves in a pattern characteristic of a crystalline solid, forming a bulk in which additional molecules deposit as the bulk grows into nuclei. In order such nuclei to be generated, a very high supersaturation is needed. On the other hand, suspended particles or small bubbles can also provide nucleation sites. This is called heterogeneous nucleation. Nuclei are often generated in the presence of crystals in the solution through friction or attrition. This “secondary” nucleation can occur in a slightly supersaturated solution in contrast to “primary” nucleation.

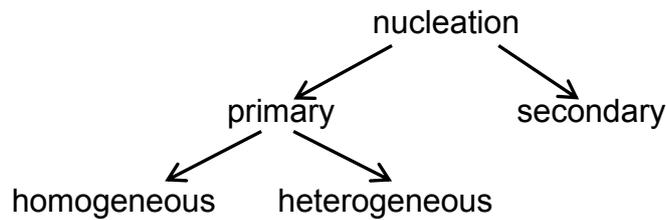


Fig. 2.5 Classification of the nucleation phenomena.

The classical theory of nucleation is based on the condensation of vapor to a liquid, and this procedure may be extended to crystallization from melts and solutions [Gibbs1948]. The free energy changes associated with the process of homogeneous nucleation may be considered as a sum of the surface free energy (i.e. the energy between the surface of the particle and bulk of the particle) and the volume excess free energy (i.e. the energy between a particle and the solute in the solution). In order a nuclei to appear a particle with a critical size is required with a minimum (or critical) free energy change of transformation per unit volume:

$$\Delta G^* = \frac{4\pi\gamma r_c^2}{3} \tag{2.10}$$

Ch. 2 | Theoretical background

It can be seen, that the behavior of the newly created spherical nucleus depends on its size and can either grow or dissolve. The critical size r_c , therefore, represents the minimum size of a stable nucleus, at which particles smaller than r_c will dissolve, and these bigger than r_c will continue to grow. The interfacial tension (or surface energy) γ between the developing crystalline surface and the supersaturated solution is included.

To explain the amount of energy, ΔG^* , necessary to form a stable nucleus, the rate of nucleation, B° , must be taken into account. It represents the number of nuclei formed per unit time per unit volume and can be approximated by a power law function of the supersaturation, also referred as the Meirs model:

$$B^\circ = k_n(c - c^*)^j \quad (2.11)$$

In the equation 2.11, k_0 is the rate constant and it is usually a function of the temperature T , whereas the exponent j is referred to as the 'order' of the overall nucleation rate. From equations 2.10 and 2.11 it can be seen that three main variables govern the nucleation rate – temperature T , degree of supersaturation Δc , and surface energy γ [Randolph1988].

2.1.2.2 Crystal growth

In a supersaturated solution a formation of stable nuclei can grow into crystals as soon as they reach a specific critical size. By the crystal growth process, the supersaturation is reduced as the dissolved molecules of the substance are deposited on the crystal surface at a rate proportional to the difference in concentration between the crystal surface and the bulk in the solution. There are many theories in the literature for crystal growth description, including the adsorption-layer theory, where crystals grow layer by layer. According to Gibbs, the surface-energy theory is based on the principle that the total surface free energy of a crystal in equilibrium with its surroundings at a constant temperature and pressure would be a minimum for a given volume. [Gibbs1948] The crystal growth is exemplarily shown including several steps on fig. 2.6

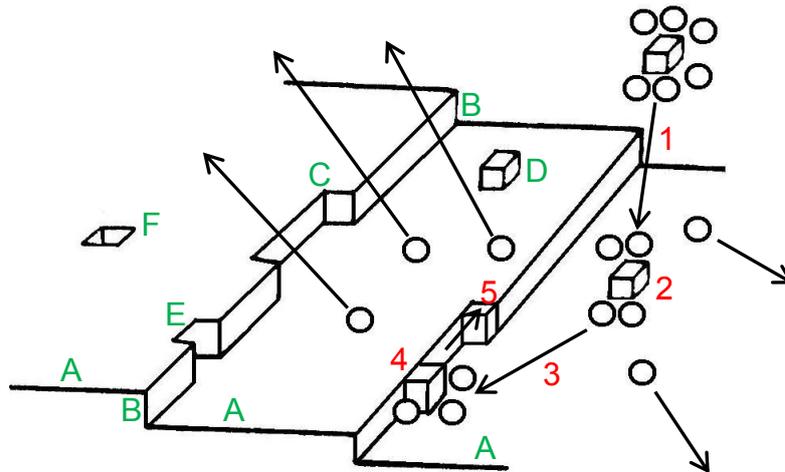


Fig. 2.6 Kossel's model of a growing crystal surface, showing flat surface (A), steps (B), kinks (C), surface-adsorbed growth units (D), edge vacancies (E), and surface vacancies (F) [adopted from Mullin2001].

According to Kossel's model, the crystal growth can be schematically represented with the following steps: (1) Transport of the molecule from the liquid phase to the liquid-solid phase boundary; (2) Adsorption of the molecule on the crystal surface with a possible desolvation; (3) Transport to an eventual layer by surface diffusion including further desolvation; (4) Assembly on the surface, thus enlarging the layer; (5) Integration on the surface and final desolvation [Kossel1934].

According to diffusion-reaction theory from the work of Noyes and Whitney, for the crystallization can be proposed [Noyes1897]:

$$\frac{dm}{dt} = k_m A(c - c^*) \quad (2.12)$$

where m is mass of solid deposited in time t ; A is surface area of the crystal; k_m is coefficient of mass transfer; c and c^* are the concentration of the supersaturated and saturated solutions respectively. On the assumption that the molecules have to diffuse from the solute to the growing crystal face, the equation 2.12 could be rewritten in the form:

$$\frac{dm}{dt} = k_d A(c - c_i) \quad (2.13)$$

Ch. 2 | Theoretical background

where k_d is coefficient of mass transfer by diffusion and c_i is solute concentration in the solution at the crystal surface. A first-order 'reaction' equation then represents the arrangement of the solute molecules into the crystal lattice:

$$\frac{dm}{dt} = k_r A (c_i - c^*) \quad (2.14)$$

where k_r is a rate constant for the surface reaction (integration) process. Equations 2.13 and 2.14 are not easy to apply in practice, because they involve interfacial concentrations, which are difficult to measure. A general equation can be then written, which eliminates the term c_i :

$$\frac{dm}{dt} = K_G A (c - c^*)^g \quad (2.15)$$

where K_G is an overall crystal growth coefficient. The exponent g is referred to as the 'order' of the overall crystal growth process. If $g = 1$ and the surface reaction (eq. 21) is also first-order, then the interfacial concentration c_i can be eliminated by combining equations 2.13 and 2.14 into:

$$K_G = \frac{k_d k_r}{k_d + k_r} \quad (2.16)$$

The overall crystal growth rate is then given as [Mullin2001]:

$$R_G = \frac{1}{A} \cdot \frac{dm}{dt} = K_G (c - c^*)^g \quad (2.17)$$

The Gibbs-Volmer theory or the adsorption layer theory is based on thermodynamic considerations. According to these considerations, the solute is not immediately integrated in the crystal lattice but forms an adsorbed layer around the crystal. Between this layer and the volume of the solution, a dynamic equilibrium is formed. During the growth process, loose lattice components from the adsorption layer are moving to the active sites in the crystal lattice (e.g. kinks, vacancies or steps). Under ideal conditions, they form a whole new level on the crystal surface [Mullin2001].

Further kinematic theories may also be mentioned, but for the purpose of this work, they are not relevant and more detailed information can be found in the literature [Mullin2001].

2.1.3 Polymorphism

By the production of fine chemical via crystallization it is not uncommon that the newly formed crystalline phase is metastable, e.g. a polymorph. Some of them can rapidly transform to a more stable phase, while others can exhibit apparent stability for a long time. Some transformations are reversible (enantiotropic), while others are irreversible (monotropic) [Mullin2001]. Polymorphism is of great importance due to its effect on some physical characteristics of the crystal lattice such as melting point, flowability, vapour pressure, bulk density, chemical reactivity, apparent solubility and dissolution rate, and optical and electrical properties. Thus, polymorphism can affect drug stability, manipulation, and bioavailability [Bernstein2002]. For example, the solubility of different polymorphs of the same compound reflects the differences in free energy between their respective crystalline states, which are different for each polymorph. Thus, the solubilities of these various crystal forms can vary in a broad range. Differences in solubility between crystalline forms of a pharmaceutical can lead to differences in bioavailability of solid dosage forms if the bioavailability is dissolution limited. In some cases, the metastable phase may have more desirable properties than the stable one, e.g. by the pharmaceutical product ritonavir, the stable polymorph form II is virtually inactive compared to the alternative metastable form I due to its poor solubility and lower bioavailability. Moreover, the “inactive” polymorph was subsequently found to convert the metastable and therapeutically effective polymorph into the stable but not so effective form on contact, due to its lower energy and greater stability [Bauer2001].

Two of the substances, used in this work, exhibit different polymorphic forms. More information about substances used can be found in chapter 3, section 3.1.

2.1.4 Cooling crystallization

The selection of a crystallization method and the proper design of a crystallizer depend on the type of supersaturation to be produced (cooling, evaporative,

drowning out, chemical reaction), the mode of operation (continuous or batch), the desired crystal size distribution and median crystal size, and the purity of the product [Mersmann2001]. Cooling crystallization is commonly practiced for solutions in which solubility is a strong function of temperature. Cooling alone can achieve the desired degree of crystallization when solubility is sufficiently low at the end of the cooling operation.

A high proportion of the industrial crystallization is carried out in batch processes. This process is mainly used when producing smaller quantities, the product is frequently changed or high product purities are required. With a batch process both the quality assurance and the quality control of the final product can be ensured [Mersmann2001].

In comparison to batch process, continuous crystallization is used when larger amounts of product have to be produced. As for the pharmaceutical industry usually only small quantities are produced, it finds less application here. In both process variants presented below the supersaturation is created by cooling.

2.1.4.1 Batch crystallization

In the operation of batch crystallizers, maintaining a constant supersaturation of the solution in the crystallizer can be challenging. If the supersaturation varies along the process, it could result in lowering the quality of the product and spreading the crystal size distribution. To ensure a constant product quality, it is essential that the process conditions are identical at the beginning of the crystallization. For the optimal adjustment of the concentration supersaturation, the following applies: $0 < \Delta c < \Delta c_{\text{metastable}}$, in order to avoid the dissolution of the seed crystals and uncontrolled nucleation. To keep the solution homogeneously mixed in a batch crystallizer, stirrers are used, which can lead to secondary nucleation due to breakage of the crystals. Higher stirrer speed has higher impact energy and thus the collision probability of the crystals is increased. An example system for batch crystallization is shown in fig 2.7.

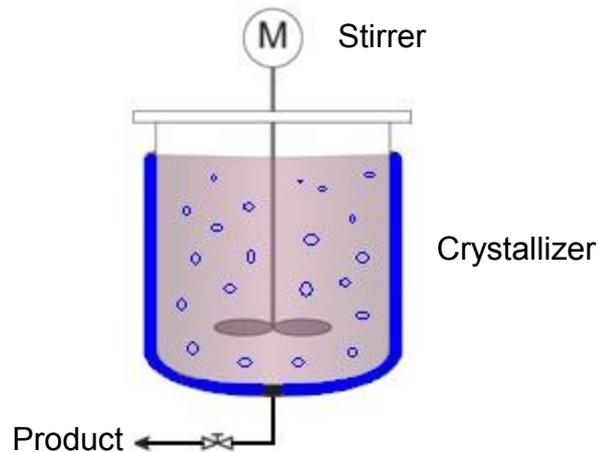


Fig. 2.7 Scheme of a batch crystallizer, filled with crystal suspension.

In the case of a one-component system, a saturated solution of the component is filled in the crystallizer and cooled until nuclei are formed through the supersaturation formed. The homogeneity of the solution is provided by a stirrer, while the temperature of the jacketed crystallizer is ensured by a thermostat. At the end of the process, the crystal suspension is fluxed through the valve into a solid-liquid separation facility (e.g. suction filter, centrifuge), where the product crystals are separated from the mother liquor. This merely simple setup and the easy adjustment of the process parameters make the batch-crystallization processes interesting for the industry. Quite the contrary, its application in the case of two- or more component systems like enantiomer separation is complicated. More information on the classical preferential crystallization process and enantiomer purification can be found in section 2.2.

2.1.4.2 Continuous crystallization

The crystallization process is run continuously when the crystallizer is integrated in a large production plant that is also operated continuously. The most important advantage of continuously operated crystallizers is the fact that the mean supersaturation is a function of the mean residence time:

$$\tau = \frac{V_{\text{sus}}}{\dot{V}} \quad (2.18)$$

where V_{sus} is the suspension volume and \dot{V} is the flow rate of the product suspension removed from the crystallizers. This means that the optimal

Ch. 2 | Theoretical background

supersaturation can be easily maintained by a certain flow \dot{V} for a given volume V_{sus} .

However, it is also important that the crystallization process occurs in the metastable region in order to avoid an unwanted nucleation. The reduction of the supersaturation takes place mainly through crystal growth. In general, a large crystal surface and thus a high number of particles are desirable.

The continuous crystallization processes can have different variants of realization. It is possible to use a batch-crystallizer in order to operate continuously. A typical example is shown in Fig. 2.8

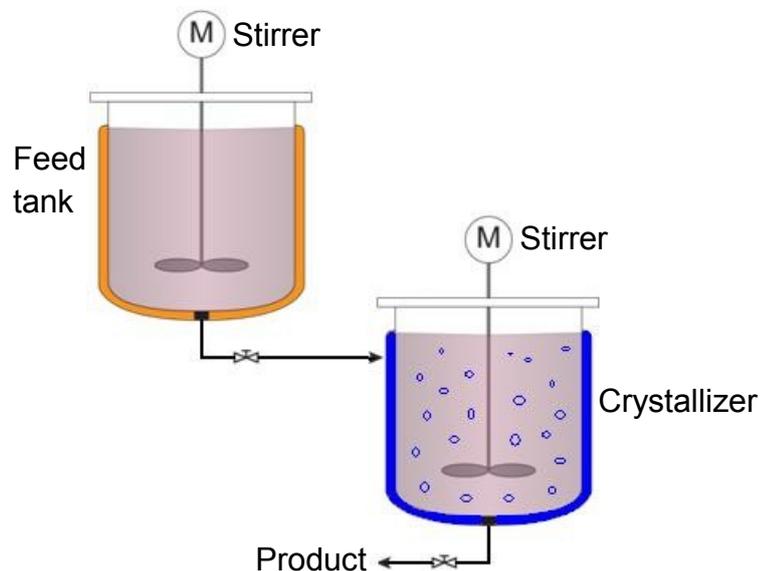


Fig. 2.8 Scheme of a continuous crystallization setup.

The feed tank is filled with a saturated solution of the substance to be crystallized. It should contain no solid particles in order to avoid nucleation and contamination, when solution is transported to the crystallizer. A filter could be used between the tank and the crystallizer if necessary. The crystallizer is operated isothermally at a lower temperature than the feed tank. Hence, the solution is cooled and becomes supersaturated. Because of the supersaturation of the solution, the substance crystals can grow, and over time part of them are collected from the bottom of the crystallizer and separated from the mother liquor in a filter. The mother liquor is then refluxed back to the feed tank and the resulted product crystals can be removed. The constant inflow of fresh solution from the feed tank and the constant takeout of a crystal suspension from the

bottom of the crystallizer assures almost constant supersaturation level and thus “quasi-steady state” can be established.

2.1.5 Seeding

The addition of solid particles of the desired substance to a crystallization medium is known as seeding. It is often only reliable way to obtain the desired phase [Beckmann2000]. Controlling the crystallization process via seeding relies on the potential of the crystal surfaces to promote secondary nucleation, while avoiding heterogeneous nucleation mediated by unknown contaminants [Mullin2001]. In this case, the supersaturation is mainly degraded by crystal growth. Furthermore, some advantages result for the operation of the crystallizers, where by addition of seed crystals incrustation can be avoided, and thus lowering the spontaneous nucleation rate. In continuous crystallizers an improved startup behavior is observed, which as a result is shorter than the corresponding batch process. A further advantage of using seeds is the reduction of the contingency of spontaneous nucleation, thus seeding can be efficiently employed for chiral resolution of enantiomers during crystallization [Jacques1994, Sheldon1990].

The factors affecting the seeding effectiveness include addition timing and method, seed surface properties, seed CSD, and the rate of supersaturation generation [Paul2005]. A reproducible production of the seed crystals is crucial for the crystallization process in order to achieve constant product quality. This also applies for the product particle size. Furthermore, the addition of the seeds into the crystallizer must be realized in a way that the relevant process parameters do not change. Moreover, the solution must be in the crystallizer in a corresponding state, wherein the seed crystals will not dissolve in the solution, but grow instead. The corresponding temperature of the process should be observed. Otherwise, by a further temperature reduction nucleation can be triggered, which results in product quality or a temperature increase, which can lead to dissolution of the seeds – also not desired.

For an optimal process control the necessary amount (or mass) of seed crystals used should be about 0.1 to 3% of the expected product yield mass

Ch. 2 | Theoretical background

[Heffels1999]. According to the same authors, the size of the seeds used should be about 10 to 30% of the desired product size.

The optimum amount of seed crystals can be calculated:

$$m_{\text{seed}} = \frac{m_{\text{final}} \cdot L_{\text{seed}}^3}{L_{\text{final}}^3 - L_{\text{seed}}^3} \quad (2.19)$$

In the equation 2.19, the m_{seed} represents the mass of the seeds needed. It is calculated using the desired product size L_{final} , a specified seed crystal size L_{seed} and the expected product mass m_{final} [Beckmann2000].

- *Exploitation of ultrasound*

The possibility to accelerate the crystallization process by applying ultrasonic (US) waves on the supersaturated solution has undergone serious development over the past years. Moreover, the US cavitation effect can initiate spontaneous crystallization without the need to introduce foreign material (e.g. seeds) and prevents agglomeration of the crystals. Moreover, the possible impurity introduction from seeding or mechanical milling can be avoided in the solution. This technique can be used, where extreme high purity is needed, like pharmaceutical and food industry [Dennehy2003, Rucroft2005].

Ultrasonic processing in simple terms is the application of sound waves in the frequency range of 20 kHz–1 MHz which is above the range of human hearing. Ultrasound is used principally to influence the initial nucleation stage of crystallization. Principally, US creates cavitation in the solution, where each cavitation event consists of first the formation of small gas or vapor bubble followed by its quick collapse. The shock wave from the local high pressure of the cavitation collapse can accelerate the motion of the molecules in the liquid and increase molecular impacts so as to initiate nucleation. Cavitation event serves as a means of generating nuclei due to high local supersaturation level to new crystal formation and growth. Ultrasound can reduce the induction time at low supersaturation levels and can narrow the metastable zone width. Therefore, the effect of ultrasound on nucleation is stronger than that of high supersaturation level [DeCastro2007, Vironea2006].

US can also be used to break up crystals into smaller fragments in order to produce seeds. The process of crystal breakage affects the average particle sizes and size distributions both through reducing the size of existing crystals and by creating secondary nucleation sites [Zeiger2011]. The crystal break up can occur either by fracture or erosion. Erosion refers to particle size reduction due to the loss of primary particles from the surface of the agglomerate, whereas fracture is the partitioning of the original agglomerate into several smaller agglomerates. Which breakage mechanism dominates may depend on the applied ultrasonic intensity and it is certainly a function of material properties [Kusters1994, Marković2008].

Several studies have been reported related to the kinetics and mechanism of US-facilitated breakage [Kusters1994, Hill1995, Raman2011]. Recently, Bari and Pandit have proposed a generic approach on solving PBE with a given CSD data to estimate the breakage kinetics [Bari2014]. The authors have obtained an empirical relation for the specific rate of breakage suggesting that rate is proportional to square root of the ultrasonic power.

Teipel and Mikonsaari have investigated the influence of the US on the size reduction of some organic and inorganic crystals [Teipel2002]. An important observation is that two of the organic crystals, hexogen (RDX) and octogen (HMX), are polymorphic substances, which did not change their form during the experiments. The authors have observed that US has almost no effect on breaking up inorganic materials (e.g. NH_4NO_3 and NaCl) and significant effect on the size reduction of the crystals with organic origin.

2.2 Enantiomers and their isolation

In this section of chapter 2 is elaborated the importance of purification of some special chemicals, called enantiomers. Furthermore, the preferential crystallization as a resolution method is introduced, where two possible techniques are given and compared.

2.2.1 Enantiomers and racemic mixtures

The amino acid molecule can be seen as a typical example of an enantiomer. It is an organic acid, which has at least one amino group ($-\text{NH}_2$) and one carboxyl

Ch. 2 | Theoretical background

group (-COOH) in its molecule. Most of them are α -amino acids. In this case, the amino group and the carboxyl group are connected to the same carbon atom. In some cases β -amino acids can also be found, where the carboxyl group is connected to the first carbon atom and the amino group to the second carbon atom [Greenstein1961].

Further, in addition to the carbon backbone, amino acids may contain additional functional groups like -COOH, =NH, -OH, or -SH. In figure 1 is shown the general formula of an α -amino acid, where R represents the rest structure or side chain.

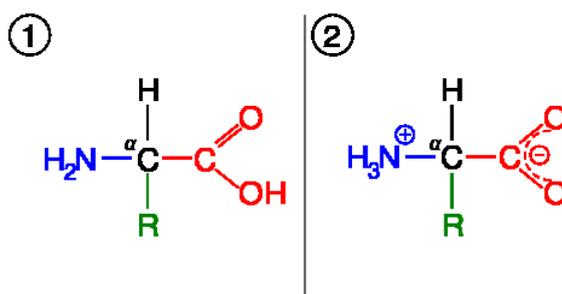


Fig. 2.9 A general formula of an amino acid in its (1) unionized and (2) zwitterionic forms. In the formula R represents the rest structure.

There are a lot of known aminoacids, but only 22 of them are so called proteinogenous [Hertweck2011]. They are the main component of the proteins, and therefore are found in every living organism. They are involved in the structure and function of cells in the body. Depending on how the structure and functional groups of the amino acids are built, they have a different effect on the proteins formed by them.

The human organism cannot synthesize itself some of the α -amino acids it needs. These are called essential amino acids and they must be supplied through food intake. Essential amino acids are valine, leucine, isoleucine, lysine, phenylalanine, methionine, tryptophan and threonine. Amino acids are generally chiral molecules (except glycine), since they have four different substituents on the carbon atom in the figure 1 (-NH₂, -H, -COOH groups and rest structure). Hence, enantiomers are stereoisomers or chemical compounds, which behave mirrored in their spatial structure. The word comes from the Greek *Enantios*, meaning the opposite. They are also called optical isomers due to the fact that they cannot be superimposed onto their mirror image or their structure cannot be brought into congruence with its mirror image by translation or rotation. Its

molecular formula and the linking of atoms are consistent with both versions, see figure 2.10. This particular type of isomerism is called chirality. The term comes from the Greek *cheir*, which means hand. Chirality is usually possible only for atoms with at least four binding arms. The left and right hand can be used as an example of a chiral system or a pair of enantiomers [Meierhenrich2008].

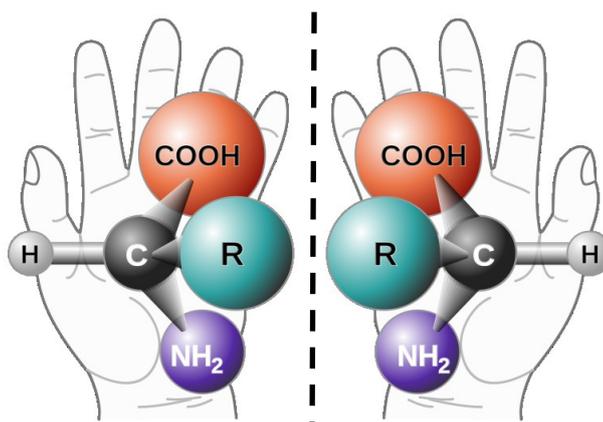


Fig. 2.10 An illustration of the chirality by analogue with the human hands. The dashed line represents the plane mirror.

In figure 2.10, the left and right hands metaphorically represent a pair of enantiomers. The dashed vertical line between the two hands represents a mirror. It can be seen from the figure, the two hands are shown superimposed, or the two molecules cannot be brought into alignment by side-inversion of either of the shown structures.

A specific feature of the enantiomers is that they have the same chemical and physical properties, like melting and boiling points, densities, solubilities and also same X-ray diffraction spectra. The only way to distinguish them is their different optical activity. They rotate the plane of linearly polarized light clockwise ((+)-enantiomer) or counterclockwise ((-)-enantiomer), where the turning angle is indicated by α . Accordingly, the (+)-enantiomer stands for the dextrorotatory form and (-)-enantiomer - the levorotatory form. When measured by a polarimeter, they rotate the plane of polarization of the linearly polarized light in each case by the same amount in the opposite direction. This property of the different direction of rotation is used for differentiation of enantiomers.

As a further possibility for enantiomer differentiation, e.g. saccharides and amino acids, the D / L system (Fischer projection) can be used. In the Fischer projection D is *dexter*, meaning right-handed, L stands for *laevus* and is left-handed.

Ch. 2 | Theoretical background

As a third possibility can be used the nomenclature system proposed by Cahn, Ingold and Prelog (CIP) [Cahn1966]. Like in the Fischer system, the enantiomers are differentiated from each other with letters (S) or (R). The abbreviations again come from the Latin, whereby R stands for *rectus* and means right and S - for *sinister*, which means left.

Another term of importance is a 50:50 mixture of enantiomers, which is generally called a racemate. In this 1:1 mixture of (+)- and (-)-enantiomer, the optical activity of the individual substances compensates. By the same right- and left-handed shares a racemate is optically inactive and has a rotation angle α of 0° .

The distinction between the two enantiomers is of great importance since they react differently in chemical reactions. Even when used as pharmacological agents enantiomeric substances can have different effects. Thus, one form has the desired effect, while the other may be indifferent, toxic or cause adverse effects. As an example, penicillamine can be used, which (S) form (D-enantiomer) is used to treat copper poisoning and the (R) form is toxic [Kuchinskas1957, Crawhall1979]. Another example is thalidomide – one stereoisomer was the beneficial agent for preventing morning sickness by pregnant women, while the other causes serious birth defects [Miller1999].

The enantiomers may also differ in taste or odor, however. In 1886, Piutti found that D-asparagine had a sweet taste, while L-asparagine was tasteless [Greenstein1961]. Leitereg et al. confirmed differences in odor for the purified limonene enantiomers. The (R)-(+)-limonene has the odor of orange and (S)-(-)-limonene has the odor of lemon [Leitereg1971].

Since the enantiomers possess different activities and effects, the presence of a counter enantiomer is unwanted, which makes their purification of great importance. One way to produce optically pure enantiomers is by using biological processes like fermentation [Leuchtenberger2005] or chemical synthesis [Coppola1987]. Still by the enantiomer production impurities can accumulate in the resulted product or some chemical synthesis lead to production of racemic solutions, where the 'impurity' of the unwanted enantiomer is 50%. For many industrially bulk-produced organic chemicals a purity of >95% is often accepted as 'pure'. For some special chemicals a purity of >99% may be demanded. For purities >99.9% the term 'ultra-pure' is frequently applied. For many chiral

products, an enantiomeric purity of around 98% can be accepted, since the 2% of the other enantiomer has little or no effect on the activity of the product [Mullin2001].

To avoid unwanted side effects from the impurities present in the resulting solutions, commonly crystallization is used for further purification purposes.

2.2.2 Preferential crystallization of simple eutectic systems

Crystallization is a very powerful technique and permits enantiomers that behave as conglomerates to be resolved from their racemic mixtures. Besides crystallization, the resolution of enantiomers can be achieved by various methods, like microbiological methods, kinetic enzymatic resolution, and chromatography [Jacques1994]. Some of the recent studies show that of growing importance are methods that permit the continuous production of pure enantiomers, such as the combination of continuous chromatographic processes and subsequent crystallization [Kaemmerer2013, Swernath2013], chiral-membrane-based separation techniques, [Xie2008, Gou2011] and polymers imprinted with chiral templates [Wattanakit2014]. Although all these techniques show high chiral discrimination, they are not yet applicable for the large-scale resolution of enantiomers. Therefore, large-scale separations are still typically achieved by classical crystallization methods. In the case of an enantioseparation process, direct crystallization can be performed in two main ways, i.e. preferential and simultaneous crystallization [Jacques1994]. The preferential crystallization process as a method for resolution of racemates has great potential and real economic importance in both pharmaceutical and chemical industries. However, profound understanding of the underlying fundamental processes such as thermodynamics and kinetics of this technique in the crystallization process is needed. To optimize the resolution technique, the behavior of chiral crystals under varied conditions must be understood [Li1997]. The resolution of enantiomers by preferential crystallization is a kinetically controlled separation process that is terminated before thermodynamic equilibrium is attained. This technique is also known as resolution by entrainment [Jacques1994]. Although most of preferential crystallization process can be applied conveniently to conglomerate system, there are few cases where it has been used for racemic

compound systems. Lorenz et al. have illustrated the possibility of preferential crystallization for such systems starting with a solution having approximately eutectic composition, which consists of the racemic compound and one of the pure enantiomers [Lorenz2006b].

In preferential nucleation the nucleation rates of both enantiomers are different. This process concept is a variant of the so called auto seeded polythermal programmed preferential crystallization process [Coquerel2007, Czaplak2008]. The most important aspect of this process is the “auto seeding”, or generation of seed crystals inside the crystallization vessel. This behavior can be attained by addition of a suitable additive that selectively inhibits nucleation of one of the enantiomers. This promotes the other enantiomer to nucleate. Ndzié et al. demonstrated a successful enantiomeric resolution of (\pm)-5-Ethyl-5-Methylhydantoin by means of preferential nucleation [Ndzié1998].

By the simultaneous crystallization, the process consists of seeding the racemic supersaturated solution with comparatively large seeds of one of the enantiomers which eventually grows larger. At the same time, the spontaneous crystallization of the counter enantiomers by the small seeds will create small crystals which can be separated from the larger enantiomeric crystal by sieving [Jacques1994]. Resolution by entrainment is based on the differences in solubility of the racemate and the pure enantiomers [Li1997].

Resolution of racemic conglomerates by preferential crystallization is the easiest and cheapest method available for the generation of pure enantiomers [Jacques1994].

2.2.2.1 Preferential crystallization in a batch crystallizer

Two different principles of preferential crystallization for the batch process exist, the isothermal and polythermal process management [Jacques1994, Coquerel2007, Elsner2009]. In this work only isothermal process control is used, so further explanations on polythermal process management as well as recent publications on the subject can be found elsewhere [Polenske2009, Czaplak2010, Levilain2010, Elsner2011].

The enantiomeric separation of racemic mixtures by means of preferential crystallization is carried out in the three-phase region of the ternary phase

diagram. This is administered by the addition of seed crystals of a pure enantiomer in a supersaturated racemic solution. Hence, a crystallization setup with only one crystallizer (like shown in fig. 2.7) is not efficient, because only one enantiomer can be separated, thus the concentration of the other will increase in the solution, resulting a spontaneous nucleation and contamination of the product. Yet, the process is manageable if the crystallization of the one enantiomer is terminated after some period of time by taking out the product crystals. Then the residual solution is heated in order to dissolve all solid particles and after temperature is lowered and supersaturation is again built, seeds of the counter enantiomer can be added. The principle for such cyclic batch process is illustrated on a ternary phase diagram, see figure 2.11.

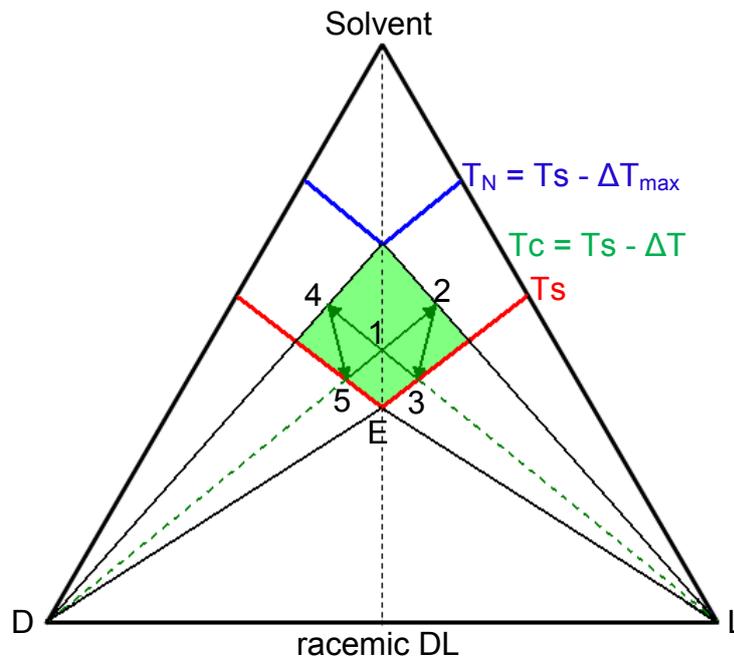


Fig. 2.11 Example of a cyclic preferential crystallization process of a conglomerate-forming chiral system in a ternary phase diagram.

A solution, consisting of the two enantiomers present in racemic composition, is saturated at a certain equilibrium temperature (T_s) in a batch-crystallizer (point E). The solution is cooled to a crystallization temperature (T_c), and thus supersaturation is achieved in the solution (point 1). The temperature difference between the T_s and T_c has to be chosen such that point 1 remains in the metastable region (area plotted in green). This is necessary to avoid spontaneous nucleation of counter-enantiomer, which can happen if the

temperature goes below T_N . The crystallization process is initiated by adding seed crystals of one enantiomer to the crystallizer (e.g. D-enantiomer). A high driving force for crystallization of the D-enantiomer will occur in the beginning, when the degree of supersaturation is still high. Over time, as the liquid phase becomes poorer with the D form, the system faces greater instability and crystallization of the L-enantiomer arises at point 2. Before reaching this state, the crystallization should be stopped and the product crystals collected. Then racemate is added in the system, which is indicated by the line 2-3 along with an increase of the temperature to T_s . At point 3 L-enantiomer seeds are added after the system is cooled to temperature T_c . Because of the high driving force the L-enantiomer will crystallize preferably until point 4 is reached, where crystallization of D-enantiomer arises. Again the crystallization should be stopped by collecting the L-enantiomer product crystals, then racemate is again added and the temperature is increased to T_s (point 5). The cyclic preferential crystallization process is closed with adding again seeds of the D-enantiomer, cooling the system to T_c and further crystallization until point 2 is reached. By this procedure, the two enantiomers can be obtained as pure products cyclically, where a maximum difference in the crystallization rates between the two enantiomers can be achieved between points 3 to 1 and 5 to 1 (Elsner2009, Polenske2009). Ideally the process could be operated infinitely. In practice there are certain limitations. Due to the recycling of the mother liquor, impurities will accumulate. This can lead to alteration of the crystallization kinetics or changes of the system solubility, which directly impacts the cyclic crystallization process and can lead to fluctuations or even its termination [Czapla2010].

2.2.2.2 Continuous preferential crystallization in coupled crystallizers

In this chapter section will be summarized the theoretical basis on the continuous preferential crystallization, which is of particular relevance for this work. The preferential crystallization process can be realized in two coupled crystallizers, connected in series or parallel. The scheme of such coupled crystallizers is shown in Fig. 2.12.

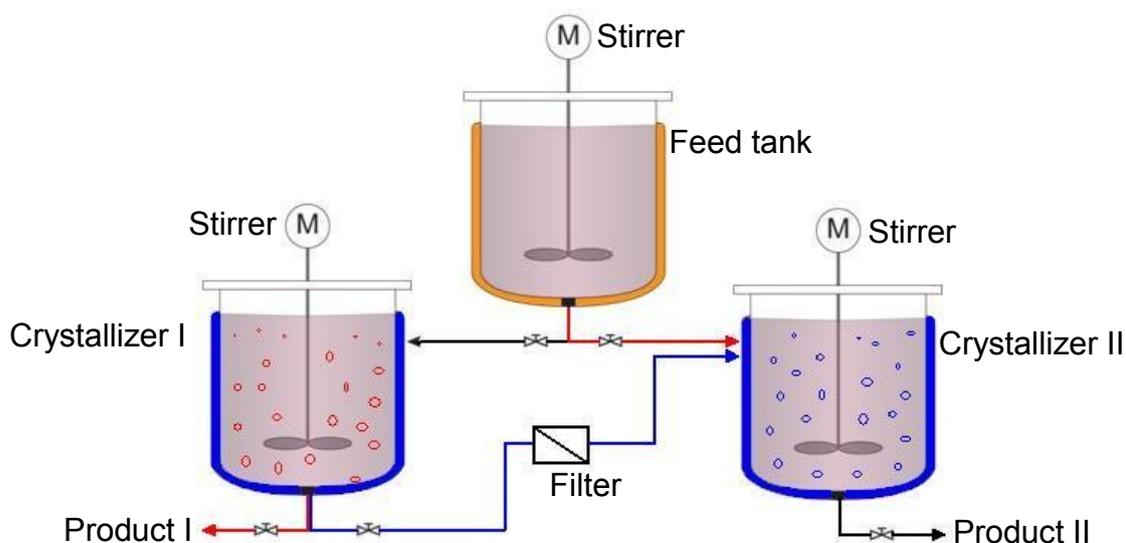


Fig. 2.12 Scheme of a continuous crystallization setup for racemate separation, realized in two crystallizers. With red / blue arrows is represented the parallel / serial operation. Black arrows are used by the both operations.

In the feed tank a saturated solution of the racemic mixture of the both enantiomers is placed. The solution is pumped through filters in order to keep it particle-free and to avoid unwanted nucleation and contamination. In both crystallizers the solution is cooled to the crystallization temperature and seed crystals of the corresponding enantiomer are added. Because of the supersaturation of the solution, they grow, and over time are collected from the bottom of the crystallizers and separated from the mother liquor in a filter. In the case of serial operation the suspension taken out from crystallizer I should be filtered, then the solution heated to dissolve eventual solid, and then the clear solution is poured into crystallizer II. The advantages of the parallel operation over the serial one is that the enantiomer ratio in the solution is close to 1:1, thus avoiding the unwanted nucleation of the counter enantiomer. Moreover, continuous parallel operation can be maintained without contaminating the second crystallizer with crystals of the counter-enantiomer from the first one. The mother liquor from crystallizer II can be eventually refluxed back to the feed tank in the case of parallel operation or pumped into crystallizer I, thus realizing a cyclic process in the case of serial operation [Tung2009].

In this work, continuous preferential crystallization in two parallel connected fluidized bed crystallizers is realized isothermally. The process is illustrated on a

Ch. 2 | Theoretical background

ternary phase diagram in figure 2.13, while a detailed description of the experimental setup can be found in section 3.3 of this thesis.

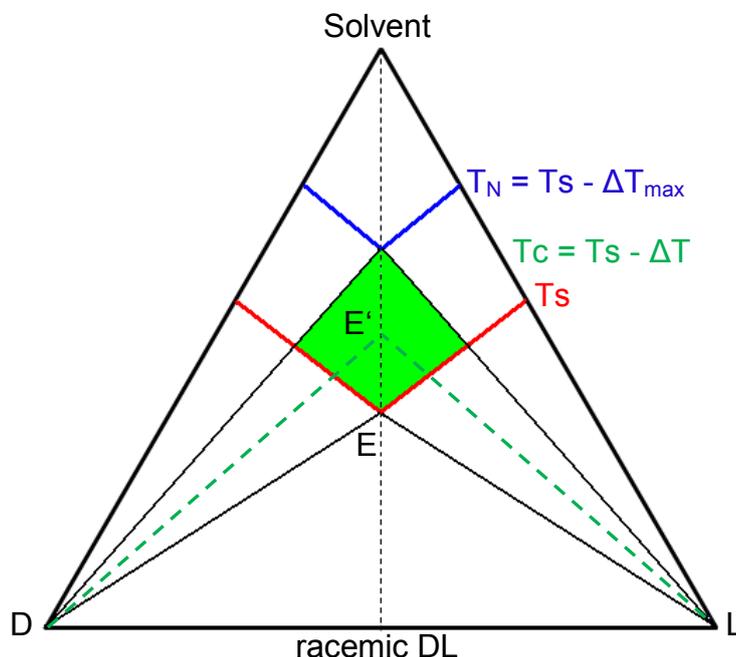


Fig. 2.13 Ternary phase diagram example of a continuous preferential crystallization process of a conglomerate system, isothermally realized in two parallel coupled fluidized bed crystallizers.

A solution, consisting of the two enantiomers present in racemic composition, is saturated at a certain equilibrium temperature (T_s) in a feed tank (point E, fig. 2.13). The solution is simultaneously pumped into two fluidized bed crystallizers, where it is cooled to a crystallization temperature (T_c), and thus supersaturation is achieved (point E'). To initiate the process, seeds of the two enantiomers are introduced in the two crystallizers respectively, while fresh racemic solution is constantly added from the feed tank. The crystallization driving force for both enantiomers is equal and thus the enantiomer ratio in the solution remains close to 1:1 in both crystallizers.

In comparison with the coupled batch crystallizers, the fluidized bed crystallization process possesses some advantages. The constant supersaturation, generated in the crystallizers during the whole process ensures its robust control, stable crystal growth and uniform product crystal sizes. Moreover, the risk of contamination through nucleation of the counter enantiomer is very low due to the constant upward flow and thus the carrying of the formed

nuclei out of the crystallizer is ensured. Due to the upward flow, the crystal mixing and heat transfer in the fluidized bed process are more uniform in comparison with the batch one [Tung2009].

Some of the major draw-backs of the fluidized bed process are the need of an increased crystallizer vessel and the use of pumping power to ensure stable crystal fluidization. Moreover, the current lack of understanding the process makes the eventual scale-up from pilot-plant very difficult. This can lead to higher initial capital costs including longer investigation times.

2.3 Crystallization in fluidized bed

In this section of the thesis, information about fluidized bed crystallization process is given as an alternative to the stirred tank crystallizers. At first, the general principle of the process is clarified and its interrelation with the fluid hydrodynamics, which is strongly dependent on the crystallizer geometry. Furthermore, the behavior of the fluidized particles in an upward flow is discussed, along with their segregation in correlation with the respective particle size distribution and particle density. In a separate subsection, the application of the fluidized bed process is elucidated with an emphasis on its conjunction with the crystallization process. Recent studies in the current state of the mathematical modelling of the fluidization process conclude this section, followed by the classical force balance considerations, proposed by Richardson and Zaki.

2.3.1 Principle and hydrodynamics

Fluidized bed crystallization is a process, where a solution is circulated through a crystallizer in which seed crystals are suspended by the up-flowing fluid. The flow rate is such that the crystal will not settle nor flow out of the crystallization vessel and the supersaturation will remain constant with time [Myerson2001].

Fluidization is the preferred mode of operation for many physical or chemical processes. This method provides several advantages over the other methods of operation such as good solids mixing providing uniform temperature throughout the reactor, high mass and heat transfer and easy solids handling. Fluidized state of a fluid-solid system is achieved when the solid particles weight is entirely

Ch. 2 | Theoretical background

balanced by the solid-fluid interaction forces. This complete support is obtained for a fluid velocity greater than the minimum fluidization velocity.

The fluidized bed crystallization process possesses a very complex hydrodynamic behavior since a wide range of particles are employed and the liquid upflow velocity has to be such that the fines do not leave the crystallizer; at the same time, the larger particles must be kept suspended for growth, to yield the desired size crystals. Under fluidized bed conditions, particles tend to segregate according to their size/density in a multi-particle system. For particles denser than the fluidizing medium, larger/heavier particles populate at the bottom of the crystallizer and the smaller/lighter particles accumulate near the top of the bed [Seibert1998].

The crystallizer geometry design is the core of the process, upon which the fluidization of the crystals, their size distribution and process productivity depend [Tung2009]. Hence, fluidized bed crystallizers are generally conical at the bottom and tubular at the top. A generic scheme of a fluidized bed crystallizer setup is shown in fig. 2.14.

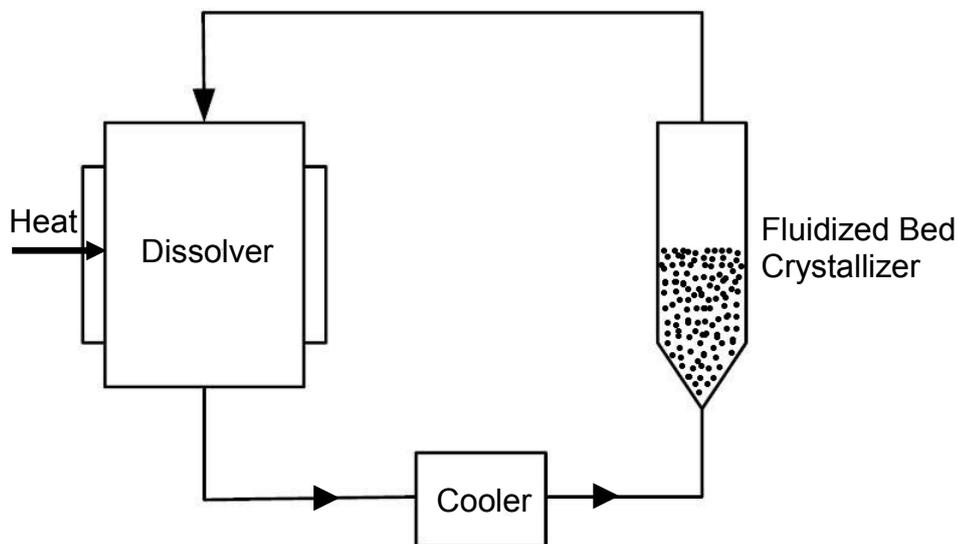


Fig. 2.14 Scheme of a fluidized bed crystallization setup [Tung2009].

In a fluidized bed crystallizer, the simultaneous progress of two processes, fluidization and crystallization, yield very complex phenomena which requires comprehensive experimentation of the process hydrodynamics, to help design an efficient crystallizer. As the supersaturated solution flows upward through a fluidized bed crystallizer, the solution contacting the bed relieves its

supersaturation on the growing crystals and subsequently the supersaturation decreases along the upward direction. As a result, crystals near the bottom grow faster than those near the top of the crystallizer. Such behavior results in the variation of particle size with height. When the bed is composed of particles of different sizes, the particle size distribution is influenced by two opposite phenomenon: classification and dispersion [Tavare1990].

Due to the complex hydrodynamic behavior of the particle mixtures, the reported studies on the fluidization of multiparticle systems are only limited to very simple situation, like fluidization of binary systems with particle differing in size or density. Al-Dibouni et al. measured the particle size distribution at various heights within the bed and came to a conclusion that classification dominates in a bed having the ratio of the largest to the smallest particle diameter greater than 2.2 [Al-Dibouni1979]. The variation of size distribution with height could be accurately predicted by assuming perfect classification of the particles in bed. With the variation of particle sizes with height, bed voidages also vary along the height of the crystallizer. Bed expansion is an important parameter required for sizing the crystallizer, which is a significant factor affecting the total cost of the process.

2.3.2 Segregation

Knowledge of bed material segregation is necessary to properly operate the crystallizer with a two-phase system. Segregation in fluidized beds occurs for several reasons including size segregation, density segregation and flow regime segregation. Classification results from the movement of particles of different weights; a large particle among the smaller one tends to reach the bottom part of the bed, whereas a smaller particle, between larger ones, rises. At the same time, dispersion is induced by irregular motions of the solid. Perfect classification and perfect mixing of the solid in fluidized bed are the two extreme situations. More often, a mixing zone is created between the two layers of classification particles, allowing partial classification within the bed. For simplicity, design methods for fluidized bed crystallizers are generally based on the perfect size classification [Nývlt1970].

Many studies have investigated size segregation of particles with equal density and different diameters [Hoffman1993]. The resulting trend from these studies is

that particles of large diameter segregate to the lower regions of the fluidized bed, while smaller diameter particles segregate to the upper regions. Other studies have investigated density segregation of particles with similar diameters and different densities [Nienow1980]. Studies have also been performed on the role of flow regime in segregation [Zhang2009]. The work of Formisani et al. suggested that segregation occurs even in completely fluidized beds with fully mixed particles [Formisani2001, Formisani2008]. Nienow et al. writes that the flow regime determines the extent of segregation in the fluidized bed [Zhang2009, Nienow1980]. Currently little is known about predicting the extent of segregation or predicting particle distributions in fluidizing beds [Howley2002].

2.3.3 Application

The first industrial application of a chemical reactor employing a fluidized bed of particles which is set in boiling motion by a rising current of gas for a coal gasification process was done by the German chemist Fritz Winkler [Winkler1926]. The application of this principle has revolutionized many industrial processes of solids treatment and in many cases made them work more successfully. Fluidized bed gasification, combustion and activation of carbonaceous material are important examples of how this type of reactor is used in coal technology. Nowadays, the industrial application of this technology extends well beyond coal. Liquid–solid fluidized beds are used in chemical industry, hydrometallurgy, food technology, biochemical processing and water treatment. A variety of operations, such as crystallization, ion exchange, adsorption as well as chemical reaction, can be conducted in liquid–solid fluidized beds. They have a number of advantages as a chemical reactor since they operate essentially at isothermal conditions. In addition, the solid particles, if used as catalysts, can be readily added to or withdrawn from the system for regeneration. The successful scale up, design and operation of liquid fluidized beds mainly depend on the accurate prediction of the behavior and features of the system, such as phase holdups and their distributions, flow patterns, and mixing levels of the individual phases. At present the understanding of liquid fluidized systems is far from complete because of the complex interactions among the phases. There is insufficient quantitative information about flow

patterns, phase holdups, solids mixing and circulation, which are all important to the estimation of heat and mass transfer rates for heterogeneous reactions [Fan1989].

Continuous crystallization methods are commonly used in the industry for the manufacture of mass-produced inorganic and organic chemicals, such as potassium chloride, ammonium sulfate, sodium sulfate, sugar, and acetylsalicylic acid [Myerson2001, Hofmann2005, Glasby1968]. The advantage of the continuous process management consists in ensuring a stationary operation and the associated stability of the crystallization conditions, consistent product quality, for example in terms of purity, particle size and particle size distribution. Usually in the field of fine chemicals, the products are manufactured in batches, where the production with respect of high system flexibility and gaining pure solid target product from the solution is carried out by batch crystallization. Critical is the necessary start-up, which can result from batch to batch of product quality variations [Randolph1988]. A particular difficulty is the "solids handling" related seeding process to initialize the crystallization. Ensuring reproducible seeding conditions, in particular the seed quality (surface area, crystal size and shape) is not trivial.

Crystal growth in a liquid fluidized bed is an industrially established process. The system involves liquid fluidization of seeded crystals, grown by moderately supersaturated solution to the solute to be precipitated. In fluidized bed crystallizers, the particles undergo considerably less attrition and breakage than in circulating suspensions crystallizers. This type of crystallizer is thus, well suited for the crystallization of large crystals. The most common type of crystallizer of this kind is Krystal (Oslo or Jerimiassen) crystallizer [Perry1997]. Mullin and his coworkers have extensively studied the operating conditions of this type of system [Mullin2001], as well as by many others [e.g. Tai1999, Epstein2003, Tung2009]. Most studies involve the crystallization of inorganic salts from aqueous solutions. Fluidized-bed crystallizers can be operated in both the batch mode and the continuous mode, with bottom discharge of the enlarged crystal product [Yang2003]. Due to the longer residence times and degree of supersaturation, the suspended crystals can reach bigger sizes in comparison with these from the batch process [Tung2009].

The removal of fluoride in a fluidized bed crystallizer by crystallization on the surface of sand grains has been studied as an alternative to chemical precipitation. Water recycling is required in order to decrease the fluoride concentration under the acceptable levels [WHO1994]. The combination of a fluidized bed crystallizer and a sand filter bed in the process has been able to achieve a reduction in the formation of fines for technical applications. Under these conditions, process efficiencies close to 80% and pellets with calcium fluoride content higher than 97%, which are able to be reused as raw material in several applications, have been obtained [Aldaco2006].

A fluidized-bed crystallizer was employed in the study to remove lead from the synthetic wastewater by crystallization of metal carbonate precipitates on surfaces of the sand grains. For the influent concentration up to 40 mg/L, lead removal efficiency reached 99% and the effluent concentration was less than 1 mg/L when the system was operated with a series of optimum conditions. In addition, the stable operation in terms of lead removal and solution turbidity was observed after a 380-minute operation. Analysis of the composition of crystals deposited on the sand grains surface showed that nearly 99% was lead salt [Chen2000].

The feasibility of phosphate removal from the supernatant of anaerobically digested sludge by struvite (MAP, MgNH_4PO_4) crystallization in a fluidized-bed crystallizer was studied by Battistoni et. al. [Battistoni1997]. Quartz sand was used as seed material. The combination of quartz sand as seed material and air stripping avoids the use of chemicals to reach appropriate pH values for struvite crystallization. All the phosphate is crystallized as MAP and no precipitate is formed when external continuous aeration is adopted.

Fluidized bed crystallization of APIs and enantiomers

The crystallization of acetylsalicylic acid (aspirin) from absolute alcohol in a fluidized bed crystallizer has been reported by Glasby et al. [Glasby1968]. Ogawa et al. have studied the growth of L-alanine crystals in a fluidized-bed crystallizer under the influence of a magnetic field [Ogawa2009]. Microscopic observations of the results of crystallization revealed that the c-axes of the L-alanine crystals

moving in the solution were parallel to the direction of the applied magnetic field. Moreover, it was found that the orientation of the fine crystals adhered to the surface of the growing crystals and the surface topography of the crystals could be controlled by applying a magnetic field in the fluidized-bed crystallizer [Ogawa2009].

In chapter 11 of his book, Tung et. al. have presented a kinetic separation of enantiomers in heavily seeded, all-growth, limited residence time fluidized bed crystallizers, using a continuous (steady-state) process for tight control of supersaturation, unchanging with time. The utilization of the fluidized bed crystallizers helps to avoid the need for heavy-magma, high-flux filtration equipment. [Tung2009]. The continuous kinetic resolution of stereoisomers was put into production, using production-scale fluidized bed crystallizers in 1967, using ultrasonic cleavage of seed particles to maintain the continuity of the crystallization process [Midler1970]. The process was investigated by Michael Midler Jr., who have extended the application of the fluidized bed crystallization by coupling two crystallizers (tubular crystallizers with conical lower part) together in serial or in parallel mode, thus a preferential crystallization of some conglomerate forming systems could be performed (DL-N-acetyl aminonitrile and DL-acetamido-(p-hydroxyphenyl)-propionitrile, both soluted in methanol). The necessary seed crystals are continuously produced in situ by means of ultrasonic comminution. The resulted product crystals had a purity of over 97%, based on polarized light rotation measurements [Midler1975, Midler1976]. This system design has shown the potential for the targeted control of particle size, while supporting an automated generation of seed crystals, which eliminates the problems of non-reproducibility of the seeding process.

This thesis was inspired by Midler's works and is based on the concept to investigate the possibility of continuous separation of enantiomers on one hand and the simultaneous product design (crystal size and shape, purity, polymorphism, etc.) on the other. The principle of this method should be applicable also to other isomer separations (assuming they have a eutectic in the system), thus increasing its potential for broader deployment.

2.3.4 Force balance model for evaluation of particle position

A large amount of work has been done on developing models for gas-solid fluidized beds (e.g. population balance modelling for continuous fluidized bed spray granulation) [Heinrich2002]. Only a few researchers have attempted to develop models for fluidized bed crystallizers. This may be due to the complex nature of the fluidized bed crystallizer and the limited application of this type of crystallizer for the realization of the crystallization processes. Frances et al. developed a model for a continuous fluidized bed crystallizer, based on the description of the fluidized bed as a multistage crystallizer [Frances1994]. The model was developed in order to take into account the segregation and particles mixing within the bed, while providing better prediction of the mean size of the product. Influences of various parameters on ammonium sulphate crystallization in a fluidized bed crystallizer were simulated by Belcu and Turtoi [Belcu1996]. The model was developed based on a phenomenological approach and the results found strong influence of the equipment geometry. Shiau et al. developed a theoretical model for a continuous fluidized bed crystallizer, assuming that the liquid phase moves upward through the bed in plug flow and the solid phase in the fluidized bed is perfectly classified [Shiau1999]. The model describes the variations of crystal size and solute concentration with vertical position within the crystallizer and also allows one to study the effects of various operating parameters, such as the feed rate and height / diameter ratio, on the performance of a continuous fluidized bed crystallizer. Later, the same investigators performed a study on the interactive effects of particle mixing and segregation on the performance characteristics of a batch fluidized bed crystallizer [Shiau2001]. In this model, the liquid phase is again assumed to move upward through the bed in plug flow and the solid phase is represented by a series of equal-sized ideal mixed beds of crystals.

It is attractive to know the steady state position of a particle size distribution in a fluidized bed crystallizer. The Richardson-Zaki correlation was found to be effective in predicting the bed expansion characteristics of a fluidized bed of mono-sized spherical particles [Gibilardo2001, Richardson1954]. It comprises a formulation of the conservation equations for mass and momentum in a fluidized

suspension, and applications of these equations to the prediction of system behavior in steady state. A starting point for the examination of the mechanism of the fluidization process, which involves the suspension of a large number of solid particles in an upward flowing fluid, is the simple case of the single particle with fixed diameter. The fluidization process of the particle is essentially based on force balance considerations. Herby the forces acting on a single particle are depicted in Fig. 2.15

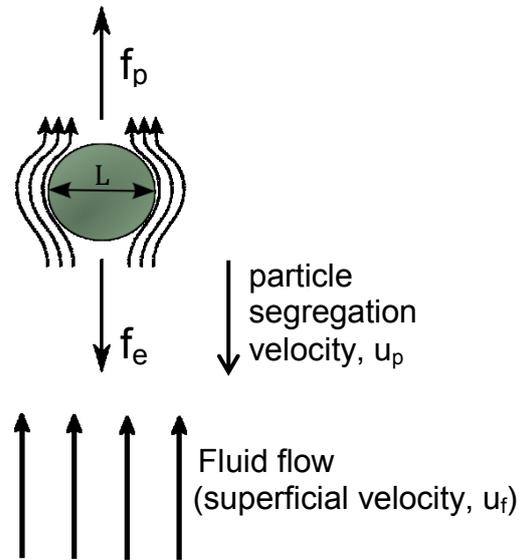


Fig. 2.15 Single particle in a suspension with important forces acting on it.

As seen from figure 2.15, important forces acting on a fluidized particle with a diameter L are the fluid-particle interaction force f_p and the particle effective force f_e . Under equilibrium conditions, they are equal and the particle position can be quantified:

$$f_p + f_e = 0 \tag{2.20}$$

The fluid-particle interaction force f_p can be represented as the buoyancy force, f_b , and the total drag force, f_d , in the following form:

$$f_p = f_b + f_d = \frac{\pi L^3}{6} g \rho_f + 3\pi u_f L \mu_f \tag{2.21}$$

Ch. 2 | Theoretical background

where L is the particle diameter, g is the standard Earth gravity, u_f represents fluid superficial velocity; ρ_f and μ_f are fluid density and fluid viscosity, respectively.

The description of the particle effective force, f_e , includes the gravity force acting on the particle and the buoyancy force, f_b :

$$f_e = f_g + f_b = -\frac{\pi L^3}{6} (\rho_p - \rho_f)g \quad (2.22)$$

From both equations it can be seen that in equilibrium conditions the drag force equals the gravity force but with opposite sign, i.e. $f_d = -f_g$.

If a low fluid flow rate is considered around a sphere, where the fluid streamlines follow its contours (the so called creeping flow regime, or laminar flow), then the empirical relation for the drag force can be expressed dimensionless by introducing the drag coefficient, C_D , which is [Gibilaro2001]:

$$C_D = \frac{f_d}{(\rho_f u_f^2 / 2)(\pi L^2 / 4)} = \frac{24 \mu_f}{u_f \rho_f L} = \frac{24}{Re_p} \quad (2.23)$$

where Re_p is the Reynolds number. It is defined as the ratio of inertial forces to viscous forces and consequently quantifies the relative importance of these two types of forces for given flow conditions [Gibilaro2001].

At equilibrium, the drag force can be rewritten in order to include the particle segregation velocity, u_p :

$$C_D = \frac{4 g L (\rho_p - \rho_f)}{3 u_p^2 \rho_f} \quad (2.24)$$

From equations 2.23 and 2.24 can be seen that C_D is a function of Re_p and hence of u_p . So equation 2.24 can be solved for u_p , which for the laminar flow regime has the following form:

$$(2.25)$$

$$u_p = \frac{(\rho_p - \rho_f)gL^2}{18\mu_f}$$

The above expression for the segregation (or terminal) velocity of a single particle can be expressed in dimensionless form, thereby introducing the Archimedes number, Ar , which can be used in further characterization of the fluidized state:

$$Ar = \frac{\rho_f(\rho_p - \rho_f)gL^3}{\mu_f^2} \quad (2.26)$$

Consider a defined volume with height H and a cross-sectional area A , representing a fluidized bed of uniform particles. In order to consider the forces acting, one must take into account the total energy content of the fluid entering and leaving, as well as the dissipation of this energy brought by the individual particles. Thus, the hydrodynamics of such fluid includes the so called unrecoverable pressure loss due to particle-fluid frictional iterations, which rises with the bed height. Moreover, the fluid superficial velocity, u_f , depends on the fraction of the bed cross-section, A , free from particles, which is the void fraction, ε , available for flow. Combining all these factors and including tortuosity and the friction factor, for the unrecoverable pressure loss can be written [Gibilaro2001]:

$$\Delta P = \left(\frac{18}{Re_p} + 0.33 \right) \frac{H\rho_f u_f^2}{L} (1 - \varepsilon)\varepsilon^{-4.8} \quad (2.27)$$

where, the power value of -4.8 will be explained later. This convenient relation between the particle drag and the unrecoverable pressure loss is a revised version of the known Ergun equation [Ergun1949]. It is applicable over the full expansion range, $1 > \varepsilon \geq 0.4$. In contrast, the standard Ergun equation is applicable only for normal packed beds with $\varepsilon \approx 0.4$ and deviates with increase of the void fraction.

Richardson and Zaki have done an extensive experimental investigation of the fluidized bed behavior [Richardson1954]. Their large amount of observations can be described by the following empirical equation:

$$u_f = u_p \varepsilon^{n_{RZ}} \quad (2.28)$$

Ch. 2 | Theoretical background

The parameter n_{RZ} was found to correlate with the particle Reynolds number. A more convenient relation enables n_{RZ} to be evaluated from the Archimedes number:

$$\frac{4.8 - n_{RZ}}{n_{RZ} - 2.4} = 0.043Ar^{0.57} \quad (2.29)$$

$$n_{RZ} = \frac{4.8 + 0.1032Ar^{0.57}}{1 + 0.043Ar^{0.57}} \quad (2.30)$$

Under viscous conditions ($Ar \ll 1$), the value for n_{RZ} is 4.8 and under inertial flow conditions ($Ar \gg 1$) $n_{RZ} = 2.4$, thus the border conditions for n_{RZ} are set.

Concluding this section, the primary forces acting on a fluidized particle can be identified as the gravity, buoyancy and the drag forces. Thus, for single particle suspension an effective weight, W_e , of a particle can be defined as the net effect of gravity and buoyancy in correlation with particle diameter:

$$W_e = f_g + f_b = -\frac{\pi L^3}{6} (\rho_p - \rho_f) g \varepsilon \quad (2.31)$$

This relation shows the effective weight of an average fluidized particle under equilibrium conditions is proportional to the void fraction.

For the complete drag force adopted for all flow regimes can be written:

$$F_d = \frac{\pi L^3}{6} (\rho_p - \rho_f) g \left(\frac{u_f}{u_p} \right)^{\frac{4.8}{n_{RZ}}} \varepsilon^{-3.8} \quad (2.32)$$

The consistency of the equations for W_e and F_d can be confirmed at equilibrium conditions (where both are equal), thus, yielding the Richardson-Zaki relation:

$$W_e + F_d = 0 \quad (2.33)$$

$$-\frac{\pi L^3}{6} (\rho_p - \rho_f) g \varepsilon + \frac{\pi L^3}{6} (\rho_p - \rho_f) g \left(\frac{u_f}{u_p} \right)^{\frac{4.8}{n_{RZ}}} \varepsilon^{-3.8} = 0 \quad (2.34)$$

After truncating the equal terms, equation 2.34 can be reduced to:

$$\varepsilon^{4.8} = \left(\frac{u_f}{u_p} \right)^{\frac{4.8}{n_{RZ}}} \quad (2.35)$$

From equation 2.35 it is easily seen, that solving for u_f after unifying the power values gives the Richardson-Zaki equation 2.28.

The application of equation 2.28 is only valid at steady state operation of the fluidization process, thus allowing the estimation of a position of particles with certain diameters, depending on the experimental process parameters and crystallizer geometry.

In order to take into account the difference between the assumed spherical particles and real crystal shapes, a sphericity parameter, Ψ , can be introduced. It was defined by Wadell as the ratio of the surface area of a sphere, which has the same volume as the particle, to the surface area of the particle [Wadell1935]:

$$\Psi = \frac{\sqrt[3]{\pi(6V_p)^2}}{A_p} \quad (2.36)$$

where V_p and A_p are the particle volume and particle area respectively. Hereby, the calculated particle diameter, L , has to be multiplied by the sphericity parameter, Ψ , to achieve the predicted mean particle size, d_{50} , to be compared with corresponding experimental values of component specific measured CSD i.e. $d_{50} = L \cdot \Psi$.

From equation 2.36 can be seen, that Ψ is dimensionless and can have values between 0 and 1, meaning that particle forms similar to a sphere will have sphericity parameter closer to 1 and particles with long, needlelike forms will have a sphericity parameter closer to 0.

This simplified balance force model will be applied in chapter 4.4.1.4 to predict the steady state position of crystals in the fluidized bed crystallizer and to compare calculated data with experimental measurements. Since the model comprises only the segregation of a single particle in the fluidized bed, an extension to the model is introduced in chapter 4.1, where the crystallization dynamics and size distributions are is considered in addition.

Ch. 2 | Theoretical background

Main goal of this thesis is to extend essentially the knowledge for the crystallization process in fluidized bed by conducting systematic experimental work in a specially designed experimental setup for selected challenging separation problems, which will be described in the next chapter.

3. Experimental

The chapter is divided into three sections. In the first section 3.1, an overview of the physical and chemical properties of the investigated glutamic acid, asparagine and aminobenzoic acid model systems is given. The second section provides detailed information about the methods, procedures and experimental setups used. In the last section, the basics and application of the analytical techniques and instruments used are explained.

3.1 Selected model compounds

The materials, used in this work, can be separated into two groups. In the first one are the two aminoacids - asparagine and glutamic acid. They are chiral conglomerate-forming compounds and therefore are optically active substances. The other group is represented by the isomers of the aminobenzoic acid. It is a stereomeric system exhibiting simple eutectic, showing constitutional isomerism. Furthermore, the safety precautions for the substance handling have to be taken into account and are thus described in this section.

3.1.1 Glutamic acid

Glutamic acid system consists of two enantiomers, namely D-glutamic acid and L-glutamic acid as a racemic mixture. From them only the L-enantiomer finds application and can be naturally found. L-Glutamic acid is a nonessential alpha-amino-acid, daily needed in the human metabolism. It is important for the protein-buildup and it is part of the polypeptide chain. In small amounts, L-glutamic acid can be produced by the body itself, but the majority is obtained as a nutrient from the food. In the living cells of certain tissues, glutamic acid acts as energy source and is responsible for detoxification processes [Plaitakis2001]. Furthermore, it acts as an important neurotransmitter between nerve cells for the stimulus extension [Yamada2005, Robinson1987]. Naturally, L-glutamic acid is available from protein-rich foods, such as grain, curd, soybeans, tomatoes, chicken meat and milk. While bound glutamic acid has no effect on the taste, free glutamic acid acts as a flavor enhancer. Therefore it is used in the food industry as a food

additive, abbreviated as Glu or E620 [EU2011]. The flavor enhancer is mainly used for production of ready meals such as canned soups and broths, but can be found in small amounts in all processed foods. Total consumption of glutamate from food in EU ranged from 5 to 12 g/day. A maximum intake of 16 g/kg body weight is regarded as safe. Thus, the general use of glutamate salts as a food additive can be regarded harmless for the human [Beyreuther2007].

L-Glutamic acid is produced mainly by fermentation, where over 15 registered patents on the subject were applied from Ajinomoto Co., Inc. in the last 3 years (2011-2013). The 2-aminopentanedioic acid is an alpha-amino-acid and has two mirror image forms – L- (S-) and D- (R-). In fig. 3.1 the two structural formulas of glutamic acid enantiomers are shown.

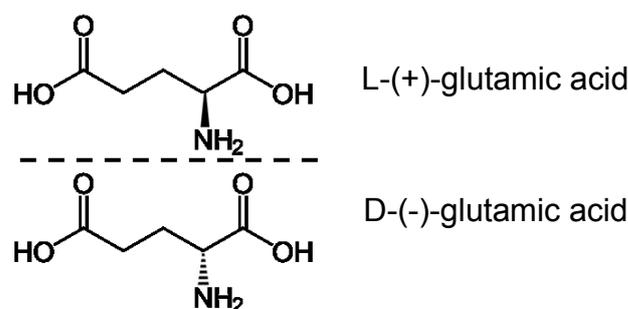


Fig. 3.1 Structural formula of the glutamic acid enantiomers. Dashed line represents mirror plane.

The glutamic acid substance is a white powder with a molecular formula $C_5H_9NO_4$, which is the same for both enantiomers. The physical and chemical material properties of the two enantiomers are identical and some of them are summarized in Table 3.1.

Table 3.1 Physical and chemical properties of the glutamic acid enantiomers at 25 °C, 100 kPa [Chemspider591].

Molecular formula	$C_5H_9NO_4$
Molar mass	147.13 g/mol
Appearance	white crystalline powder
Density	1.54 g/cm^3 (20 °C)
Melting point	205 °C decomposition
Solubility in water	see chapter 4, section 4.1
Rotation angle α (at 20°)	34.5° (10 mol in 2N HCl)
Toxicity (LD ₅₀ oral by rats)	> 30000 mg/kg

Although the physical and chemical properties of the both enantiomers are the same, they are different in taste. The taste of the L-form of glutamic acid is sweet to sour, while the D-form is neutral in taste [Kawai2012].

L-Glutamic acid crystals have two polymorphic forms. Its α -form has a crystal morphology comprising a prism with bipyramid terminations, while the more stable β -form is needle-like [Mougin2002]. For the D-glutamic acid only one literature source could be found, where the crystal habit of the crystals comprises a prism, when recrystallized from ethanol [Kofler1957].

For the investigations in this work, D-Glu, L-Glu and DL-Glu from Alfa-Aesar were used with a purity of 99%. The enantiomer excess (ee) content was proved with a HPLC and showed 100 ee% for the both enantiomers and 0 ee% for the racemate.

3.1.2 Asparagine monohydrate

The alpha-amino-acid asparagine is isolated from the juice of asparagus for the first time from which it is named [Vauquelin1806]. In nature, mostly L-asparagine occurs especially in protein-containing plants such as soy, potatoes and cereal grains, as well as in animal sources beef, eggs and seafood. The human organism is, however, also being able to synthesize L-asparagine. Therefore, it is one of the nonessential amino acids. Under the influence of the enzymes transaminase and asparagine synthetase, it is synthesized in the liver from oxaloacetate [Cooney1970]. Asparagine is used in the human body as a nitrogen transport and to carry away the toxins. The L-enantiomer is used medically in cases of low blood pressure, kidney problems, or liver damage. The peptide fullicin includes a D-asparagine residue shows higher bioactivity compared to fullicin containing the L-enantiomer [Meierhenrich2008]. Asparagine or 2-amino-3-carbamoylpropanoic acid is a proteinogenic amino acid and is abbreviated with Asn or N. It is an optically active molecule, having two mirror enantiomers, shown in fig 3.2. The amino acid is present as L-Asn or D-Asn. Other names for the L-enantiomer are (S)-Asn or (+)-Asn, while for the D-enantiomer corresponding are (R)-Asn or (-)-Asn [Meierhenrich2008].

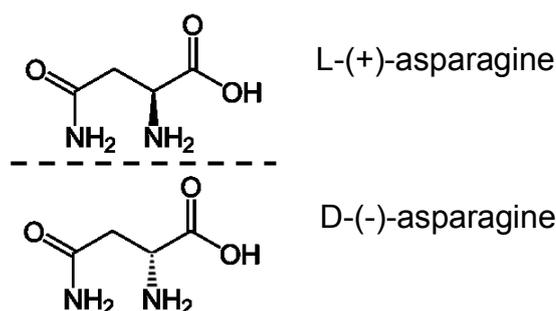


Fig. 3.2 Structural formula of the asparagine enantiomers. Dashed line represents mirror plane.

The asparagine substance is a stable white crystalline powder with a molecular formula $C_4H_8N_2O_3$, but it is moisture-sensitive. By the production of the asparagine enantiomers through crystallization, a monohydrate is formed. There are no known polymorphs found in the literature. Furthermore, the physical and chemical material properties of the two enantiomers are identical and some of them are summarized in table 3.2.

Table 3.2 Physical and chemical properties of the asparagine enantiomers at 25 °C, 100 kPa [Chemspider231].

Molecular formula	$C_4H_8N_2O_3$
Molar mass	132.12 g/mol
Appearance	white crystalline powder
Density	1.54 g/cm ³ (20 °C)
Melting point	235 °C decomposition
Solubility in water	see chapter 4, section 4.1
Rotation angle α (at 20°)	34.5 ° (10 mol in 2N HCl)
Toxicity (LD ₅₀)	no data available

As by the glutamic acid enantiomers, the asparagine enantiomers differ by the optical rotation measurements of the polarized light, resulting in an equal value, but with opposite sign. The asparagine enantiomers differ also in taste, as L-asparagine tastes bitter and D-asparagine is sweet [Meierhenrich2008].

For the investigations in the thesis, D-asparagine monohydrate, L-asparagine monohydrate and DL-asparagine monohydrate from Alfa-Aesar were used with a purity of >98 %. The enantiomer excess (ee) content was proved with a HPLC and showed 100 ee% for the both enantiomers and 0 ee% for the racemate.

3.1.3 Aminobenzoic acid

Aminobenzoic acid is an aromatic amino-acid with the formula $C_6H_4(NH_2)(CO_2H)$. The molecule consists of a substituted benzene ring, with two functional groups, a carboxylic acid and an amine. Hence, it has three positional isomers shown in fig. 3.3, where the prefixes *ortho*, *meta* and *para* are commonly used to indicate a 1,2- or 1,3- or 1,4- positions respectively. For the investigations in the thesis, only *ortho*- and *para*-aminobenzoic acid have been used.

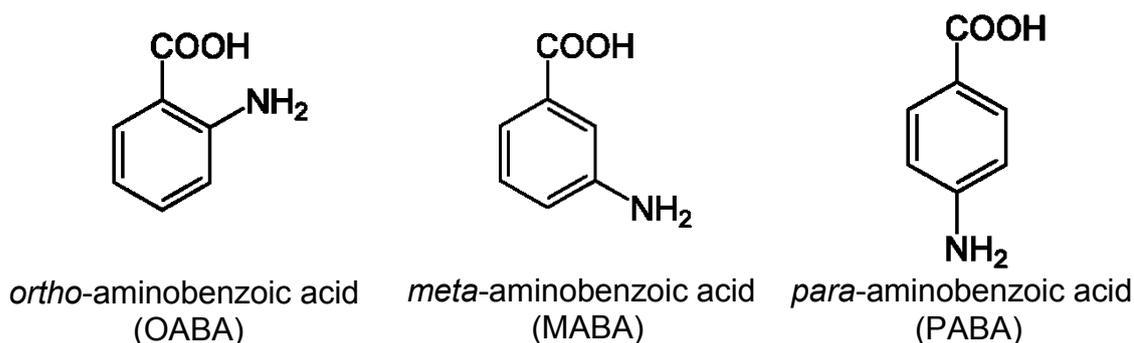


Fig. 3.3 Structural formula of the aminobenzoic stereomers.

Ortho-aminobenzoic acid, or anthranilic acid, was first obtained as a decomposition product from indigo [Fritsche1839]. It is usually produced from phthalic anhydride via sodium phthalamate, followed by oxidative decarboxylation (the Hofmann reaction) by the addition of sodium hypochlorite solution and final acidification [Maki2000]. In appearance, anthranilic acid is a yellow solid, although some samples may appear white. It is sometimes referred to as vitamin L_1 and has a sweet taste. The major use of *ortho*-aminobenzoic acid is as an intermediate for dyes and for saccharin production. As its occurrence suggests, it is an intermediate for indigo synthesis. In the dairy industry it enhances the milk production of cows.

Para-aminobenzoic acid is widely found in baker's yeast and brewer's yeast and it is a factor (Vitamin B_{10}) in vitamin B complex. It enhances the growth of various microorganisms, and it is essential to the anaerobic metabolism of some bacteria. It is also known as bacterial vitamin H_1 and is antagonistic to sulfonamide drugs. It darkens slightly on exposure to air or light. *Para*-aminobenzoic acid is used principally in the pharmaceutical industry. Other applications are as a cross-linking agent for polyurethane resins, dyes, and feedstock additives. The

conventional method of producing *para*-aminobenzoic acid is the reduction of 4-nitrobenzoic acid. A two-stage Hofmann degradation reaction of terephthalic acid is an alternative production source [Maki2000].

The main chemical and physical properties of the aminobenzoic acid stereomers are given in table 3.3. The stereomers of the aminobenzoic acid have been known to form several polymorphs. For the *ortho*-aminobenzoic acid there are three known polymorphs found in the literature: form I [Brown1985] (orthorhombic with space group $P2_1cn$), form II [Boone1977] (orthorhombic with space group $Pbca$), and form III [Takazawa1986] (monoclinic with space group $P2_1/c$), while for *para*-aminobenzoic acid two polymorphs are known, identified as needle-shaped α and prism-shaped β form [Tripathi1996].

Table 3.3 Physical and chemical properties of the aminobenzoic acid stereomers $C_7H_7NO_2$ at 25 °C, 100 kPa [Chemspider222, Chemspider953].

	<i>ortho</i> -aminobenzoic acid	<i>para</i> -aminobenzoic acid
Molar mass	137.14 g/mol	
Appearance	yellow powder	white-gray solid
Density	1.367 g/cm ³ (20 °C)	1.374 g/cm ³ (20 °C)
Melting point	144-147 °C	185-188 °C
Solubility in water	see chapter 4.2	
Toxicity (LD ₅₀ oral by rats)	5410 mg/kg	2850 mg/kg

For the investigations in the thesis, *ortho*-aminobenzoic acid and *para*-aminobenzoic acid from Merck were used with a purity of >99 %.

3.2 Methods, procedures and experimental setups

In this section, detailed description of the planning and execution of the experiments carried out is given. In the first part, the preliminary experiments are described, which include solubility, metastable limit measurement, and seed preparation of the used substances. For generation of seeds, ultrasonic cleavage of the crystals of the used substances in batch and continuous mode is explained. Furthermore, systematic crystallization experiments in a single fluidized bed are described, including studies of the application of different flow rates, influence of the ultrasonic waves on the product CSD, and different seed sizes. The steady state principle of the fluidized bed was proofed along with the

continuous ultrasonic seed generation. A special emphasis is given on the construction and operation of the experimental setups, which represent the core of this work. Finally, continuous preferential crystallization experiments of asparagine monohydrate enantiomers and aminobenzoic acid isomers in coupled fluidized bed crystallizers are described.

3.2.1 Preliminary experiments

3.2.1.1 Solubility equilibria and metastable zone width

In this subsection, methods and procedures regarding solubility equilibria, as well as metastable limit measurements of the following pure substances will be described:

- DL-glutamic acid monohydrate (DL-glu.H₂O), D-glutamic acid (D-glu) and L-glutamic acid (L-glu);
- DL-asparagine monohydrate (DL-asn.H₂O), D-asparagine monohydrate (D-asn.H₂O) and L-asparagine monohydrate (L-asn.H₂O);
- *ortho*-aminobenzoic acid (OABA) and *para*-aminobenzoic acid (PABA).

As a solvent, deionized water was used. Different concentrations of some of the above listed pure substances in water are used for measuring the solubilities and determination of the metastable zone width. The latter were carried out in the Crystal16TM reactor in the temperature range between 60°C and 5°C. Studies on the primary nucleation were also made in the Crystal16TM reactor. In both cases, the polythermal method was applied, which is described in subsection 3.2 of this chapter. A constant cooling rate of 3 K/h and constant stirring of 450 min⁻¹ for polythermal and 250 min⁻¹ for the isothermal experiments were applied. Generally, the nucleation time is a function of the cooling rate and the current solution temperature. Thus, in order to optimize and save time, used by the solubility measurements, several temperature programs were adapted. In all programs the suspension is heated in order to dissolve the solid particles and then a constant cooling rate is applied. More details about the programs are listed in the Appendix A1.

For the construction of the ternary phase diagrams, the solubilities of some mixtures of the pure substances as well as samples of the pure components were

also studied using the isothermal gravimetric method, combined with HPLC measurements.

The samples with defined mass and composition were inserted in vials and subsequently 10 g of distilled water was added. The vials were heated above the expected saturation temperature to completely dissolve the solids, and then tempered at predefined temperatures under stirring for 24 hours to guarantee an equilibrated saturated solution with an excess of crystals. The predefined temperatures for asparagine mixtures are 20°C and 40°C; for aminobenzoic acid mixtures are 20°C, 35°C and 50°C. The temperatures for the samples of the pure substances OABA and PABA: 20°C, 35°C, 40°C, 45°C, 50°C, and 60°C; and for the pure substances L-asn.H₂O, D-asn.H₂O and DL-asn.H₂O: 10°C, 20°C, 30°C, 40°C, 50°C, 60°C, and 70°C. After establishment of equilibria, samples from the fluid phase were taken through a 0.45 µm filter by using a syringe, and were analyzed for composition by HPLC. Afterwards, the phases were separated by filtration by using a vacuum filter with porosity 4 (16 µm mesh) and after drying at a room temperature the solid phases were analyzed by HPLC and XRPD.

The results from polythermal and isothermal methods were compared with each other, further combined and discussed in chapter 4.2.

It is important to determine the width of the metastable zone in the crystallization setup in order to get maximum efficiency of the crystallization process with respect to nucleation. Two series of experiments were conducted and the results are discussed in chapter 4.5.1 and 4.5.2 for the first and second series of experiments respectively.

A 50:50 mechanical mixture of OABA and PABA (first series) and DL-asparagine monohydrate (second series) were dissolved in water and the respective solutions were saturated at 35°C. After starting the circulation of the solutions in the crystallization setup, the temperature of both crystallizers was set to specific values, lower than 35°C, while the ultrasonic bath was operated at the saturation temperature. Thus, the influence of the cavitation effect on the formation of nuclei is greatly suppressed. The detection of the nucleation was done with a densitometer by measuring the density of the solutions, while considering the time since the start of the experiment. The nucleation is detected by the negative

peak of the density measurements, resulting in concentration change. The time of the event is recorded as nucleation time, t_{nucl} .

3.2.1.2 Seed preparation by sieving

For the experiments, seeds of the pure substances L-Glu, D-Glu, L-Asn.H₂O, D-Asn.H₂O, OABA and PABA were prepared by sieving, using sieve 68-90 μm on a Retsch AS200 digit sieve apparatus. The material to be sieved is taken from its original package and used as it is. It was filled into the upper sieve (90 μm). The sieve apparatus was turned on and the sieving was continued until enough material was collected in the middle sieve (68 μm). Then, the sieve fraction of 68-90 μm was collected and used further in experiments. Generally, the seeds were given once at the beginning of the experiment to initiate the crystallization process. The unused material was collected in its original package. The seed sizes were additionally characterized using laser diffraction (CILAS 1180L, Quantachrome GmbH & Co. KG) and photographs were taken using microscope Axioscope 2 (Carl Zeiss AG).

3.2.1.3 Ultrasound-forced breakage of crystals

From the literature it was elucidated, by the continuous operated crystallization processes, an important parameter is the permanent seed addition. In this work, continuous seed generation through break-up of the product crystals was applied, realized in an ultrasonic water bath outside the crystallizer. To study the crystal breakage process by using ultrasound, special experimental setups are constructed, see Fig. 3.4. Three series of experiments were conducted in each setup by using L-Glu, L-Asn.H₂O and OABA crystals respectively. In the batch experimental setup, the comminution of crystals was followed up by continuous inline measuring of their chord length distribution. The construction of the second setup (Fig. 3.4b) was necessary in order to reproduce the results in the same experimental setup section, as used in the crystallization facility.

The batch experimental setup (Fig. 3.4a) consists of a tempered ultrasonic (US) water bath and an immersed glass reactor in such way, that the level of the suspension in the reactor is below the water level in the US bath. A FBRM probe was inserted in the reactor along with a temperature sensor Pt-100. A mechanical

stirrer was used for homogenization of the suspension. An at 25°C saturated aqueous solution of the respected substance was prepared and filtered in order to remove all solid particles. The solution was poured in the reactor and temperature of the US bath was set at 25°C. A predefined amount (5 g) of already produced crystals of the substances studied was suspended in the reactor. Before starting the ultrasonic device, the FBRM probe was started to measure the crystal chord length distribution in the suspension. After 5 min, the US comminution was started using predefined percentage (100%, 50% and 10%, or 480, 240 and 48 W respectively) of the unit US output power for a total of 30 min.

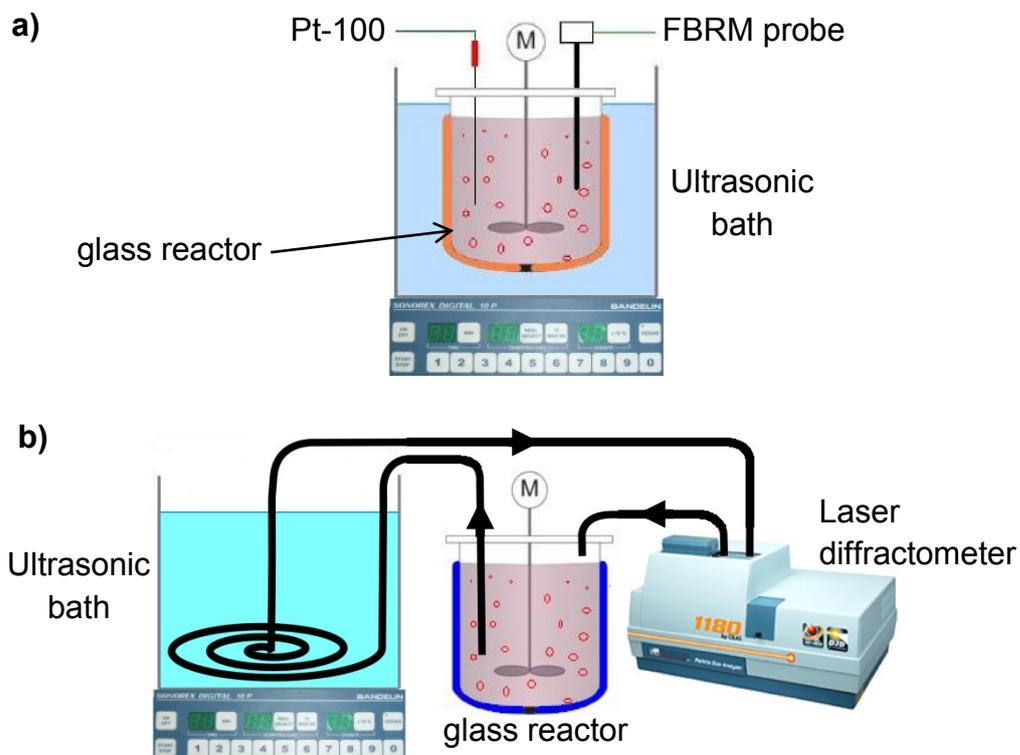


Fig. 3.4 Experimental setup for ultrasonic break-up of crystals in a) batch mode and b) continuous mode.

The experimental setup in fig. 3.4b consists of a tempered ultrasonic (US) water bath, tempered glass crystallizer and laser diffractometer. The experimental conditions were the same as these from the batch experiments. The saturated solution from the crystallizer is transported through a hose with a defined length and wall thickness into the US bath and subsequently into the laser diffractometer with the help of the peristaltic pump. The pump is embedded in the diffractometer

and not shown in the figure. A predefined amount (5 g) of already produced crystals from the respected substance was suspended in the crystallizer and their PSD measured without turning the US bath on. A sequence of experiments followed, where the suspension is continuously transported through the setup, whilst the US power was turned on for a defined period of time followed by immediate measurements of the PSD. The US output power was adjusted at 10% (48 W) of the maximum unit power for all the experiments. For calculation of the residence time of the crystals in the US bath by the experiments done in continuous mode, the following equation was used

$$\tau_{US} = \frac{V_{US}}{\dot{V}_{US}} \quad (3.1)$$

where V_{US} is the total volume of the hose inside the US bath and \dot{V}_{US} is the suspension flow.

The experiments in both setups were done three times and fairly reproducible results were obtained, discussed in section 4.3 of this thesis.

3.2.2 Experiments in single fluidized bed crystallizer

3.2.2.1 Equipment used and description of the process

The crystallization process was studied in newly developed and novel equipment, comprising one FBC. The basic idea comes from a patent, realized in 1975 by Michael Midler Jr. [Midler1975] with some improvements from our side.

The fluidized bed crystallizer has a total volume of 0.8 l and it is divided into two sections. The bottom part of the FBC has conical shape. The smallest diameter is 15 mm at the entrance. It increases up to a height $x=515$ mm, where the diameter is 30 mm, and remains constant in the tubular upper part. The conical geometry of the crystallizer offers the possibility of classifying the fluidized particles, and, more importantly, the withdrawal of a crystal suspension at a certain height, characterized by a narrow size distribution. For the withdrawal of crystal suspension, seven outlets has been provided along the height $x=1150$ mm of the FBC, where outlet I is at $x=165$ mm and outlet VII at $x=765$ mm with 100 mm pitch between outlets. A detailed scheme of the FBC is given in Fig. A1.1.

A scheme of the experimental setup with all the components necessary for the crystallization process is shown in fig. 3.5, while a photograph is given in fig. 3.6. The numbering of the common equipment's parts are the same in both figures.

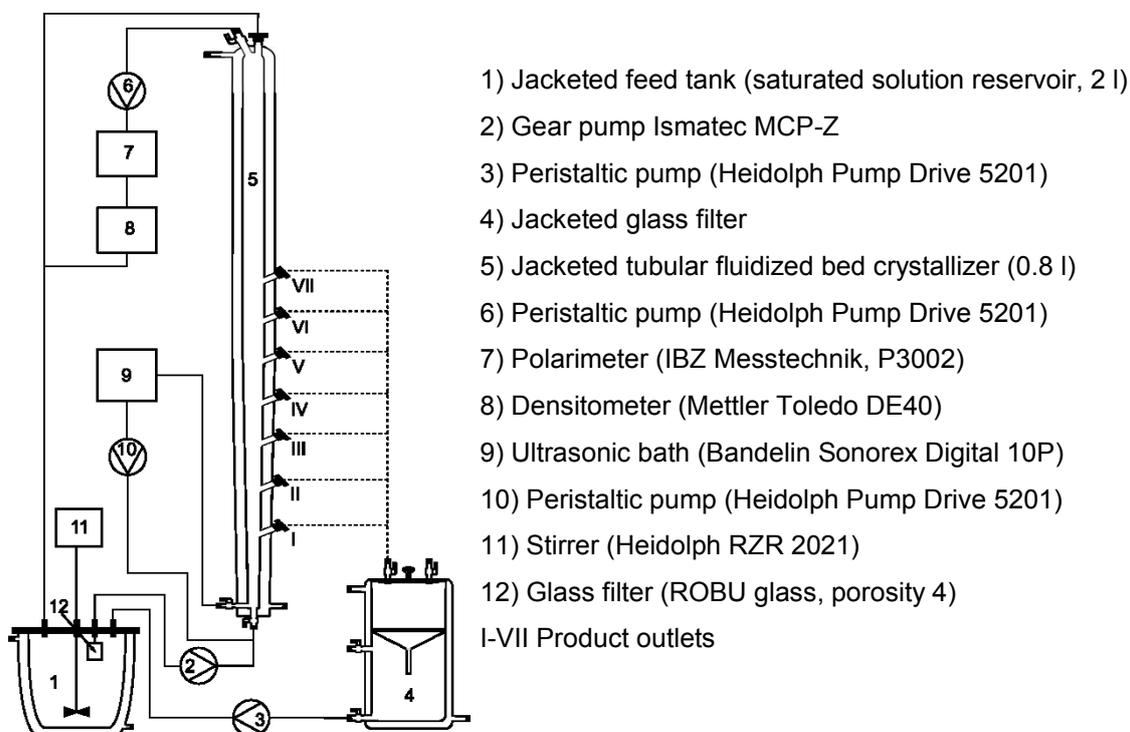


Fig. 3.5 Scheme of the fluidized bed equipment.

The equipment consists of a double jacketed feed tank (1), which is the solution reservoir with a volume of 2 l, a gear pump (2), a double jacketed home-made tubular fluidized bed crystallizer (5), a double jacketed home-made glass filter (4), three peristaltic pumps (3, 6, 10), an ultrasonic bath (9) and a stirrer (11). The connecting pipes between the feed tank and crystallizer are electrically heated, while the rest are thermo-isolated. Water bath thermostats (not shown in the figure) provide the necessary conditions for the process to be isothermally conducted with temperature control through thermocouples PT 100 (standard deviation ± 0.1 °C). A polarimeter (7) and a densitometer (8) are used to monitor the ratio of the enantiomers and the solution concentration respectively throughout the crystallization process.

An at 50°C saturated solution, containing undissolved solid particles of L-glu (saturated suspension, 2.13 wt.%) is located in the double jacketed, heated

reservoir (1). The homogenization of the solution is provided through an electric stirrer with a constant stirring rate of 250 min^{-1} (11). The solution is pumped into the bottom of a FBC (5) with the aid of a gear pump (2) at a constant flow rate through a glass filter (12). The porosity of the filter is chosen such, that on one side it ensures a constant solution flow, and on the other - the solid particles ($>16 \mu\text{m}$) remain in the feed tank. The clear, saturated solution is cooled inside the FBC to 45°C in order to become metastable or supersaturated ($c/c^* = 1.19$), while it flows from bottom to the top. The double jacket of the crystallizer maintains the temperature in the whole crystallizer volume constant. After leaving from the top of the crystallizer, the solution is fed back into the feed tank, where it is enriched by dissolution of the excess solid feed and thus becomes again saturated. A continuous flow circulation of the working solution is thus realized, where constant supersaturation in the FBC and constant saturation in the feed tank are maintained.

For collecting the product crystals, seven identical outlets are provided at the wall of the FBC. They are situated along the height of the FBC at equal distances between them, having Roman numbers (I - VII) increasing from bottom to the top. The same Roman numbering is used further in the discussion of the results in chapter 4.

Product crystals are collected in a novel jacketed glass filter (4) on a round paper-filter (Whatman 589/2). The collected filtrate is transported back to the feed tank by a peristaltic pump (3). A detailed scheme of the home-made glass filter is given in fig. A1.3.

The monitoring of the crystallization process takes place in a separate loop, where solid-free solution is pumped from the top of the FBC through a HPLC-filter by a peristaltic pump (6) and transported via a polarimeter (7) and a densitometer (8). The measurement values are continuously recorded with intervals of 1 min for the optical rotation and 5 min for solution density.

During the crystallization process, the large and heavy crystals and crystal agglomerates are continuously taken from an outlet at the bottom side of the FBC and transported by a peristaltic pump (10) into a heated ultrasonic bath (9), where a crystal comminution through ultrasonic waves takes place. Thus, seed crystals are continuously generated for the crystallization process. The

suspension is afterwards pumped back into the FBC together with the feed flow. This continuous seed-generation loop assures that the crystallization process runs continuously by providing the therefore needed seed crystals, while taking out bigger crystals and crystal agglomerates from the bottom of the FBC avoiding the clogging of the latter.



Fig. 3.6 Photograph of the equipment test setup, used to study the crystallization in fluidized bed. The numbering from figure 3.5 is used.

3.2.2.2 Crystal size distribution measurements

Throughout the duration of all experiments, crystal size distributions (CSD) were tracked and constantly measured. In order to evaluate the latter, three techniques were used and compared with each other: light microscopy, FBRM and laser diffraction. This subsection of chapter 3 focuses on the procedures, adopted for the necessary CSD measurements. Sieving was used only for preparation of seed crystals and is described in subsection 3.3.1.3 of this chapter. The CSD measurements, done with FBRM and laser diffraction are all volume based (crystal size volume distribution).

For microscopic analysis, product sample crystals were stochastically taken from the product batch immediately after the end of each experiment, rinsed with cold

ethanol and dried at room temperature. The latter were put on a microscopic glass slide without further preparation and the slide was examined under a light microscope. Crystal size measurements were done using the computer software provided (AxioVision 4.6.3) on at least 10 crystals of each sample, while microscopic photographs were taken. For the evaluation, the mean crystal size was used, based on the sum of the sizes, divided to the number of measurements.

The sample crystals, taken as a suspension by using a 10 ml syringe from the crystallizer outlets throughout the crystallization process, were immediately filtrated, rinsed with cold ethanol and dried at room temperature. The dry crystals were then subject to already described light microscopy.

For the measurements, done with the FBRM probe, no special procedures were taken. Some of the measurements were performed at the outlets of the fluidized bed crystallizer for inline crystal size tracking during the crystallization process. The measurements of the final product size distributions were performed at 25°C in a saturated solution of the respected substance. Hence, 5 grams of product crystals were then suspended and measured for 10 min under a constant stirring and temperature observation. From the apparatus software, the crystal chord length distribution was recorded and used as it is further in results and discussion part of the thesis.

For the measurements of the CSD, done with laser diffractometer CILAS 1180L in liquid mode, a saturated solution of the substance to be measured was prepared and used as a carrier medium. At the beginning of each measurement, a background signal was first measured and then the sample was introduced into the small volume unit. The latter was preferably used instead of the built-in sample container, because of the small volume of carrier medium used (120 ml, instead of 500 ml), and the need to measure small volume samples. For determination of the CSD during the crystallization process, a 10 ml syringe was used to take a 3-4 ml suspension sample probes from the outlets of the fluidized bed crystallizer, which were immediately introduced into the carrier medium. The created suspension was homogenized and after that measurement can be started. Every sample CSD was determined 3 times with almost no change in the measured values. A mean CSD was then created from the latter and used in the

discussion part of this thesis. After each measurement, the sample holder, tubing and measurement sample cell were rinsed with distilled water and ethanol to assure that the next measurement is not contaminated.

For size distribution measurements of the seeds and product crystals by laser diffraction, samples were prepared as already described in the procedure for light microscope measurements. The dried crystals were introduced into the carrier medium, the suspension was homogenized and then CSD was measured 3 times for each sample. A mean CSD was then calculated and used in the discussion part of this thesis.

3.2.3 Experiments in coupled fluidized bed crystallizer

In order to conduct a continuous preferential crystallization, coupled FBC equipment is constructed, comprising two FBCs operated simultaneously in parallel mode. This experimental setup can be seen as a combination of two single FBC setups, sharing a common feed tank. Moreover, both fluidized bed crystallizers have the same geometry as the one, used in the single FBC setup, except that only one outlet was left for the product takeout. The position of the product outlet along the height of the crystallizer was considered, based on the experimental results done in the single FBC. Other identical parts in both FBC setups are the glass filters, gear and peristaltic pumps, US bath, and the analytical equipment (polarimeter and densitometer). A scheme of the equipment is shown in fig. 3.7, while a photograph of a part of the equipment is presented in fig. 3.8.

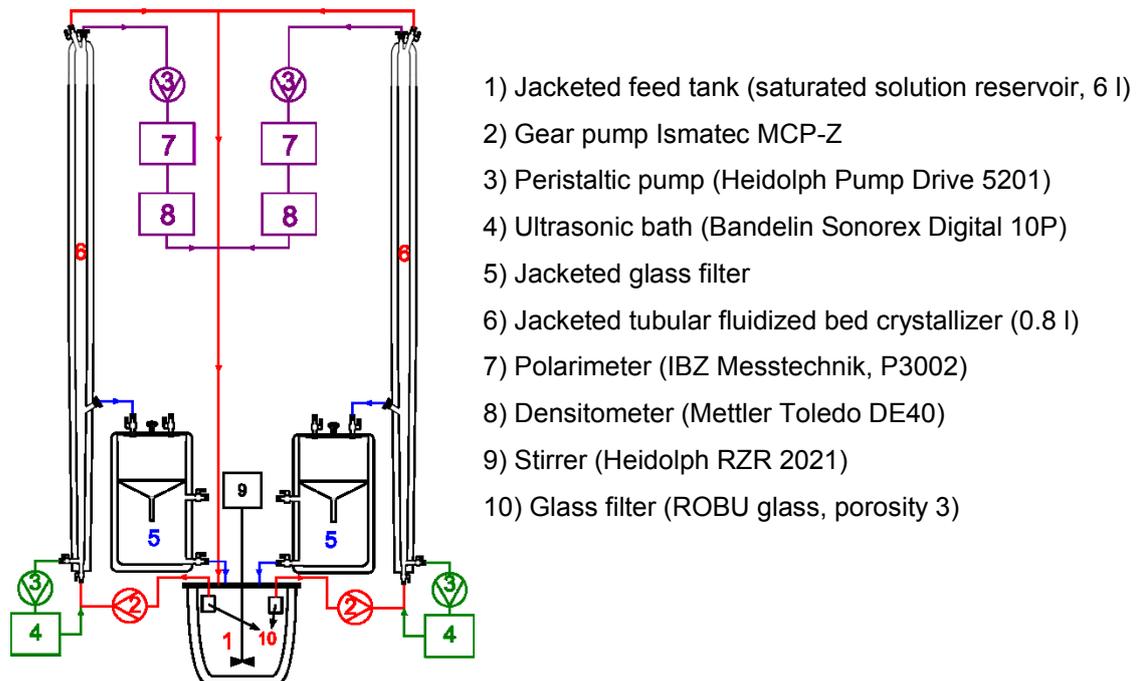


Fig. 3.7 Scheme of the coupled fluidized bed equipment.

The numbering of the common equipment's parts are the same in both figures. As seen from the figures, the setup configuration does not differ from the single FBC one. A detailed explanation of the equipment parts are already elucidated by the description of the single FBC. All connecting pipes are thermo-isolated, except these, connecting the top of the crystallizer and the feed tank, which are electrically heated. Two couples of polarimeters (7) and densitometers (8) are used to monitor the ratio of the enantiomers and the solution concentration of the each crystallizer respectively throughout the crystallization process. In order to prevent the usage of a long tubing, while maintaining lower risks of unwanted substance nucleation and high temperature deviations, the whole crystallization equipment is built as compact as possible. In order to quickly filtrate the product crystals, a vacuum pump (ILMVAC MP 601 E, not shown in fig. 3.7) was connected to the respected filter outlet situated at the middle part of each filter.

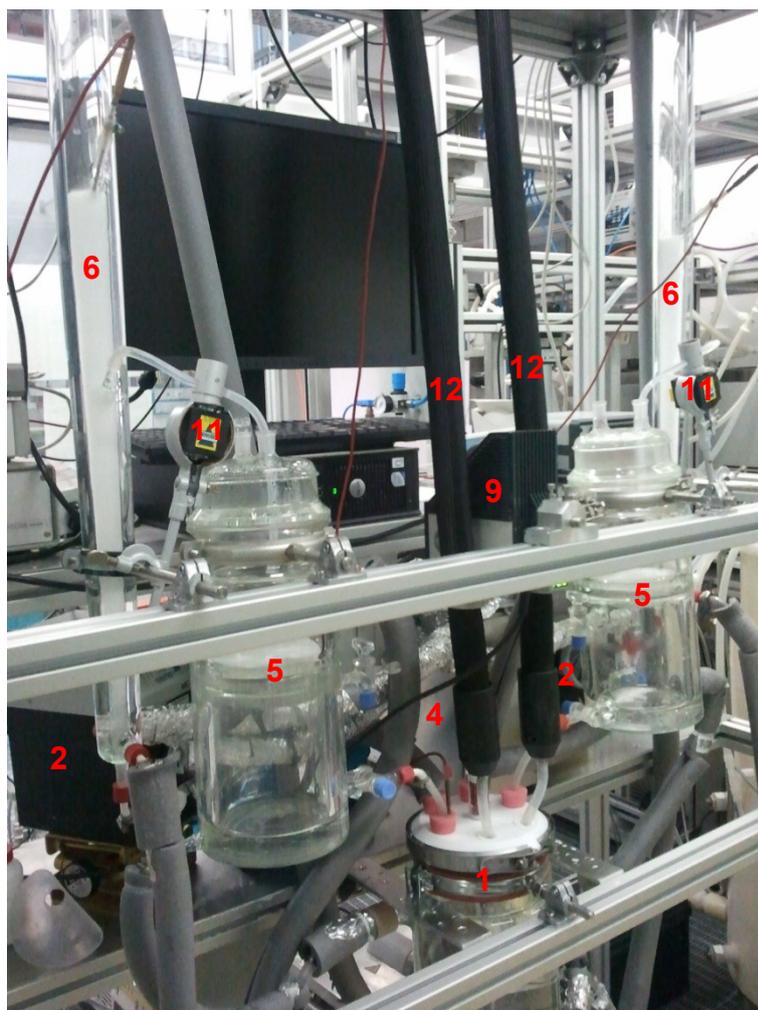


Fig. 3.8 Photograph of the equipment, used for the continuous preferential crystallization experiments. The numbering from figure 3.7 is used. Additional parts are: 11) Electromagnetic valve (Sirai S105) and 12) Heated tubing (Hillesheim, H100 T1/08).

A saturated racemic suspension (eg. DL-asparagine), containing undissolved solid particles of the substance is located in the double jacketed, heated reservoir (1). The homogenization of the solution is provided through an electric stirrer with a constant stirring rate of 250 min^{-1} (9). The solution is simultaneously pumped into the bottom of the two FBCs (6) with the aid of gear pumps (2) at a constant flow rate through glass filters (10). The porosity of the filters is chosen such, that on one side ensures a constant solution flow, and on the other - the solid particles ($>40 \mu\text{m}$) remain in the feed tank. The clear, saturated solution is cooled inside each FBC to an appropriate temperature so it becomes metastable or supersaturated, while it is flowed through from bottom to the top. The double jackets of the crystallizers maintain the temperature almost constant ($\pm 0.2 \text{ K}$) in

the whole crystallizer volume. After leaving from the top of the crystallizer, the mother liquor is recycled back in the feed tank through electrically heated pipes. Hence, the recycled solution is tempered to the reservoir temperature, thus dissolving the small crystals, taken out from the FBC with the fluid flow. The returned mother liquor is saturated in the feed tank. A double continuous flow circulation of the working solution is thus maintained, where constant supersaturation in the FBCs and constant saturation in the feed tank are maintained.

For collecting the product crystals, an outlet is provided at the wall of the FBC, corresponding to outlet III from the single FBC setup (see fig. 3.5). An electromagnetic valve (Sirai S105) connected with two optical sensors ensures the automated product extraction from the FBC. The volume of the extracted suspension is thus always constant (~ 75 ml) and the offtake process is realized in about 2 seconds. Likewise by the single FBC setup, the product crystals are collected in a jacketed glass filter on a round paper-filter.

The monitoring of the crystallization process is already described in the previous subsection.

Likewise by the single FBC setup, during the crystallization process, big crystals and crystal agglomerates are continuously taken from an outlet at the bottom side of the each FBC and transported by a peristaltic pump into a heated ultrasonic bath, where a crystal break-up through ultrasonic waves takes place. The suspension transport to and from US device is situated behind the heated tubing (12) and glass filters (see fig. 3.8). The separate representation of the latter in fig. 3.7 is done for clarity purposes. The ultrasonic comminution process is explained in detail in subsection 3.3.1.3.

3.3 Analytical techniques

Acquiring reliable information during the crystallization process and on the final product is of a great importance. The properties of the product are highly dependent on the quality of the seeds used, the presence of a specific polymorphic form and the crystal size distribution. In order to characterize the investigated material systems, precise measurements of the solution concentration and density, product purity, crystal size distribution, or to

characterize the crystal polymorph or its form, special analytical techniques and tools were employed. In this section of the thesis a detailed description on the analytical devices used will be given. The function and operation of these measurement techniques are presented in the following sections of this chapter.

- Solubility and MSZW measurements

The proper realization of the crystallization is based on the solubilities, c^* , of the substances involved in the process. One of the techniques used in this thesis is the polythermal method, based on multiple heating - cooling runs, thus dissolving the solids in the solvent with the temperature increase and further crystallizing it with the temperature decrease. A multiple-reactor system Crystal16™ (Avantium, The Netherlands) was used for this purpose, measuring the turbidity of the solution based on the cloudiness or haziness of a fluid caused by suspended solids that are generally invisible to the naked eye. It consists of four independently thermostated aluminum reactor blocks encased in a bench top setup, which are heated and cooled by a combination of Peltier elements and a cryostat, where the necessary heating and stirring rates were predefined using the apparatus software. An exemplary scheme of the principle is shown in Fig. 3.9a. The reproducibility of the solubility measurements was studied carrying out at least 3 runs under same conditions. The measured sample solutions / suspensions are inserted in HPLC-vials with a maximal volume of 1 ml. Magnetic stirrer is also inserted in every vial in order to ensure a proper homogenization.

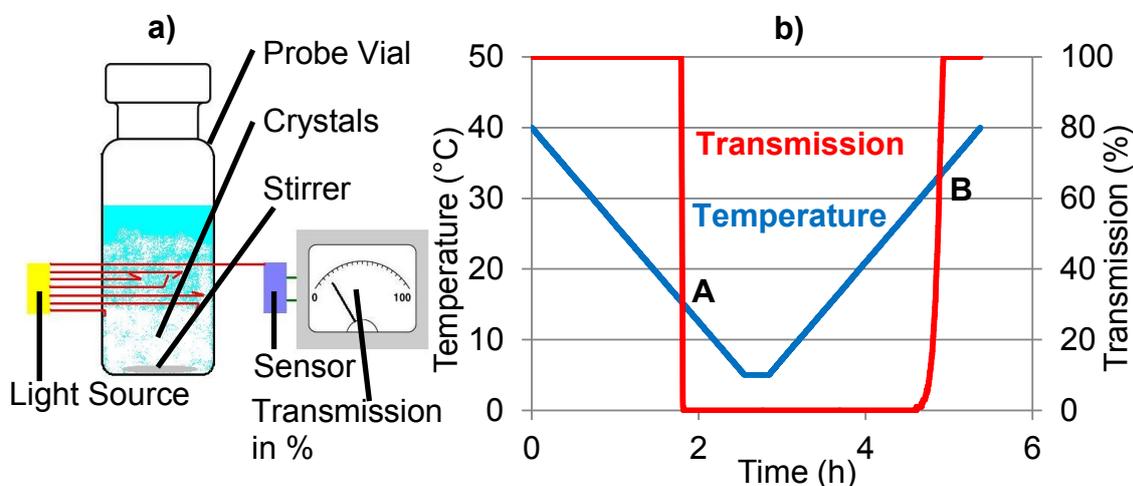


Fig. 3.9 a) Schematic representation of the Crystal16™ principle; b) example of turbidity measurement.

The turbidity was recorded per individual reactor and as seen from fig. 3.9b the disappearance of last crystals (“clear point”, point B) or the appearance of the first crystals (“cloud point”, point A) can be detected. Respectively, both intersection points are used to identify the saturation temperature T_{sat} and crystallization temperature T_{nucl} of the measured sample. Thus after measuring several samples of one substance, the solubility as well as metastable zone width can be specified as the area between the saturation temperatures and crystallization temperatures.

- *Laser diffraction*

In the crystallization processes, one of the important product parameters is the crystal size distribution. In this thesis several methods were applied for measurement of particle size distributions. One of the methods is based on laser diffraction analysis. CILAS 1180L (Quantachrome GmbH & Co., Germany) was used as a laser diffraction analyzer for the determination of the particle distributions within a measurement range from 0.04 to 2.500 μm , while maintaining an extremely small footprint.

The function of the laser diffractometer is relatively simple. The measurement principle is based on the diffraction of the laser beams by the particles. When a particle occurred on the laser beam path, the beam is bent according to particle size and the resulting ring patterns are referred to as Fraunhofer's diffraction rings. Large particles possess a pattern with large Fraunhofer diffraction rings and narrow diffraction angles, while small Fraunhofer diffraction rings and large diffraction angles are generated by the detection of small particles. Thus, to characterize the size of a particle, it is exploited in the software evaluation, that the size of the diffraction angle is inversely proportional to particle size. The structure of a laser diffraction device is shown in the following Figure 3.10.

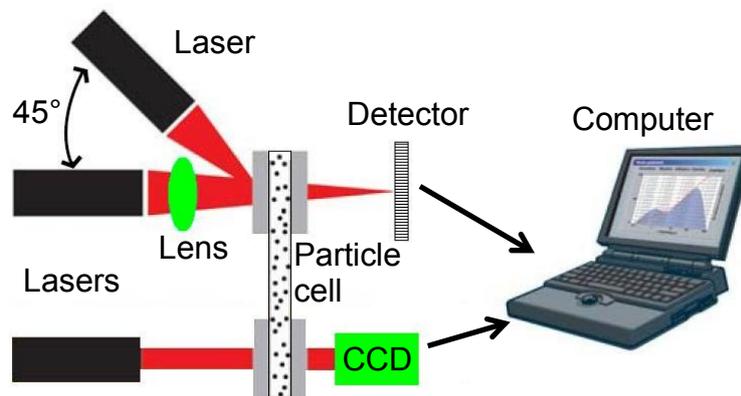


Fig. 3.10 Principle of laser diffraction device CILAS 1180L for particle size determination combined with software interface [adapted from Xu2002].

The device consists of several light sources (lasers) and a lens system for widening the narrow laser beams. This ensures that the entire sample can be illuminated. The substance to be measured is located in a measuring cell, which consists of a frame made of glass. The laser beams are combined and passed through a Fourier lens to a detector system. Recording the diffraction pattern is carried out with suitable software, which is also used to calculate the particle size distribution.

The calculation of the particle size is relatively complex, since the sample consists of not only one particle, but delivers a full set of data from different particle sizes. Thus, a superposition of the different diffraction patterns is characterized, referred to as interference. Through the software, the particle sizes are determined by an algorithm through iteration from possible particle sizes, and thus the interference pattern can be calculated. This process is repeated until the calculated pattern coincides with the one, derived from the measurement.

The output of the particle sizes is carried out by a distribution curve (so called q_3 distribution) in which the volume is given in % of the particle size in microns. Along with the distribution, different populations of particles can be represented. If it is a mono-modal curve, the sample contains only one particle population. However, if the curve is bi- or multimodal, it consists of several particle populations. Furthermore, some specific parameters can be specified, based on the particles diameter, alternative to the graphical representation of the measurement result. One of them is the mean diameter d_{50} of the particle population. It specifies at which particle size 50% of the particles are smaller than

the delivered result. Further parameters are d_{10} as a measure of the small particles and d_{90} for the large particles in the measured substance. If both parameters, d_{10} and d_{90} , are close together, the particle size distribution is narrow [Xu2002].

- *Density*

In order to optimally conduct a crystallization process, changes of the concentration of the targeted material in the solution should be regularly monitored and registered within the process course. This can be achieved by using several methods. In this thesis, the determination of the solution density, ρ_f , was realized with a densitometer (Mettler Toledo DE40). The solution density determination depends on the measurement temperature and the solution concentration. The principle of measurement of the density measuring device is based on the electromagnetically induced vibration of a U-shaped glass tube with a defined volume and it is shown in figure 3.11. The tube vibrations correspond to an oscillation period and this period is referred to as T_o , where the frequency f [s^{-1}] is the number of periods per second, see eq. 3.2.

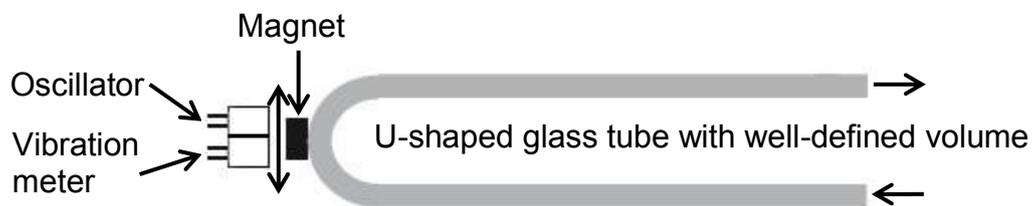


Fig. 3.11 Measuring cell of a densitometer.

$$f = \frac{1}{T_o} \quad (3.2)$$

The glass tube possesses a characteristic or natural frequency, which changes when the tube is filled with a gas or liquid. The frequency of the tube is a function of the sample mass. Thus, when the mass increases, the frequency decreases. As seen in fig. 3.11, a magnet is connected to the tube, which through the oscillator generates an electric signal from the tube vibrations. The so generated signal is detected by the vibration meter. The oscillation period is specified with the following eq. 3.3.

$$T_o = 2\pi \sqrt{\frac{\rho_f V_t + m_t}{K_c}} \quad (3.3)$$

where ρ_f is the solution density in the tube, V_t is the tube volume, m_t – the mass of the tube and K_c is a measuring cell constant. Equation 3.3 can be rewritten in order to evaluate the density

$$\rho_f = af^2 + b \quad (3.4)$$

where a and b are constants, determined by the mass, structure, and elasticity of the tube. As these tube properties can be different for every device, the constants must be determined by calibration measurements of air and water at a specific temperature. As the density of both at this specific temperature is already known, the constants a and b can be calculated.

By the continuous density measurements, the values for the oscillation period can slightly vary, because of the permanent flow through the measuring cell. Thus a mean value of the frequency f is taken based on at least three values calculated with eq. 3.2.

- *Focused Beam Reflectance Measurement (FBRM).*

A useful in-line tool for measuring not only crystal size distributions, but also crystal growth and metastable zone width (detection of nucleation) in the crystallizer, a FBRM probe (FBRM 400S, Mettler Toledo) was used. FBRM is an abbreviation for Focused Beam Reflectance Measurement. The measuring principle of the in-line probe is based on the reflection of a focused, rotating laser beam in a circular orbit from the crystals in the crystallizer and the detection time of the resulting reflection. The scheme of the probe and the measurement principle are shown in figure 3.12. The measurement range of the equipment used is between 0.5 μm and 2000 μm .

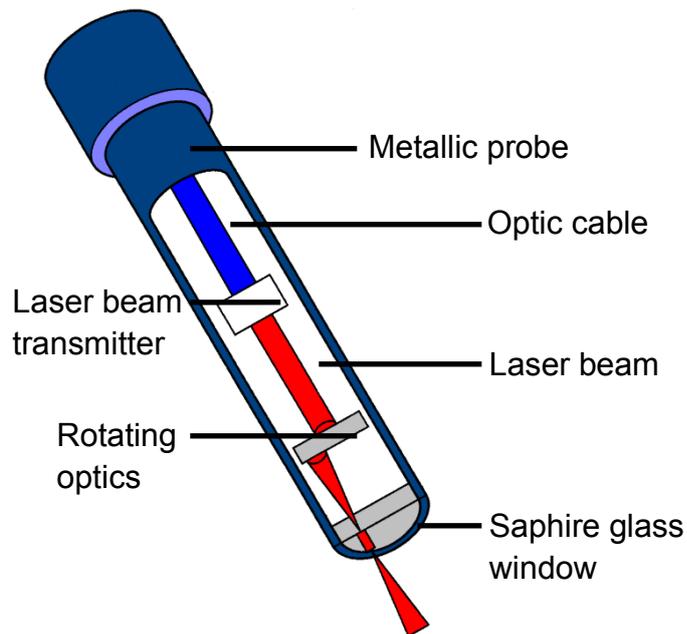


Fig. 3.12 Measurement principle and a profile of a FBRM probe.

The laser beam illustrated in figure 3.12 is rotating on a circular path. Meanwhile, it samples at a constant rate moving particles at the probe window. The reflected laser pulses from the surface of the individual particle is then counted by a special optical system and a transmitter. From the speed of the rotating optics (2 m/s) and the measured reflection time, the chord length of the reflecting crystal can be calculated. This allows for a sufficient number of crystals in the crystallizer the determination of a crystal population characteristic chord length distribution. The measured chord length distribution is affected by a variety of factors, like: crystal shape and size, hydrodynamic conditions at the probe window, homogeneous mixing of the particle sizes in the crystallizer as well as the position and the angle of the probe in it. The evaluation of measured chord length distribution and transforming it into a particle size distribution is realized through a comparison with alternative sizing techniques, such as laser diffraction and microscopy.

- *High-Performance Liquid Chromatography (HPLC)*

The determination of the purity of the initial substances and the product crystals is performed through HPLC measurements using HPLC 1200 Series equipment. HPLC is an abbreviation for High-Performance Liquid Chromatography. In this

physicochemical separation process, a sample is separated to its components along a column, filled with adsorbent. Moreover, the substances involved can be identified, quantified, and thus, the purity can be determined.

The basic setup of a HPLC system is shown in figure 3.13. Before the measurement, the solid substance to be investigated is dissolved in an appropriate solvent to form a homogeneous liquid phase. It is then injected together with the mobile phase (eluent, responsible for transport) in a separation column with the help of a pump (see Fig. 3.13). The temperature-controlled column contains a stationary phase, where the separation process is carried out isothermally. After the separation, the sample components are collected as they emerge from the column. A detector analyzes the emerging stream by measuring a property, which is related to concentration and the chemical composition. For example, the refractive index or ultra-violet absorbance is measured. At the end of the process a chromatogram is built, based on the collected information from the detector by using a PC recorder. After the detection, the substances are collected in a waste reservoir.

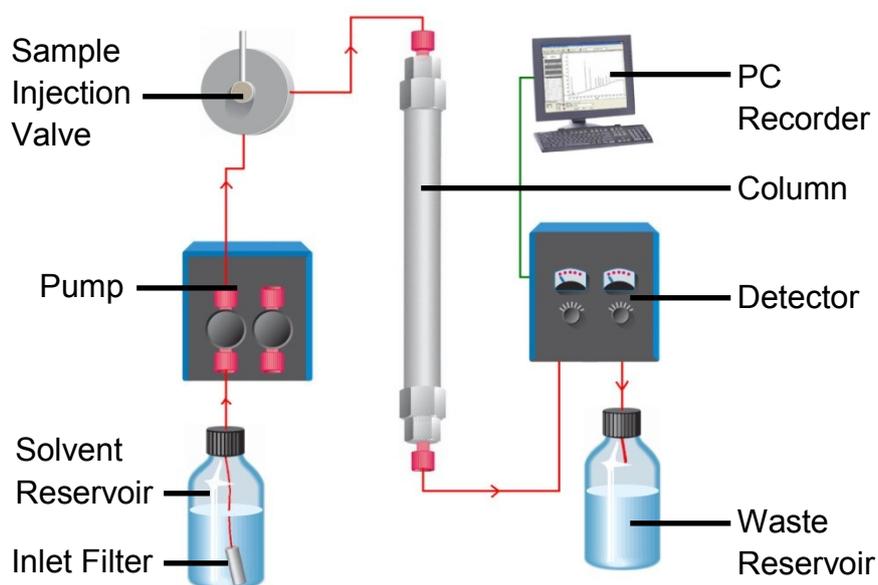


Fig. 3.13 Principle setup of a HPLC device.

The separation of the components is based on the specific interactions with the adsorbent in the chromatographic column. The spherical porous adsorbent material usually consists of chemically easily modifiable silica gel particles with a

mean size of 4 to 10 μm . In the case of the separation of chiral substances, like enantiomers, the filling of the column should be made from an optically active material [Mayer2004].

The HPLC measurement conditions of the substances used in this work are shown in table 3.4.

Table 3.4 Measurement conditions and chromatographic columns used in this work.

Substance	Asparagine	Glutamic acid	Aminobenzoic acid
Equipment	Agilent HP 1100	Agilent HP 1100	Agilent HP 1200
Detector	DAD	DAD	UV
HPLC column	Astec Chirobiotic T	Astec Chirobiotic T	Kinetex C18
Mobile phase	EtOH / H ₂ O 30 / 70	MeOH / H ₂ O / HCOOH	ACN / H ₂ O 80 / 20
Stationary	Teicoplanin / silica	Teicoplanin / silica	reverse C18 with
Flow rate	0.5 ml/min	0.5 ml/min	0.5 ml/min
Injection	5 μl	20 μl	1 μl

- Polarimetry

Optically active samples, such as solutions of chiral molecules, often exhibit circular birefringence. It causes rotation of the polarization of plane polarized light as it passes through the sample. Thus, polarimetry can be used for the quantitative determination of angle of rotation of such optically active substances. In this work, for the tracking of the optical rotation, a digital automatic online polarimeter P3002 of the company IBZ Messtechnik was used. The dependence of the specific optical rotation $[\alpha]_{\gamma}^T$ at a wavelength γ and a temperature T is defined with the following eq. 3.5.

$$[\alpha]_{\gamma}^T = \frac{\alpha}{lc} \quad (3.5)$$

where α is the optical rotation angle of the sample, l – length of the sample tube and c – mass concentration of the sample. As seen from eq. 3.5, in the presence of just one enantiomer in the solution, concentration measurements are possible by this measurement method at a constant temperature. During the measurement, the rotation angle changes the linearly polarized light of the chemical sample. This property is referred to as intrinsic property of chiral non-racemic compounds or mixtures. By the polarimeter each enantiomer can be

determined or the crystallization can be monitored. The measurement principle of a polarimeter is shown in fig 3.14.

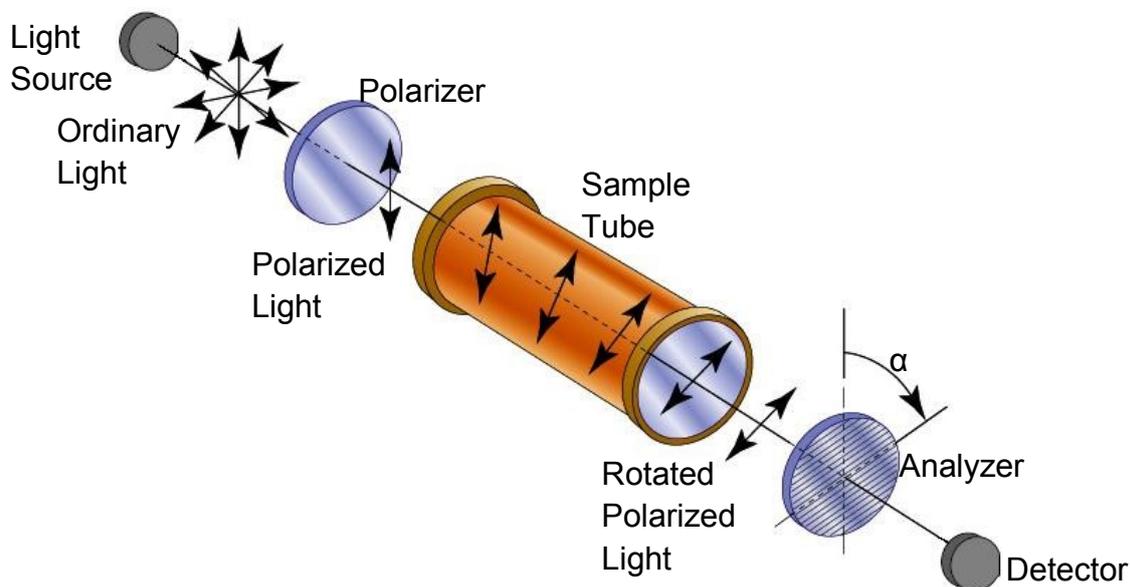


Fig. 3.14 Measurement principle of a polarimeter for determining the angle of rotation.

As can be seen in figure 3.14, the polarimeter is composed of a light source, which radiates ordinary light; a polarizer, which polarizes the light so it has only one plane of vibration; a sample tube, where the plane polarized light is rotated by the substance solution; an rotatable analyzer, which, combined with the detector, measures the rotation angle α by the maximum light passage through the analyzer. In preferential crystallization, the continuous measurement of the ratio of both enantiomers in the solution is of great importance in order to achieve optimum results for process productivity and product purity. By the measurement of solutions of enantiomers, if the analyzer rotates through its adjustment to the right, then the enantiomer, referred to as right-handed and designated with a (+), is in excess in a solution. On the contrary, if the rotation of the analyzer is to the left, the enantiomer in excess is left-handed and designated with (-). Generally, for estimation of enantiomer excess (%) in a solution, the following equation can be applied [Soderberg2012]:

$$ee\% = \frac{\text{specific rotation of the solution}}{\text{specific rotation of the pure enantiomer}} \times 100 \quad (3.6)$$

- *Ultraviolet–visible spectrophotometry*

A robust method for offline as well as online tracking of concentration changes along the crystallization process is UV-visible spectroscopy. In this thesis, an ultraviolet detector (Knauer, K-2501) was used to monitor the continuous crystallization of *o*-aminobenzoic acid. In solution, it is well known for absorbing the UV-light [Takara2005]. Most of the absorption in the ultraviolet spectroscopy occurs due to π -electron transitions or n -electron transitions. When these electrons are irradiated with light energy, that is more or equal to the energy, needed for a possible electronic transition within the molecule, then some of the light energy would be absorbed by the molecule and the electrons would be promoted to the higher energy state orbital. The UV-spectrometer can record this degree of absorption at different wavelengths and can plot the absorbance versus wavelength (a spectrum plot). The wavelength at which the sample absorbs the maximum amount of light is known as λ_{\max} . For example, in fig. 3.15 is shown the spectrum of *ortho*-aminobenzoic acid, recorded on a Genesys™ 6 UV-VIS spectrophotometer (Thermo Electron Corp.). Aqueous solutions of aminobenzoic acid have light brown to dark brown color, depending of the sample concentration and have a λ_{\max} of 310 nm.

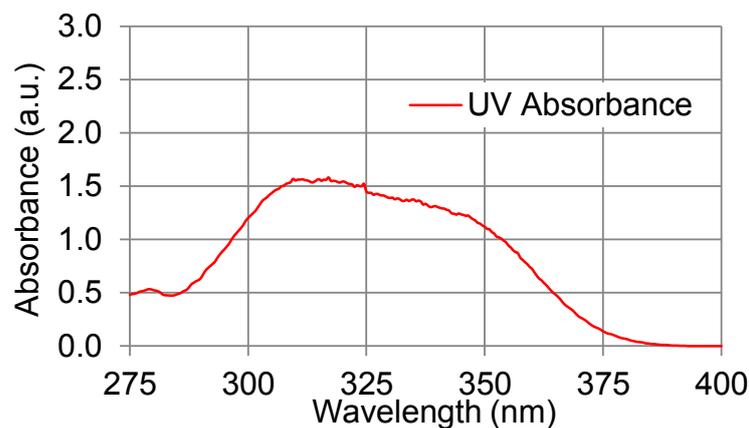


Fig. 3.15 UV-absorbance spectra for *ortho*-aminobenzoic acid (0.1 wt.%).

For the dependence of the light absorbance and sample concentration, the Beer–Lambert law can be applied:

$$A = \log_{10} \left(\frac{I_0}{I} \right) = K \epsilon \cdot c \cdot l \quad (3.7)$$

in the equation A is the measured absorbance, I_0 is the intensity of the light at a given wavelength, I is the transmitted intensity, l_s is the pathlength through the sample, and c is the concentration of the sample. The constant $K\varepsilon$ is the extinction coefficient, which is specific for each solvent and wavelength used [Hill1999].

- *X-ray powder diffraction*

Some of the fine chemicals, used in the industrial production, occur as polymorphs of the mere molecule, solvates and hydrates, molecular salts and co-crystals [Beckmann2013]. Thus, it is of great importance to know not only the exact nature of the material in the process, but also its stability with time, the variability of its chemical and physical properties as a function of the crystal form, etc. The search for and characterization of crystal forms is therefore a crucial step in the development of new chemicals. Powerful solid-state techniques, such as hot stage microscopy, differential scanning calorimetry, thermogravimetric analysis and X-ray diffraction can be used to get information about the solid state properties of the substance. The screening method used in this thesis is X-ray powder diffraction (XRPD). It is a rapid analytical technique primarily used for phase identification of a crystalline material and can provide information on unit cell dimensions. Before the analysis, the material should be finely ground and homogenized. The X-ray diffractometer consist of three basic elements: an X-ray tube, a sample holder, and an X-ray detector, see fig. 3.16.

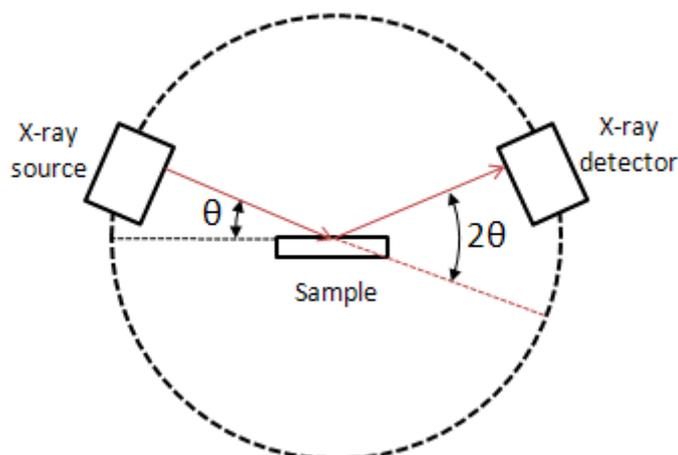


Fig. 3.16 Principle of the X-ray diffraction measurement. [adapted from Scoog2007].

X-rays are generated in a cathode ray tube by heating a filament to produce electrons, accelerating the electrons toward the sample by applying a voltage, thus bombarding it with electrons. When electrons have sufficient energy to dislodge electrons of the sample, characteristic X-ray spectra are produced. It is required to produce monochromatic X-rays needed for diffraction, using specific wavelengths, characteristic of the target material (Cu, Fe, Mo, Cr). Copper is the most common target material for single-crystal diffraction, with Cu K α radiation = 1.5418Å. The sample is rotated in the path of the collimated X-ray beam at an angle θ while the X-ray detector is mounted on an arm to collect the diffracted X-rays and rotates at an angle of 2θ . For typical powder patterns, data is collected at 2θ from $\sim 5^\circ$ to 70° , angles that are preset in the X-ray scan [Braga2009].

The XRPD patterns for all substances used were measured with an X'Pert Pro Diffractometer (PANalytical GmbH, Germany) using CuK α radiation and an X'Celerator detector. The patterns were recorded in a 2θ range of $3\text{--}40^\circ$, with a step size of 0.0167° and a counting time of 50 s per step. Powder patterns for the substances used in this thesis are given in Appendix A2.

4. Results and discussion

This chapter is separated into six sections. In the first section 4.1, a simplified dynamic model of the crystallization process in a fluidized bed is proposed as a basis for future work. The results from the solubility of the pure substances in water are elucidated in the second section 4.2, where own measured data are compared with known results from the literature. In section 4.3, results from the seed generation by using ultrasonic crystal breakage will be shown. In section 4.4, results from crystallization experiments done in a single fluidized bed crystallizer will be presented. The discussion will begin with the fluidized bed process and will be extended by implementing selected data from sections 4.2 and 4.3. The influence of feed rate, seed size, and ultrasonic crystal breakage on the crystal size distributions will be discussed in the following subsections. In section 4.5, continuous preferential crystallization of asparagine monohydrate and aminobenzoic acid in two coupled fluidized bed crystallizers will be discussed. The experimental results, concerning residence time, crystal size distributions and solution concentration development, will be compared with results from the simplified dynamic model. Based on the conducted experiments in both experimental setups, recommendations for possible improvements of the equipment applied are suggested in section 4.6.

4.1 Simplified dynamic model of the fluidized bed crystallization process

In chapter 2.3.4, it was shown the position of a single spherical particle in dependence on its diameter can be calculated from the steady state force balance model. It was assumed that the diameter of the fluidized particle was constant, i.e. no growth or dissolution takes place. If a crystallization process is added to fluidization process, then it can be assumed the fluidized particle (or as in our case, the fluidized crystal) increases its volume (or diameter) due to the mass transfer of the substance from the up-flowing solution to the crystal surface. Rahaman et al. have proposed a model, where crystallization kinetics is combined with crystallizer hydrodynamics [Rahaman2014]. The model takes care

of supersaturation generation, crystal growth and crystal segregation. Randolph and Larsen developed a method of modeling continuous crystallizers in which the growth rate is independent of size and the slurry is uniformly mixed [Randolph1988]. Such crystallizers are often referred to as the mixed-suspension mixed-product removal (MSMPR) type.

In our case, during the process seed crystals are generated from ultrasonic fragmentation of crystals and crystal agglomerates. The main effects being reflected in the population balance model are crystal growth, segregation due to different particle sizes, particle withdrawal to the ultrasonic attenuation, and reflux of small particles from the ultrasonic attenuation. The following model results in a two dimensional population balance model for the particle size distribution $n(x, L)$ as proposed within the cooperation with the group of Dr. Stefan Palis and Prof. Achim Kienle [Palis2013]. In a first step the crystal fraction is characterized by one internal coordinate, the characteristic length, L , and one external coordinate, x , associated with the crystallizer geometry. For the segregation, the Richardson-Zaki steady state force balance model is applied. The ultrasonic attenuation model is derived assuming quasi-stationary operation and a defined particle size distribution of the size reduced particles. For the liquid fraction, i.e. the solution, plug-flow along x is assumed resulting in a one dimensional partial differential equation for the solution concentration.

In order to simplify the crystallization modeling the following assumptions are made:

- 1D model in axial direction,
- $\dot{V} = \text{const}$, plug flow,
- isothermal conditions,
- nonporous, spherical particles,
- size-independent growth rate,
- no nucleation, no breakage, no agglomeration,

In Fig. 4.1 is shown a scheme of a model crystallizer with height H and cross-section A . The fluid (or the liquid solution) flows at a constant flow rate \dot{V} and has concentration c^* at the bottom of the crystallizer ($x=0$). The solution leaves the crystallizer from the top ($x=H$) with a concentration $c_H^* < c^*$. Seed crystals with

diameter L° are given at the top of the crystallizer ($x=H$) and product crystals with diameter $L_p > L^\circ$ are withdrawn at the side of the crystallizer ($x=x_p$). At the bottom of the crystallizer crystals with diameter L_{US} are withdrawn, comminuted in an ultrasonic bad and brought back as seeds of size L_{US}° . The crystal sizes in the crystallizer are limited by the condition $L^\circ < L < L_{US}$.

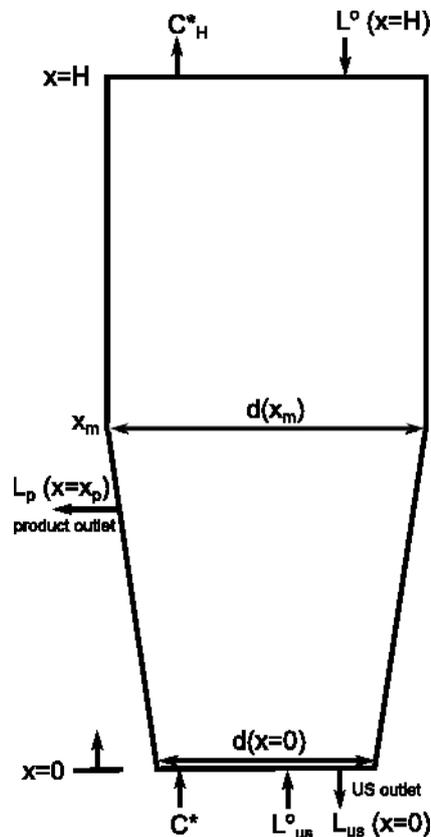


Fig. 4.1 A scheme of the model crystallizer.

The crystallizer diameter, d , corresponds to the one from the experimental setup (see details in chapter 3.2.2 and in Fig. A1.1), and its distribution is given by

$$d(x) = \begin{cases} \frac{d(x_m) - d(x=0)}{x_m}x + d(x=0), & \text{for } x \leq x_m \\ d(x_m), & \text{for } H > x > x_m \end{cases} \quad (4.1)$$

where $d(x_m) = 30$ mm, $d(x=0) = 15$ mm, $x_m = 515$ mm, $x_p = 365$ mm, and $H = 1100$ mm.

The behavior of the solid phase with time, i.e. the particle number distribution, n , in the fluidized bed crystallizer can be described by the following population balance [Randolph1988]

$$\frac{\partial n(x, t)}{\partial t} = -\frac{\partial(G(x)n(x))}{\partial L} - \dot{n}_{\text{prod}} + \dot{n}_{\text{seg}}(x) + \dot{n}_{\text{bm}}(x) - \dot{n}_{\text{out,us}} + \dot{n}_{\text{in,us}} \quad (4.2)$$

where \dot{n}_{prod} is the particle flux due to product removal, \dot{n}_{seg} is the particle flux due to segregation, \dot{n}_{bm} is the particle flux due to back mixing, $\dot{n}_{\text{out,us}}$ and $\dot{n}_{\text{in,us}}$ are the particle fluxes to and from the ultrasonic attenuation, and G is the local growth rate depending via the locally changing liquid phase concentration and the position x :

$$G(x) = k(c(x) - c^*) \quad (4.3)$$

Assuming no nucleation and solid free fluid flow from the pump the following boundary conditions hold.

$$n(x = 0, L, t) = 0 \quad (4.4)$$

$$n(x, L = 0, t) = 0 \quad (4.5)$$

The liquid phase can be described by the following partial differential equation for the concentration c .

$$\frac{\partial c}{\partial t} = c \frac{\partial u_f}{\partial x} + u_f(x) \frac{\partial c}{\partial x} - \frac{4}{3} \pi \int_0^\infty \left(\frac{L}{2}\right)^2 \frac{\partial G}{\partial L} dL \quad (4.6)$$

Here, the first two terms account for convective flux due to fluid flow and the third term for the decrease of concentration due to particle growth. At the lower boundary, the concentration can be assumed to be constant, i.e. $c(x = 0) = c^*$.

The solid phase, present in the liquid-free part of the crystallizer, expressed by the fraction $(1 - \varepsilon)V_{\text{cr}}$, can be quantified evaluating the overall growth and total particle quantity, N :

$$\frac{\partial m_s}{\partial t} = NV_{\text{cr}}(1 - \varepsilon)\rho_p \frac{4}{3} \pi \int_0^\infty \left(\frac{L}{2}\right)^2 \frac{\partial G}{\partial L} dL \quad (4.7)$$

After a modification, equation 4.7 can be used for the estimation of the particle flux due to product removal, \dot{n}_{prod} , at the product outlet at a specific height, x_p ,

$$\frac{\partial m_p(x_p)}{\partial t} = N_{\text{cr}} \dot{V}_{\text{cr}} (1 - \varepsilon) \rho_p \frac{4}{3} \pi \left(\frac{L_p}{2} \right)^2 \quad (4.8)$$

where \dot{V}_{cr} represents the taken out product suspension volumetric flow rate and N_{cr} is the particle quantity in the product suspension. It was empirically assumed to be one third of the total particle quantity, N ($N_{\text{cr}} = N/3$).

In order to derive the particle flux due to segregation \dot{n}_{seg} , the Richardson-Zaki force balance model is used by taking into account equation 2.28 and assuming quasi-stationary particle motion (or equilibrium conditions). Then for the fluid flow can be assumed: if $u_p > u_f$ a particle with radius L will sink, otherwise for $u_p < u_f$ a particle with radius L will rise. Due to variations in the effective area $A_{\text{eff}}(x)$ in the conical section ($x \leq x_m$), the fluid velocity u_f varies in this section

$$u_f(x) = \frac{\dot{V}}{A_{\text{eff}}(x)} \quad (4.9)$$

The effective area $A_{\text{eff}}(x)$ depends simply on the crystallizer geometry and the bed voidage, ε .

$$A_{\text{eff}}(x) = A(x) - A(x, \varepsilon) = A(x) - \pi \int_0^{\infty} L^2 n(L, x, t) dL \quad (4.10)$$

Using the single particle velocity $u_p(x, L)$, the particle flux due to segregation can be calculated as

$$\dot{n}_{\text{seg}} = \frac{\partial u_p(x, L) n}{\partial x} \quad (4.11)$$

In order to account for local back mixing inside the fluidized bed, a diffusion-like particle flux has been included.

$$\dot{n}_{bm} = D \frac{\partial^2 n}{\partial x^2} \quad (4.12)$$

where D is the diffusion coefficient of the studied substance.

For the seed generation in the ultrasonic bath, it can be assumed that no particle growth or dissolution occurs in sufficiently large residence time, thus a certain constant particle size distribution can be achieved. In a first step the ultrasonic attenuation can be modeled as a mass conserving size reduction process, given by

$$n_{us}(L) = N \exp\left(-\frac{L_{US} - L_{US}^0}{G \tau_{US}}\right) \quad (4.13)$$

where τ_{US} is the mean residence time in the US-bath. Equation 4.13 describes an exponential increase of the total particle density due to the comminution of crystals in the US-bath in accordance with their residence time and linked with the growth rate. In general, bigger crystals have longer residence times and vice versa. Furthermore, it was assumed that the size of the generated from US seed crystals is equal to the size of the initial seeds $L_{US}^0 = L^0$.

Hence, the particle flux from the ultrasonic attenuation being supplied to the crystallizer at height $x = 0$ is given by

$$\dot{n}_{in,us} = \frac{\int_0^\infty L^3 \dot{n}_{out,us} dL}{\int_0^\infty L^3 n_{us} dL} n_{us}(L) \delta(x = 0), \quad (4.14)$$

where δ is the Dirac delta distribution and $\dot{n}_{out,us}$ is the particle flux withdrawn from the crystallizer at height $x = 0$

$$\dot{n}_{out,us} = K_{us} \delta(x = 0) n(x, L, t). \quad (4.15)$$

The introduced model was solved numerically in Matlab® using simple explicit finite differences to approximate the derivatives. To ensure numeric precision, the number of grid points was varied in a broad range and no significant differences were found. Computational results for the solution concentration development

(eq. 4.6) in the crystallizer as well as total and recovered crystal product mass (eqs. 4.7 and 4.8 respectively) with time were derived. In order to use the proposed model there are parameters, which should be determined experimentally. Concerning the physical properties (e.g. crystal density) of the substance, these are already known and can be taken from the literature. On the contrary, some parameters like substance solubility are more complex and depend on the physical and chemical properties of the solute and solvent as well as on temperature, pressure and the pH of the solution.

To quantify the studied process in particular, profound knowledge of the solubility equilibria along with the metastable zone width (MSZW) of the substance to be crystallized is needed.

4.2 Solubility equilibria and metastable zone width determination

- Solubility equilibria and MSZW of the glutamic acid system

Solubilities of D-glu, L-Glu and DL-glu.H₂O in water were determined by using a polythermal method (described in chapter 3.3.1.1) in the temperature range 20°C – 65°C. The dependence of the saturation concentrations as a function of temperature is represented in Fig. 4.2. The concentration entity is given in mass percent (wt.%). It represents the mass of the substance multiplied by 100 and divided by the mass of the solution.

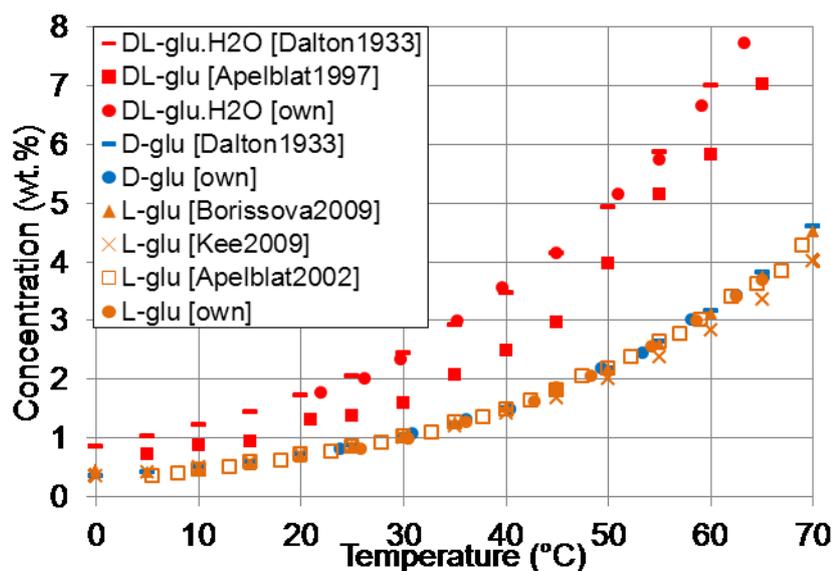


Fig. 4.2 Solubility of L-glu, D-glu, DL-glu and DL-glu.H₂O as a function of temperature (wt.% - weight percent) (own and literature data).

It can be seen from the figure, a positive slope of the solubility curves is observed, i.e. the solubility of the species increases in an exponential dependence on the temperature. The measurements of L-glu and D-glu solutions fit almost perfectly to literature data and show identical progression. On the contrary, the literature data presented for DL-glu show a considerable difference in absolute values. In a comparison of the solubility data of the pure enantiomers and DL-glu.H₂O data from Dalton and Schmidt, it can be noted that the solubility of the DL-form is greater than the corresponding values for the enantiomer form. They also reported that they have obtained DL-glu.H₂O by racemizing D-glu with barium hydroxide in an autoclave [Dalton1933]. Our solubility measurements of DL-glu.H₂O are in very good agreement with the results from Dalton and Schmidt, while the results published by Apelblat for the glutamic acid racemate are used later for constructing the Van't Hoff plot. A single probe of an aqueous solution of both enantiomers with 50:50 ratio was measured at 50°C by using an isothermal method (described in chapter 3.3.1.1). The result for the measured by HPLC saturation concentration (3.91 wt.%) fit almost perfectly with the data from Apelblat.

As seen in fig. 4.2, the solubilities of the enantiomers are lower than the solubilities of the racemate in the glutamic acid system. For the ideal case, the solubility of the conglomerate racemic solution equals the sum of the solubilities of the single enantiomers. In our case, with increase of temperature, the solubility ratios between the racemic mixture (data from Apelblat) and the pure enantiomers change from ~1.78 at 10°C to ~1.84 at 65°C. A comparison with solubility data from Dalton and our measurements of DL-glu.H₂O with the glutamic acid enantiomers show ratios from 2.45 at 10°C to 2.19 at 65°C between the DL-form and the pure enantiomers. The van't Hoff plot (shown in Fig. 4.3) gives a good linearization and the slopes for the 3 species are very similar.

The trend lines, shown in figure 4.3, correspond to the solubility data of DL-glu, D-glu and L-glu, and are represented as a natural logarithm of the molar concentration of the respective substance versus the absolute reciprocal temperature. Based on the data, the van't Hoff equation can be written by using the two parameters, A and B, listed in Table 4.1.

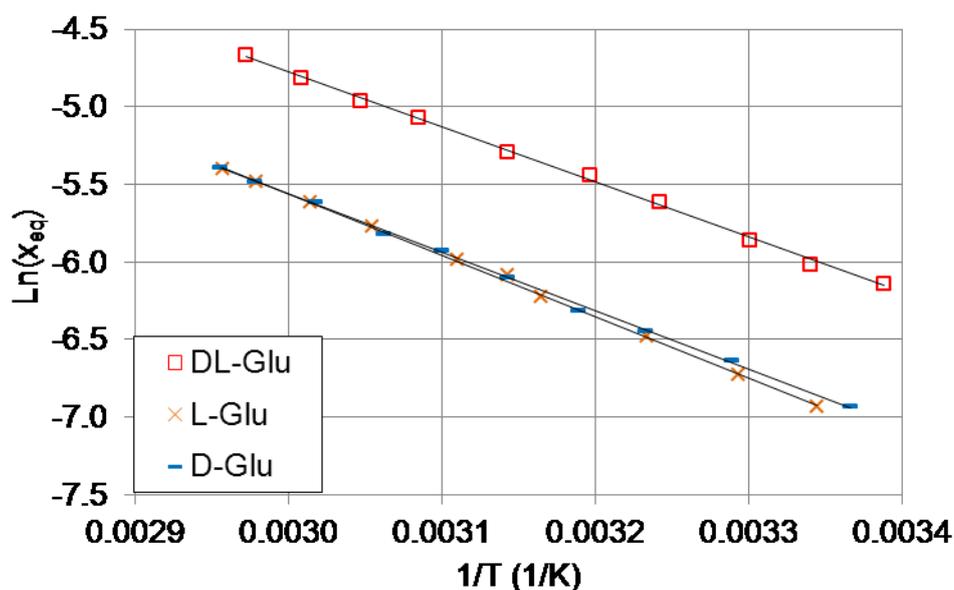


Fig. 4.3 Van't Hoff plot of D-glu, L-glu and DL-glu.

$$\ln(x_{eq}) = A \cdot T^{-1} + B \quad (4.16)$$

Table 4.1 Parameters for the equation 4.16 for the glutamic acid system.

Substance	A = ΔH / R	B = ΔS / R
DL-glu.H ₂ O	- 3546.6	5.8622
D-glu	- 3764.6	5.7296
L-glu	- 3945.8	6.2774

In the table, ΔH / ΔS represent the change of the molar enthalpy / entropy in the solution over a temperature range and R is the gas constant. Based on the parameter A estimated (the slope of the respected trend line), the molar enthalpies of solution can be calculated from the equation 4.18. The estimated molar enthalpies for DL-glu, L-glu and D-glu are shown in table 4.2 and compared with the literature data.

Table 4.2 Calculated molar enthalpies ΔH (kJ/mol) for the glutamic acid system, compared with literature data measurements at 298.15 K.

Substance	this work	Apelblat1997	Dalton1933
DL-glu	29.5*	27.3	23.9 – 25.9*
D-glu	31.3	-	25.4
L-glu	32.8	30.2	25.3

* The molar enthalpies shown are for DL-glu.H₂O

From the table it can be seen that the calculated values are in fair agreement. Still, our results are more close to these, reported by Apelblat et al.

Essential information, needed for the optimal realization of the crystallization, is the estimation of the metastable zone width. In Fig. 4.4 are depicted the results from the polythermal experiments, done with Crystal 16TM.

The MSZW of the single enantiomers is broad with a $\Delta T_{\max} > 20$ K between the solubility and supersolubility curves for saturation concentrations below 55°C. From the measurements it can be concluded that crystallization experiments can be conducted in relatively high supersaturated solutions with a considerable increase in productivity. Hence, for the crystallization experiments of L-glu, saturation concentration at 50°C and a moderate supersaturation of 1.19 ($T_c = 45^\circ\text{C}$) were used and the results are shown in chapter 4.4.

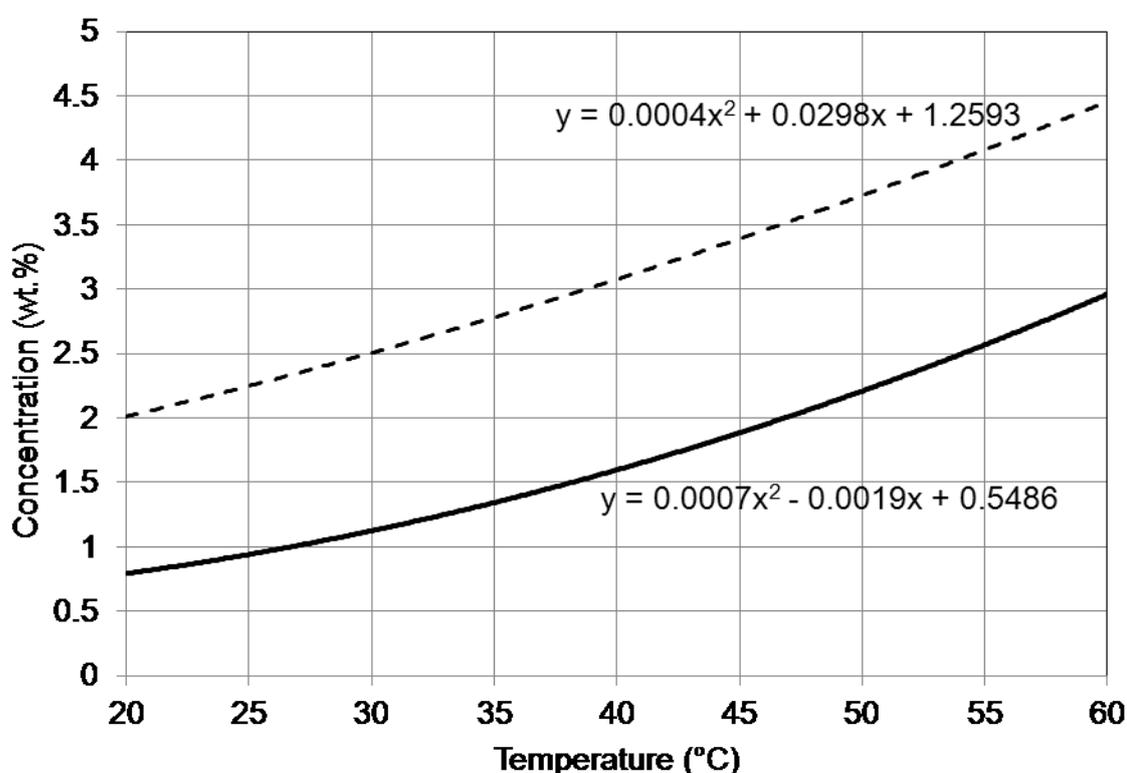


Fig. 4.4 MSZW of L-glu. The solubility / supersolubility curves are depicted with solid / dashed lines respectively correspondent to the appropriate polynomial equation. Experimental data for solubility / supersolubility is given with circles / triangles. The data for D-glu overlaps with L-glu data in the entire temperature region shown and it is not depicted.

The MSZW of DL-glu.H₂O was also measured, but the results are not represented. As DL-glu.H₂O is a racemic compound, it cannot be separated into single enantiomers by preferential crystallization [Yokota2006]. It can also be seen from measured XRPD patterns, (shown in fig. A2.1) there is a considerable

difference between the measured samples of DL-glu.H₂O and the pure enantiomers.

- Solubility equilibria and MSZW of the asparagine monohydrate system

The solubilities of D-asn.H₂O, L-asn.H₂O and DL-asn.H₂O in water were determined gravimetrically in the temperature range 10°C – 60°C. In the figure 4.5 are shown the data from the solubility measurements along with literature values, plotted for comparison.

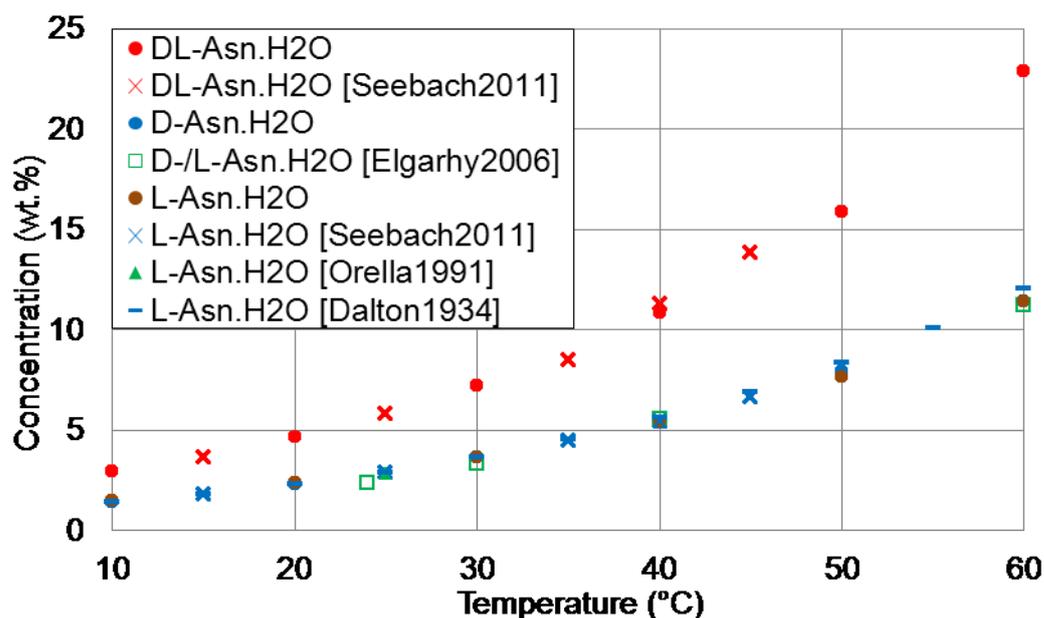


Fig. 4.5 Solubility of the enantiomers and racemic mixtures of asparagine monohydrate as a function of temperature (wt.% - weight percent) (own and literature data).

The solubility courses for both enantiomers D- and L –asn.H₂O are almost identical and the dissolved mass increase exponentially with increasing temperature. From the data it can be concluded that the solubility of both enantiomers in water is equal as expected. The literature values are measured in a range from 15 °C to 45 °C and are in very good agreement with our measurements. Notable deviations from the exponential course can be seen at temperatures above 50 °C. This may be due to the evaporation of the water at high temperatures, thus increasing slightly the measured values. Similar with the glutamic acid system, the solubility of the DL-asn.H₂O exceeds that for the pure enantiomers. The measured values show almost double magnitude as these for

the single enantiomers. The construction of the van't Hoff plot (shown in fig. 4.6) gives almost perfect linearization.

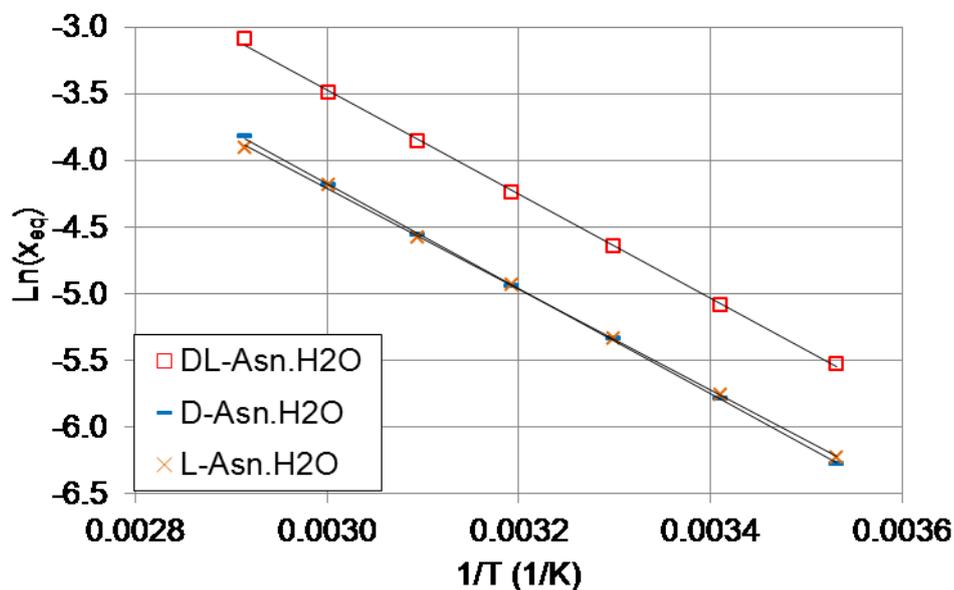


Fig. 4.6 Van't Hoff plot of D-asn.H₂O, L-asn.H₂O and DL-asn.H₂O.

Based on the isothermal solubility measurements of samples, containing defined amounts of D-Asn.H₂O and L-Asn.H₂O in water, the ternary solubility phase diagram of the system D-Asn.H₂O / L-Asn.H₂O / water is constructed with solubility isotherms at 20 and 40 °C, (blue and red lines respectively, see Fig. 4.7).

It can be seen from Fig. 4.7, the ternary system D-Asn.H₂O / L-Asn.H₂O / water exhibits symmetrical behavior with highest solubility at the eutectic. This means that the aqueous solutions of the racemate possess the highest solubility at the eutectic. The initial concentration of the samples for the 20 °C isotherm determination is given in Fig. 4.7 with green dots. It can be seen, that after establishment of equilibria, three of resulted solutions (blue dots) are racemic or very close to racemic, while in the other three the ratio of the L-enantiomer gradually increases while the respective solubility decreases. The same can be observed for the measured at 40 °C samples, where four from the total six starting solutions (black points) resulted after equilibria in the eutectic. However, by the determination of the 50 °C isotherm, the initial concentrations are closer to the measured ones, thus only three samples are measured at the eutectic.

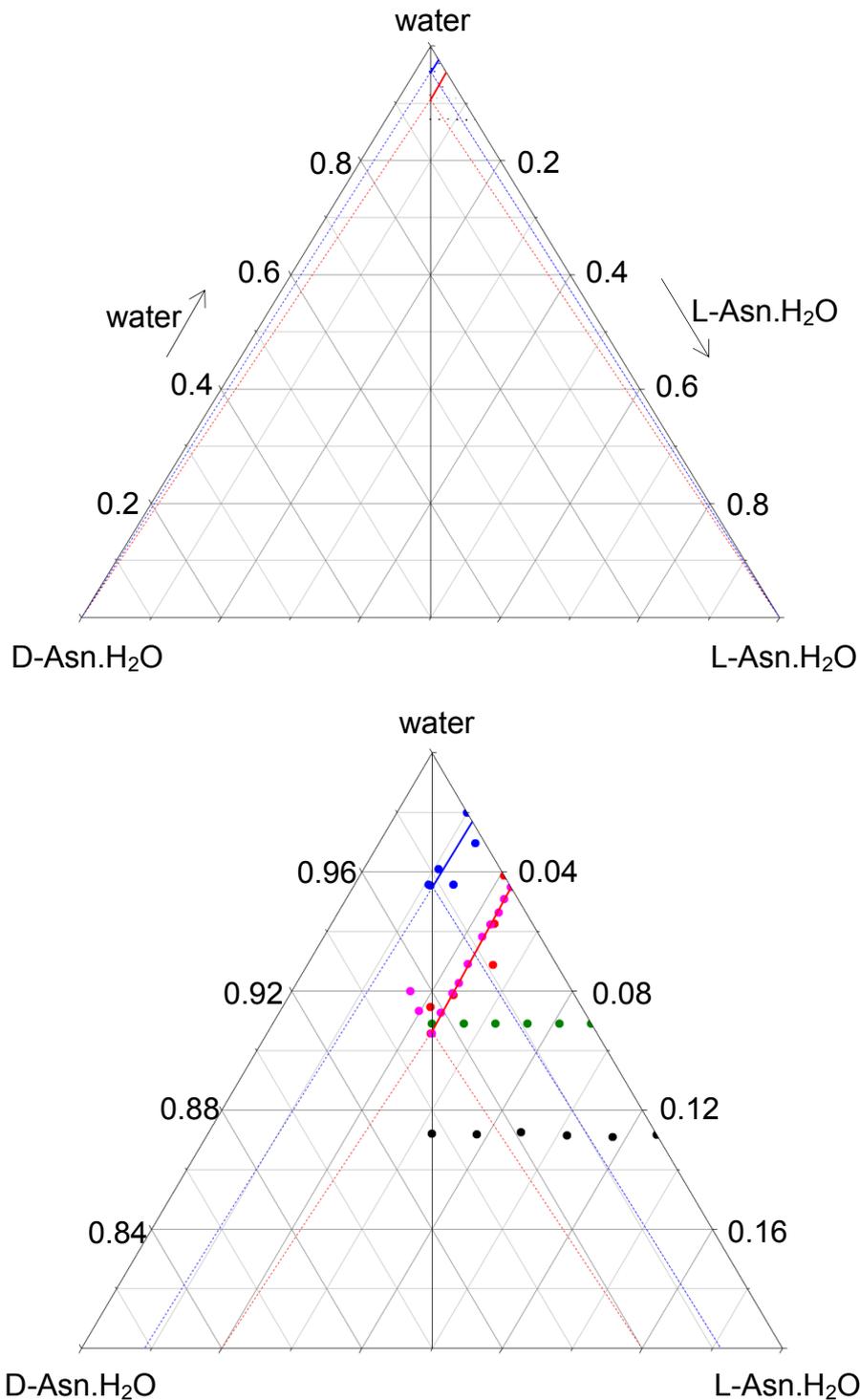


Fig. 4.7 Up: Ternary solubility phase diagram of the system D-Asn.H₂O / L-Asn.H₂O / water; **Down:** Upper 20% section of the diagram, shown for clarity. Isotherms at 20 and 40 °C are shown with blue and red lines respectively. Additionally, the respective colored dashed lines represent tie-lines, separating two-phase from three-phase zone. Green and black dots represent initial concentration at 20 and 40 °C respectively. Literature data is represented with pink dots [Seebach2011]. Axes are in weight fractions.

This behavior in the solubility phase diagram concludes that the ternary system D-Asn.H₂O / L-Asn.H₂O / water exhibit simple eutectic. Moreover, XRPD diffractogram of the samples from the solid phase with racemic ratio, taken at 20 and 40 °C unambiguously show that a mechanical mixture of both substances has been formed. The XRPD diffractogram is given in Fig. A2.2.

In order to optimally perform a preferential crystallization experiment, the metastable zone width of the asparagine racemic solution was studied. The results from the polythermal measurements for determination of the MSZW of DL-asn.H₂O are shown in figure 4.8.

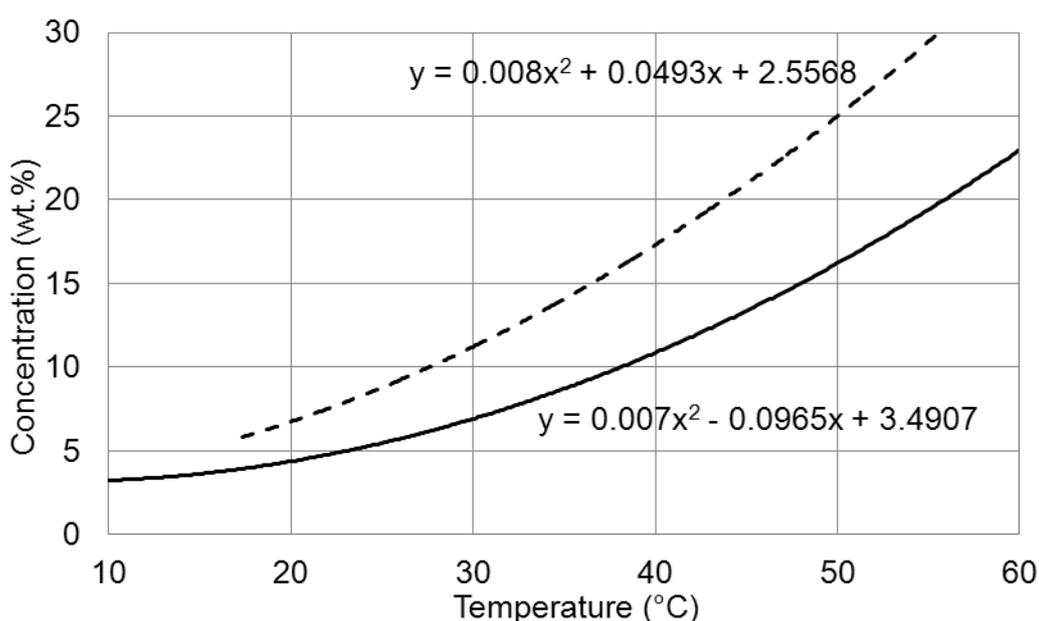


Fig. 4.8 Solubility and MSZW of DL-asn.H₂O. The solubility / supersolubility curves are depicted with solid / dashed lines respectively correspondent to the appropriate polynomial equation. Experimental data for solubility / supersolubility is given with circles / triangles.

The two curves define an expanding metastable region, where ΔT at concentration of 5 wt.% is about 7 K and rises up to 14 K at 23 wt.%. This suggests that subsequent to the crystallization experiments, a relatively high supersaturation levels could be used. Nevertheless, in high supersaturated solutions the possibility of spontaneous nucleation cannot be neglected. For this purpose, a temperature difference of no more than 8 K appears to be suitable for eventual crystallization experiments.

- Solubility equilibria and MSZW of the aminobenzoic acid system

The measurements of the solubility and the metastable zone width (MSZW) of the aminobenzoic acid system were performed for two out of the three possible stereoisomers – ortho-aminobenzoic acid (OABA) and para-aminobenzoic acid (PABA). The polythermal solubility measurements of OABA are done in temperature range 10 – 50 °C (blue dashes in Fig. 4.9). Isothermal solubility measurements of OABA and PABA (in Fig. 4.9 green points and blue crosses respectively) are done at temperatures 20, 35, 40, 45 and 50 °C. The results are shown along with literature data. Solubility of meta-aminobenzoic acid (MABA) is also shown for comparison. It can be clearly seen from the figure, that all three isomers exhibit very low solubility in water, which at 50 °C is between 1.2 and 1.4 wt.%. The pure isomers, having a hydrophobic benzene core, cannot form strong interactions with the water, which explains their low solubility in it. On the contrary, the carboxyl- and amino- groups can form relatively strong hydrogen bonding interactions, thus promoting the solvation of the molecules in the water. This is confirmed by He et al., which has published theoretical and experimental studies of water complexes of OABA and PABA [He2005].

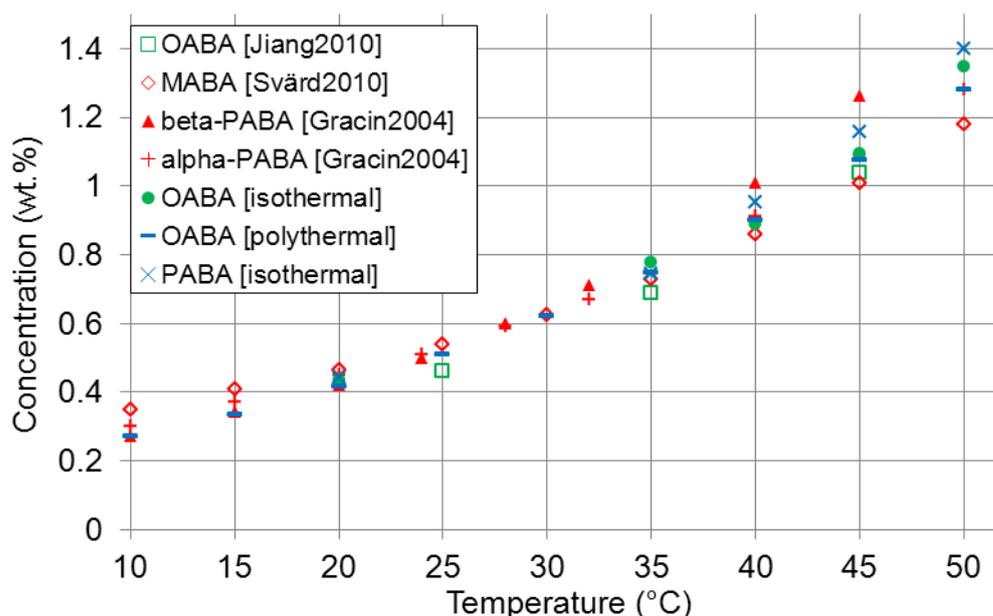


Fig. 4.9 Solubility of OABA, MABA and PABA aqueous solutions as a function of temperature (wt.% - weight percent) (own and literature data).

Hence, the measured solubility values show noticeable differences in temperature range below 15 °C and above 35 °C. It must be noted that all three isomers of aminobenzoic acid exhibit polymorphic transformations. The data for PABA shows that both polymorphs are enantiotropic with a transition temperature of 25 °C. Above this temperature the solubility of the alpha-form becomes lower than the beta-form and it crystallizes preferentially [Gracin2004]. The MABA has two polymorphs, form I is the stable and form II – metastable. The data represented in the figure is for the stable form I. Svärd et al. have investigated both MABA polymorphs and have shown that metastable form II turns very quick to form I in aqueous and methanol solutions [Svärd2010]. Almost similar tendency is published for the OABA polymorphs. Jiang et al. have observed that at lower temperature the solubility differences between all forms in water are relative large, while above 50°C the solubility of form I approaches those of the other two forms. The authors have proven that the transformation temperatures of form III to form I are probably lower than that of form II to form I. The transformation results unambiguously show that below 50 °C forms II and III are transforming to form I [Jiang2010]. It can be concluded that form I is the most stable form, while forms II and III are metastable below 50 °C. In our case, only form I of OABA was crystallized and observed microscopically. For PABA, α -form was observed with no appearance of β -form at higher temperatures (above 35°C) and at temperatures below 25°C only α -form was crystallized and observed. The results from XRPD measurements from the respected crystal samples have unambiguously shown, that a polymorph type I of OABA and α -polymorph of PABA have been formed.

Based on the isothermal solubility measurements of samples, containing defined amounts of OABA and PABA in water, the ternary solubility phase diagram of the system OABA / PABA / water is constructed with solubility isotherms at 25, 35 and 50 °C, (blue, green and red lines respectively, see Fig. 4.10).

It can be clearly seen from Fig. 4.10 the ternary system OABA / PABA / water exhibits also symmetrical behavior like the case of asparagine enantiomers in water. In this case, aqueous solutions of OABA and PABA with 50:50 ratios possess the highest solubility at the eutectic.

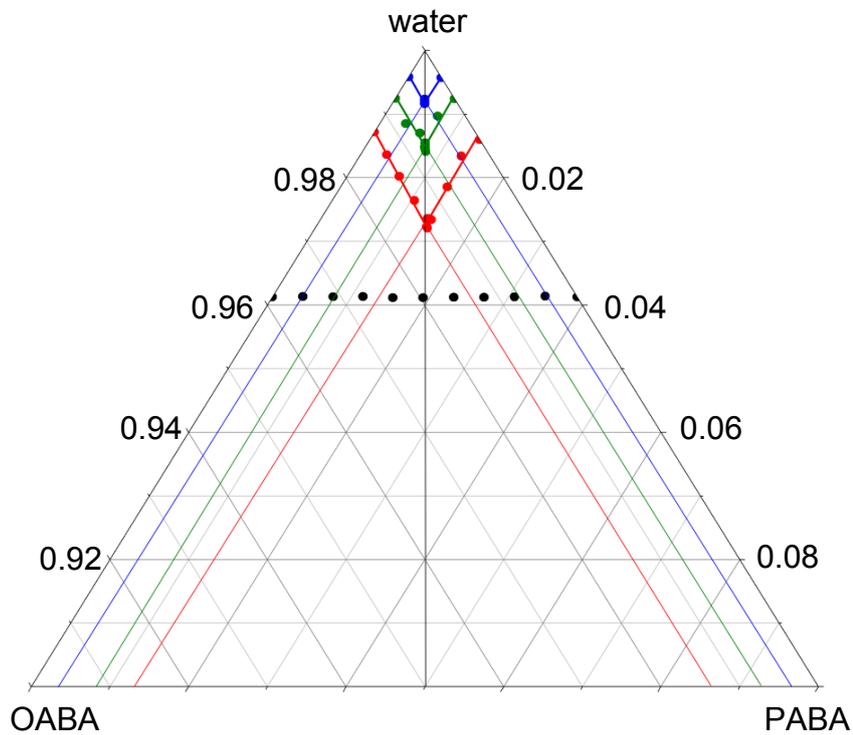
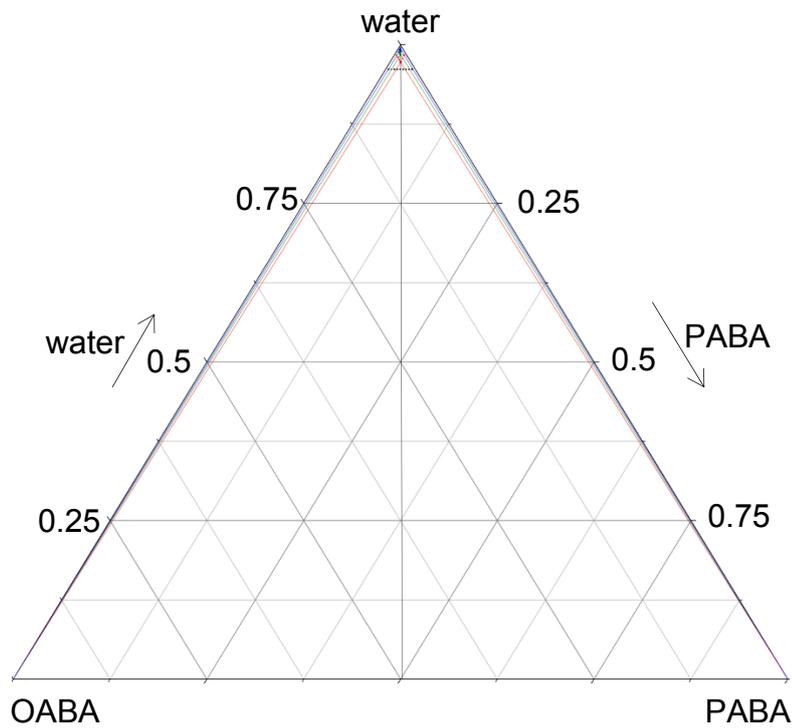


Fig. 4.10 Up: Ternary solubility phase diagram of the system OABA / PABA / water; **Down:** Upper 10% section of the diagram, shown for clarity. Isotherms at 25, 35 and 50 °C are shown with thick blue, green and red lines respectively. Additionally, the respective colored thin lines represent tie-lines, separating two-phase from three-phase zone. Black dots represent initial concentration. Axes are in weight fractions.

The initial concentration of the samples for each isotherm determination was the same and it can be seen, that for the determination of the 20 °C isotherm, all concentration measurements at equilibria are at the eutectic point. Hence, the respective tie-lines delimitate all initial conditions into the three-phase zone of the ternary phase diagram. The same can be observed for the measured at 35 °C samples, where only one point is observed in the respective two-phase region. However, by the determination of the 50 °C isotherm, the initial concentrations are closer to the measured ones, thus only three samples are measured at the eutectic. This behavior in the solubility phase diagram concludes that the ternary system OABA / PABA / water exhibit simple eutectic. Moreover, XRPD diffractogram of the samples from the solid phase with 1:1 ratio, taken at 20 and 50 °C unambiguously show that a mechanical mixture of both substances has been formed and no polymorphic transformation is observed.

The application of the preferential crystallization to separate one isomer in the presence of the other in this case should be possible. Therefore, the metastable zone width of a solution of both substances was studied. The results from the solubility measurements of a 50:50 aqueous solution of OABA and PABA are shown in Fig. 4.11.

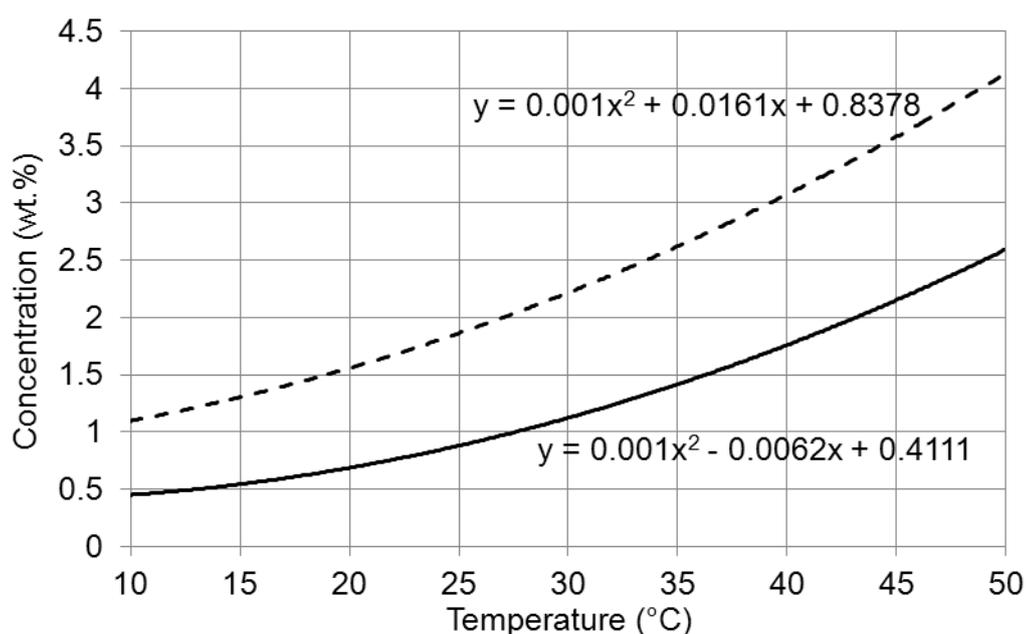


Fig. 4.11 Solubility and MSZW of a 50:50 aqueous solution of OABA and PABA. The solubility / supersolubility curves are depicted with solid / dashed lines respectively correspondent to the appropriate polynomial equation.

A comparison between the measured data for the pure substances (Fig. 4.9) and the values shown in Fig. 4.11, it can be clearly seen, that the solubilities of the aqueous solutions of the both substances are twice as high as these for the single substance. The estimated broad metastable zone width has a ΔT of about 18 K at lower temperatures and a value of 15 K at 50 °C. Hence, by the determination of the supersolubility curve, the calculated standard deviation is 2.24, which corresponds to temperature differences up to 5 °C. This could be due to the very low solubility of the samples, leading to increased discrepancies by the local formation of nuclei.

- *Summary*

In chapter 4.2, results from the solubilities and MSZW of aqueous solutions of the substances used in this thesis were represented and the dependency of the concentration on the temperature discussed. Generally, the solubility increases with the increase of the temperature. The solubility values for the single glutamic acid enantiomers are very close to those for aminobenzoic stereomers at lower temperatures (e.g. 0.3 - 0.4 wt.% at 10°C) and with the increase of the temperature the difference between the values rapidly increase up to 0.7 – 1.0 wt.% at 50°C. In comparison to them, the solubility of the asparagine enantiomers is almost 4 times higher with values from 1.4 wt.% at 10°C up to 7.6 wt.% at 50°C. This could be reasoned with the respected molecule structures (see Figs. 3.1, 3.2 and 3.3), where the benzyl core and the length of the carbon chain are the main reasons for the lower solubility of the aminobenzoic acid and glutamic acid in water respectively. On the contrary, shorter carbon chain of the asparagine along with hydrophilic functional groups (-COOH and -NH₂) increases the molecule affinity to water and therefore the solubility of the substance. For glutamic acid and asparagine monohydrate systems incipient decomposition was suspected at temperatures above 65°C indicated by slight coloring of the solution samples, which resulted in a slight decrement of the measured values for the solid-liquid equilibria. The same trend was also observed in aminobenzoic acid system, starting at about 45°C. Based on the solubility measurements and the respected MSZW, it can be generally concluded that further crystallization experiments could be planned in the temperature region 30°C – 45°C with

supersaturation up to 1.5, where the productivity could be relatively high, while attaining low nucleation probabilities and keeping the solutions stable with time.

4.3 Generation of seeds by ultra-sonication

The results from the US crystal breakage consider the effects of four operating parameters on the particle size - stirring rate, temperature, solution density and sonication power dissipated into the suspension. Furthermore, the sonication power was varied stepwise from 48 to 480 W, while stirring rate, temperature and suspension density were kept constant during the experiments. An exponential increase of the temperature was observed with time when the sonication power was increased above 100 W (or 20% of the maximal power of the US-bath). This had led to an increase of the solution density values and on one side is an indication of dissolution of the crystals and on the other side has strong effect on the crystal size distribution. In order to avoid unwanted dissolution, the sonication power was kept at 10% of the maximal power of the US-bath and in the following, only results from these experiments will be presented and discussed. It should be noted that even at 10% of the maximum power, a slight change of the solution temperature was detected, increasing with about 4.2 K after 1 h continuous sonication. This temperature offset was used further in chapters 4.4 and 4.5.

The de-aggregation / de-agglomeration effects as well as fracturing of the crystals during the ultrasonic treatment of samples of L-glu, L-asn.H₂O and OABA are presented in Figure 4.12 as calculated mean crystal size versus residence time, where two experimental setups were used and compared. The estimation of the mean crystal size, d_{50} , from the q_3 distribution of the measured CSD is explained later in chapter 4.4.1.4. The setup description and the experimental procedures can be found in subsection 3.3.1.2 of chapter III. The residence time represents the exposure time of the sample to the ultrasonic radiation.

It can be seen that with time, the mean particle size of all samples is decreasing. The biggest reduction of d_{50} is observed during the first 5 minutes and after that just a small changes in particle sizes is recorded for the batch experiments. On the contrary, the continuous experiments show constant almost linear reduction of the mean crystal sizes. The difference between the results may be due to the construction of the experimental setups used. In the continuous setup, the

suspension was constantly pumped by a peristaltic pump, which can lead to continuous attrition of the crystals in the pump head.

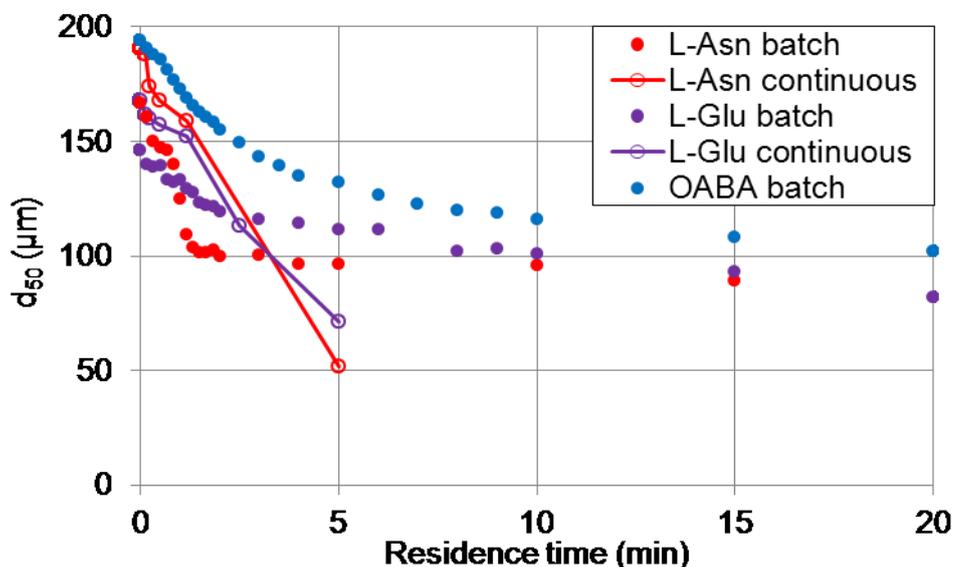


Fig. 4.12 Ultrasonic breakage of crystals of L-asn, L-glu and OABA in time. Experiments, done in batch setup are shown with filled circles, while experiments, done in continuous set-up are presented in open circles and a line.

The substances can be arranged according to their breakage. It can be seen from the figure that crystals from L-asn.H₂O break up very quickly from a mean size of 167 µm in about a minute to a mean size of 100 µm and then just a slight change in the crystal size is observed (after 20 min of US, d_{50} = 81 µm). On the contrary, the crystals from OABA need longer period to break up and their mean size change at the whole time interval from a value of 194 µm at the beginning of the process up to a value of 102 µm after 20 min. The crystal mean size values from L-glu are located between those from L-asn.H₂O and OABA. Hence, L-glu crystals break up fairly quickly in the first 3 minutes from a mean value of 146 µm to sizes about 115 µm and then show almost the same course as the crystals from OABA, reaching a value of 82 µm after 20 min of sonication.

Before and after each experiment, microscopic photographs of the samples are taken and the corresponding crystal sizes were measured. In the figure 4.13 are shown microscopic photographs of the crystals used before the start of the experiment and after 20 min of constant US comminution.

A comparison of the size values from microscopic photographs with the mean crystal sizes from the FBRM measurements shows that both data are in good

agreement. The crystals from all substances exhibit good distinguishable faces, shapes and sharp angles. After the US break up, it can be noticed that the crystal forms are not so clear to distinguish. L-asn.H₂O crystals have become more spherical with rounded edges, while for OABA crystals a great number of crystal fragments can be seen. The usually needlelike crystals of β -L-glu have been broken up to small fragments, but with distinguished edges. Some of them have multiple cracks on their surface due to the US comminution and this effect could be caused by the cavitation.

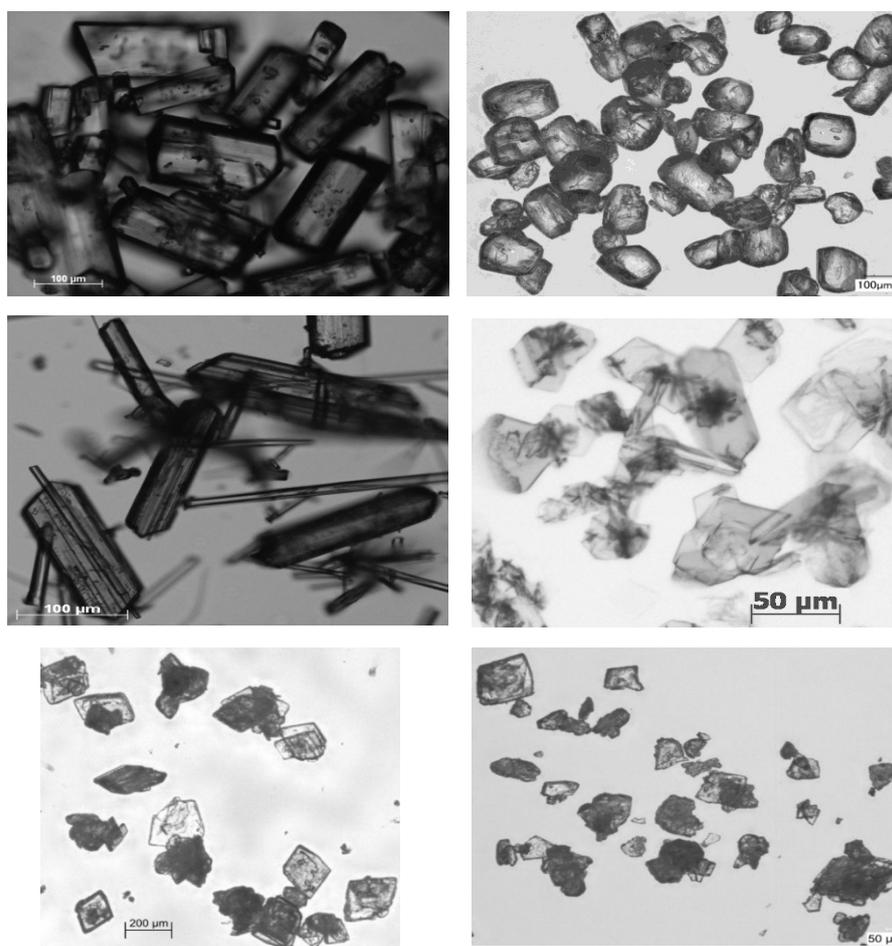


Fig. 4.13 Microscopic photographs of crystals from L-asn, L-glu and OABA (top to bottom). On the left are shown crystal before US comminution, on the right are shown crystals after 20 min of US comminution with 10% of the maximal power.

It can be summarized, that bigger crystals and agglomerates can be successfully comminuted into smaller crystal fragments under the influence of the ultrasound, applying only 10% of the maximum power and a provided residence time of 5 min. Moreover, the constant attrition from the pump head helps additionally the

process and lowering the residence times of the crystals in the US-bath. The thus created seeds can be used for the continuous operation of the crystallization process.

4.4 Experiments in a single fluidized bed

4.4.1 Influence of selected parameters on the crystal size distribution

A novel fluidized bed crystallizer (FBC) was constructed and put into operation for the next experiments. Its description and the corresponding experimental procedures can be found in chapter 3.3.2. In the current chapter, the influence of the flow rate, generation of seeds through US comminution, and the use of different seed sizes on the generated product CSDs during the fluidized bed crystallization process will be described. On one side, different flow rates of the solution flowing through the crystallizer were applied and in detail discussed. The rates used were 6, 9 and 12 l/h. In addition, the influence of the continuous seeding, provided through ultrasonic comminution in conjunction with the crystallization process will be also demonstrated. In the previous subsection it was shown that implementation of US crystal breakage on the production of seed crystals was successful. The potential of the US bath of generating seeds of 50-80 μm size was used in the current experiments at 10 % of the maximum power (48 W) and its influence was studied on the CSD along the crystallizer height, x . The influence of different seed crystal sizes on the product CSDs produced by other procedures was also studied. A summary of the conditions, used to perform the experiments, can be seen in Table 4.3.

Table 4.3 Experimental conditions used for the fluidized bed crystallization of L-glu.

Experimental conditions	Values
saturation temperature, [$^{\circ}\text{C}$]	50
crystallization temperature, [$^{\circ}\text{C}$]	45
initial solution concentration, [wt.%]	2.2
supersaturation, [-]	1.2
seed amount, [g]	1.75
seed sizes, [μm]	40 \div 80
feed flow rates, [l/h]	6, 9, 12
ultrasonic attenuation, [kHz]	35
ultrasonic output power, [W]	48
seed generation flow rate, [l/h]	2

It can be seen from the table, the generated supersaturation of 1.2 is relatively low, although the measured width of the metastable zone of L-glu is about 25 °C (see section 4.2). Hence, the main goals of the experiments are, as already mentioned above, to study the influence of selected parameters, while maintaining slight supersaturation levels and avoiding possible nucleation. The seed amount value used was calculated from eq. 2.19.

4.4.1.1 Influence of the feed flow rate

In Fig. 4.14 are shown CSDs of L-glu crystals, obtained at the different outlets of the crystallizer. Figures 4.14a, 4.14b and 4.14c refer to flow rates of 6, 9 and 12 l/h respectively. These experiments were performed without generation of seed crystals using the ultrasound. For the experiment conducted with flow rate of 6 l/h, the mean crystal size (d_{50}) of ~200 μm can be observed at output I and ~50 μm is measured at output VI. The mean crystal sizes for experiments conducted with flow rate 9 l/h have values of ~180 μm at outlet I and ~100 μm at outlet IV and for the flow rate 12 l/h d_{50} is ~220 μm at outlet I and ~150 μm at outlet IV. The data show that with increasing flow rate of the L-glu solution in the crystallizer from 6 to 12 l/h, the mean crystal sizes at the different outlets rise and the CSD gets narrower. This is expected as the drag force of the current flow grows with the increase of the flow rate, compared to the almost constant particle weight. The difference in crystal sizes at different outlets is significant when using a flow rate of 6 l/h and gets smaller with increasing flow rate. At 9 and 12 l/h (Fig. 4.14b and 4.14c) no CSDs could be measured from samples taken at the outlets above the fourth one, because of the lack of the crystal suspension. Almost no agglomeration was observed during the experiments, although at a flow rate of 12 l/h after 6 h incipient agglomeration was detected. At the beginning small agglomerates were seen freely floating, but after an hour they grow so big and heavy, that they severely restrained the upward fluid flow and thus collapsing the crystal bed. The formation of crystals, which looked like long needlelike plates, could be a possible reason for the formation of agglomerates, see Fig. 4.15. As this experiment was repeated 3 times and the agglomeration occurred at every experiment at almost the same time, it can be concluded that at higher flow rates

Ch. 4 Results and discussion

even severe agglomeration could occur and as a result the whole process could be obstructed.

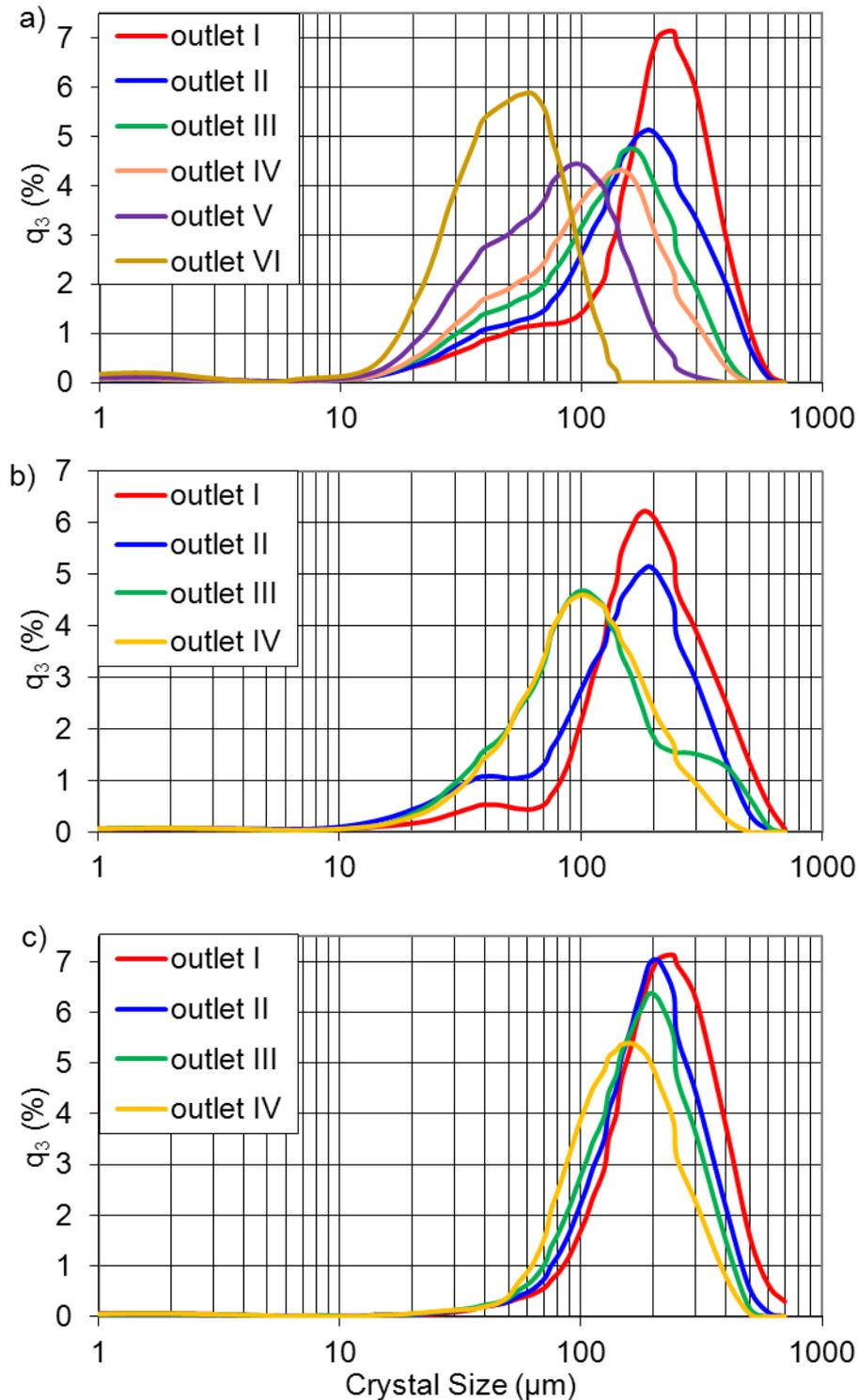


Fig. 4.14 CSDs, represented by the steady state q_3 distribution, of L-glu obtained at different outlets along the crystallizer height without influence of the US bath at flow rates of 6 (a), 9 (b) and 12 l/h (c). The initial seeds used in the experiments were sieved using a 45-68 mesh [Binev2011a].

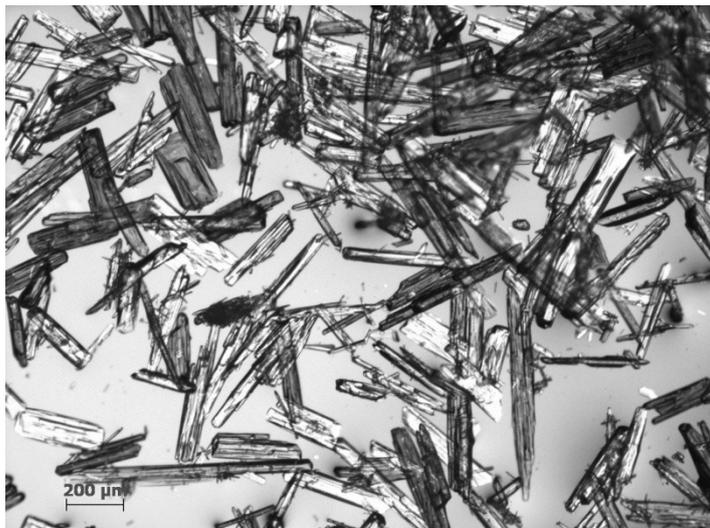


Fig. 4.15 Microscopic image of product crystals of L-glu, taken from outlet I after the agglomeration took place in the crystallizer.

4.4.1.2 Influence of the ultrasound seed generation

In chapter 4.3 was already studied the generation of seed crystals by applying power ultrasound on a suspension of bigger crystals and crystal agglomerates. In this chapter, the indirect influence of the seed generation loop on the CSD along the height of the crystallizer will be studied. In order to be consistent, the experimental conditions were kept the same as mentioned in the previous chapter. Additionally, seed crystals were continuously introduced into the bottom of the crystallizer from the seed generation loop, while at the same time bigger crystals and crystal agglomerates were taken from the bottom of the crystallizer. The achieved product CSDs of the L-glu crystals are presented in Fig. 4.16. The bimodal CSD with maxima at $\sim 100 \mu\text{m}$ and $\sim 200 \mu\text{m}$ is to be seen in fig. 4.16a and b. This can be due to the influence of the US attenuation, based on the continuous breakage of the bigger crystals and therefore the continuous production of smaller ones (with sizes around $100 \mu\text{m}$) and their insertion in the crystallizer. While this process happens at the bottom of the crystallizer, the seeds float up through the fluidized bed, dragged by the fluid flow. Thus, when taking out samples at the outlets some of the fresh generated seeds are also withdrawn.

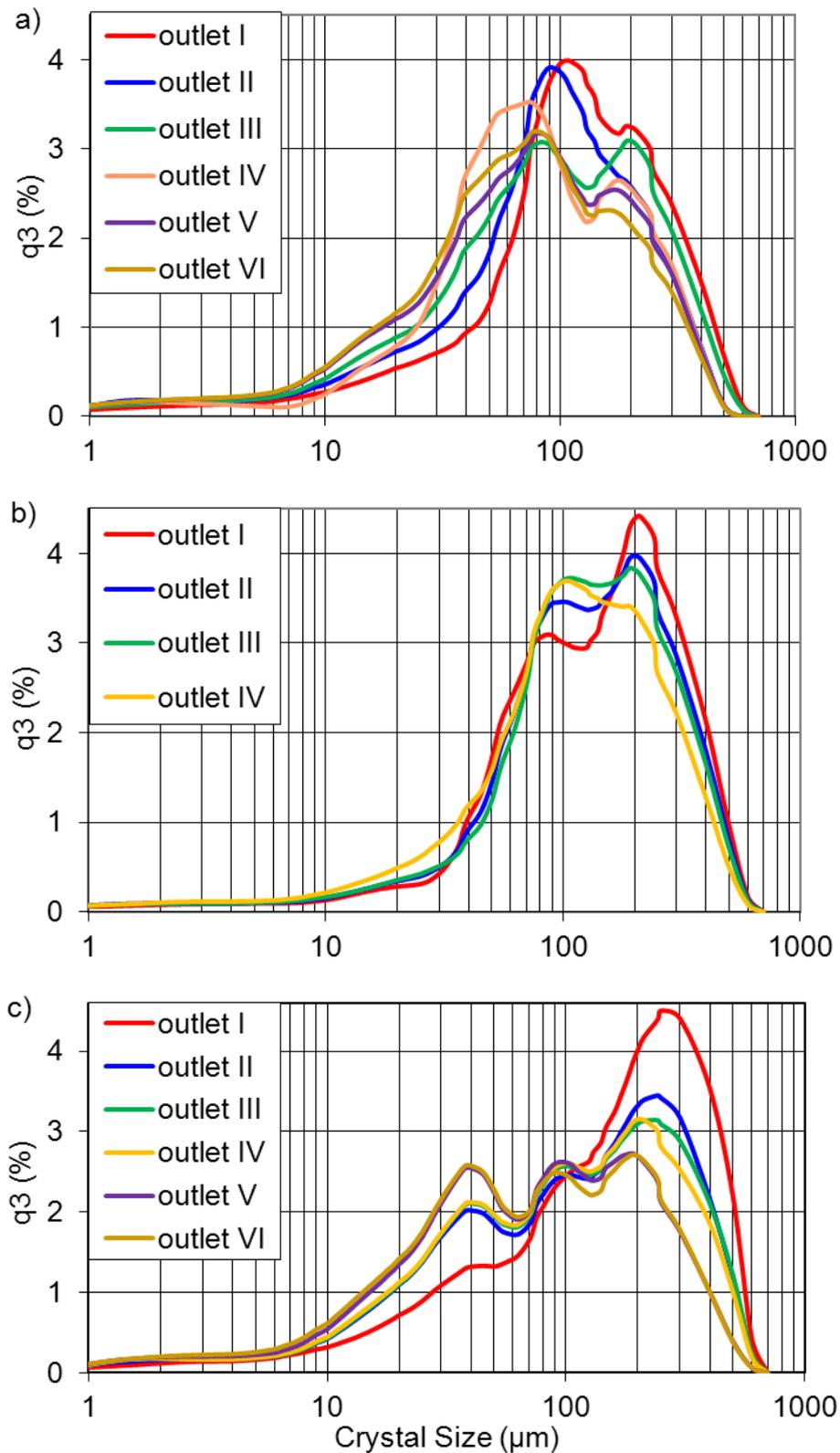


Fig. 4.16 CSDs, represented by the steady state q_3 distribution, of L-glu obtained at different outlets along the crystallizer height under the influence of continuous US seed generation at flow rates of 6 (a), 9 (b) and 12 l/h (c). The initial seeds used in the experiments were sieved using a 45-68 mesh [Binev2011a].

As already mentioned in the previous chapter, in all experiments with a flow rate of 12 l/h, incipient agglomeration was observed 6 h after the start of the process. Nevertheless, samples could be taken out at this point and the CSDs are depicted in Fig. 4.16c. The additional maximum around 40 μm from the trimodal CSD may be due to small crystals from US comminution and captured within the agglomerates or crystal fragments from the agglomerate break up in the measuring device (CILAS 1180L).

In general, the CSD curves between the different outlets in each experiment look very similar. Nevertheless at the lowest flow rate the content of the smaller particles ($\sim 100\mu\text{m}$) exceeds the content of bigger ones ($\sim 200\mu\text{m}$). Increasing the flow rate leads to an increase of the content of the bigger crystals and a reduction of the content of smaller ones. This behavior can be attributed to the different ratios between the increasing feed rates from 6 to 12 l/h and the constant flow rate ($\sim 2\text{ l/h}$) of the seed generation circle.

For a continuous operating mode and respectively continuously taking out crystals with desired specific size from one of the outlets, the continuous seed introduction by US crystal breakage is required to keep the crystallization process running.

4.4.1.3 Influence of the various seed sizes

Experiments with three types of seed crystals were conducted with the same conditions as already used (see table 4.3). For the experiments 1 and 2, the crystals seen in Fig. 4.17a and 4.17b were produced by dry milling of β -polymorph crystals of L-glu in a mortar. Additionally, the crystals seen in Fig. 4.17b were sieved using a 38-68 μm sieve. For experiment 3, the crystals seen in Fig. 4.17c were produced from already grown β -polymorph crystals of L-glu in the FBC, followed by sonication for 1 h in the US bath. Additional samples were collected in order to investigate the mean size of the solid particles, flown back to the feed tank from the top of the FBC. Hence, the mass of the lost solid phase after solid-liquid separation was determined to be about 1.25 g/h and the mean size of the crystals was about 45-50 μm , measured with light microscopy.

In Fig. 4.17d are shown product crystals from experiment 3, achieved with seed crystals, generated in the US bath. The measured with laser diffraction CSDs of

the seeds and the product crystals, taken from outlet III of the FBC from all three experiments are shown in Fig. 4.18.

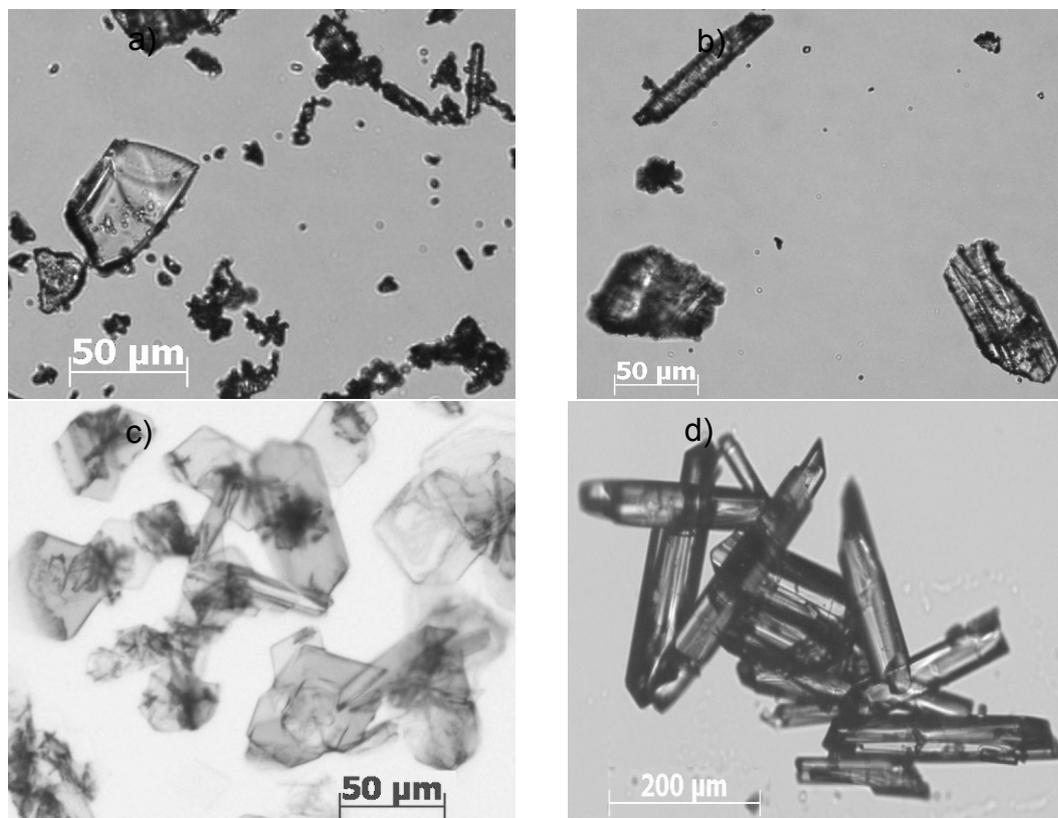


Fig. 4.17 Microscopic images of crystals of L-glu: a) seed crystals produced by milling; b) sieved seed crystals, after milling; c) seed crystals produced by US comminution; d) achieved product crystals.

It can be noticed, that the values of the mean crystal sizes (d_{50}) of the different seeds are close to each other, but the widths of the respective density distributions are totally different, as it can also be seen from Fig. 4.18. The widest CSD is provided for seed crystals produced by milling without sieving. The crystals vary a lot in their sizes and forms (Fig. 4.17a). In Fig. 4.18b is shown, that the same seed crystals, but used after sieving, have tighter but bimodal CSD. The shoulder or the small fraction at around 15 µm can be assigned to crystal fragments, formed by breakage in the sieve apparatus. From Fig. 4.17b is clearly seen the difference in the shapes of the seed crystals, which also contributes to the CSD width. The CSD of the seed crystals, produced by means of ultrasonic attenuation is narrow, monomodal and the crystals are uniform in size, as it can be seen in Figs. 4.17c and 4.18c.

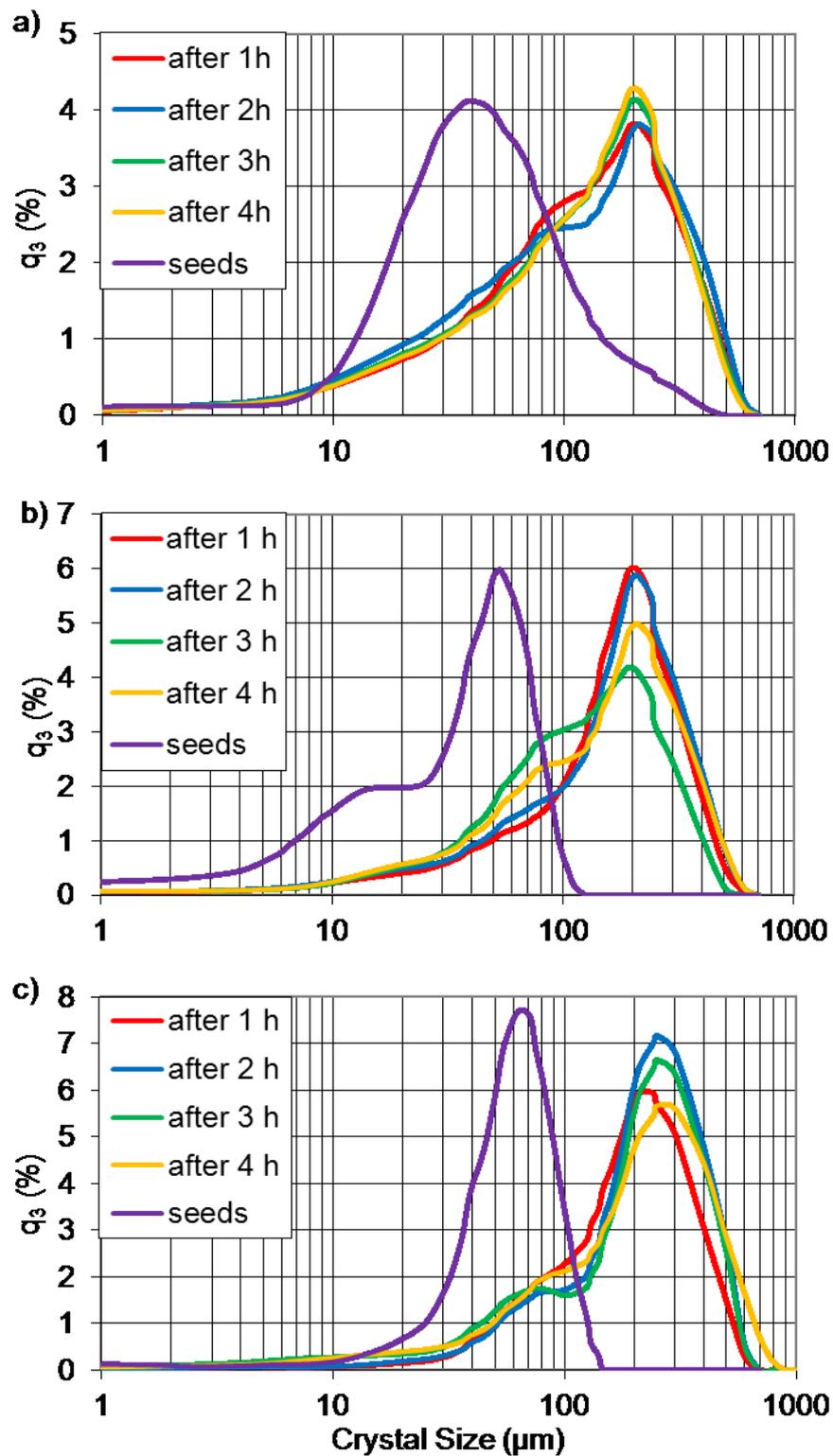


Fig. 4.18 CSDs, represented as the q_3 distribution, of L-glu obtained at a flow rate of 9 l/h from outlet III of the crystallizer, using different types of seed crystals: a) from seed crystals produced by milling; b) from sieved seed crystals, after milling; c) from seed crystals produced by US comminution [Binev2011b].

From Fig. 4.18a it can be seen, that the product CSDs from experiment No.1, compared to those in Figs. 4.18b and 4.18c, are definitely wider. This can be related to the wider CSD of the seed crystals used. Moreover the mean values for characteristic crystal sizes are lower than the respective ones from the experiments 2 and 3. However, the obtained CSDs are similar over the whole crystallization time. The product CSDs in Fig. 4.18b and 4.18c show a shoulder at about 80 μm , i.e. bimodal distributions. It can be related to the continuous production of seed crystals in the US bath. Thus with time, a breakage of the bigger crystals (product) occurs. The calculated mean seed size d_{50} from respected CSDs, shown in Figs. 4.18b and 4.18c is $\sim 45 \mu\text{m}$ used in experiment No. 2 and $\sim 65 \mu\text{m}$ used in experiment No. 3. While the conditions are the same for the both experiments it can be concluded, that the difference between the measured CSDs are probably due to the different seed crystals used respectively. Nevertheless, from all experiments, only the stable β -polymorphic crystals of L-glu were obtained (Fig. 4.17d).

4.4.1.4 Comparison with the Richardson-Zaki force balance model

The applicability of the Richardson-Zaki correlation (equation 2.28) with respect to the steady state was verified on the example of three substances, L-glu, L-asn and OABA by measurements of their local crystal sizes. Hence, the void fraction, ϵ , used in the equation 2.28 was kept constant for all flow rates, and it was experimentally determined for each substance. A defined volume of the crystal suspension was taken out in a measuring cylinder from outlet III of the crystallizer, and then the suspension was filtered in a suction flask with sintered glass filter. The ratio of the liquid filtrate volume to the whole suspension volume equals the void fraction, ϵ , for the specified flow rate. The mean values from three measurements were calculated to be $\epsilon=0.7$ for L-glu, $\epsilon=0.66$ for L-asn, and $\epsilon=0.78$ for OABA, all measured at a flow rate 9 l/h in a saturated at 25°C solution. These values were used in the empirical model (equations 2.31 – 2.32) to predict the corrected with the sphericity factor (eq. 2.36) mean crystal size, d_{50} , while assuming the process is in steady state (eq. 2.33). In order to compare the predicted values with the experimental CSD, a mean value of the crystal size, \bar{L} ,

can be calculated as the first moment of the distribution of the sizes, L , from the q_3 distributions of the measured CSDs (Figures 4.14, 4.16, and 4.18).

$$\bar{L} = \frac{\int_0^\infty q_3(L)LdL}{\int_0^\infty q_3(L)dL} \approx \frac{\sum_{i=1}^{1000} q_3(L_i)L_i(L_i - L_{i-1})}{\sum_{i=1}^{1000} q_3(L_i)(L_i - L_{i-1})} \quad (4.17)$$

The mean value, \bar{L} , will be used further as the mean crystal size, d_{50} , of the respected CSD.

The results from the fluidized bed crystallization of L-glu are summarized in Fig. 4.19, where the CSDs are represented by the experimental d_{50} as a function of the crystallizer height. Additionally to the experimental data, the predicted values for d_{50} are implemented by straight lines. A correction with the estimated sphericity parameter was also implemented on the calculated values shown. The presented in the figure error bars include both effects of the types of the seeds and the ultrasonic attenuation by the estimation of the mean experimental d_{50} . A single experimental d_{50} value is the size in microns that splits the distribution into two areas, where half of the crystal population resides above the value and half resides below it.

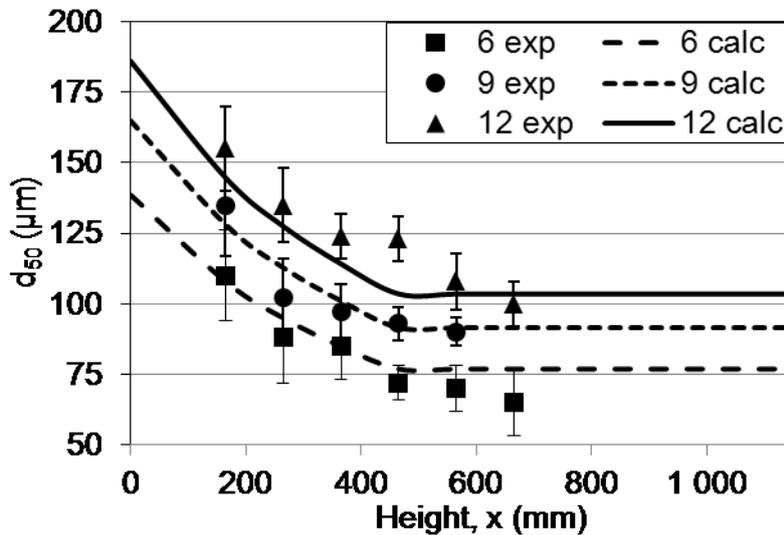


Fig. 4.19 Experimental (eq. 4.18) and calculated (eqs. 2.31 – 2.33 and 2.36) values for d_{50} of L-glu along the height of the fluidized bed crystallizer at flow rates 6, 9 and 12 l/h. Standard deviation error bars include both effects of the types of the seeds and the ultrasonic attenuation on the experimental d_{50} . The calculated values for d_{50} are shown as lines; experimental values – with symbols.

Ch. 4 | Results and discussion

It can be seen from the figure that experimental d_{50} values decrease from outlet I (d_{50} between 110 and 155 μm) until outlet IV (d_{50} between 72 and 124 μm), while keeping almost constant afterwards. This was expected as the fluidized bed crystallizer is conical at the lower part, thus the fluid flow velocity decreases with increasing diameter. This trend is also verified with the predicted d_{50} values, where the terminal velocity depends on the crystallizer diameter and affects the fluid drag force. Good agreement was obtained for flow rates 6 and 9 l/h, while at flow rate of 12 l/h, vast agglomeration occurred, leading to disruption of the fluidized bed structure inside the crystallizer, thus hindering reliable measurements. A comparison with microscopic images showed that at all flow rates needle-like crystals of the β -polymorph of L-glu are formed, see Fig. 4.20 left. It is noted that smaller values for d_{50} were obtained from the measured CSD with laser diffraction in comparison with direct measurements of the crystal sizes from the microscopic images, shown in Figure 4.20. Still, the expected deviation between the methods is due to the needle-like shape of the crystals of L-glu. Moreover, the brittleness of the latter could lead to premature crystal breakage due to the suspension transport through the laser diffractometer from the internal peristaltic pump.

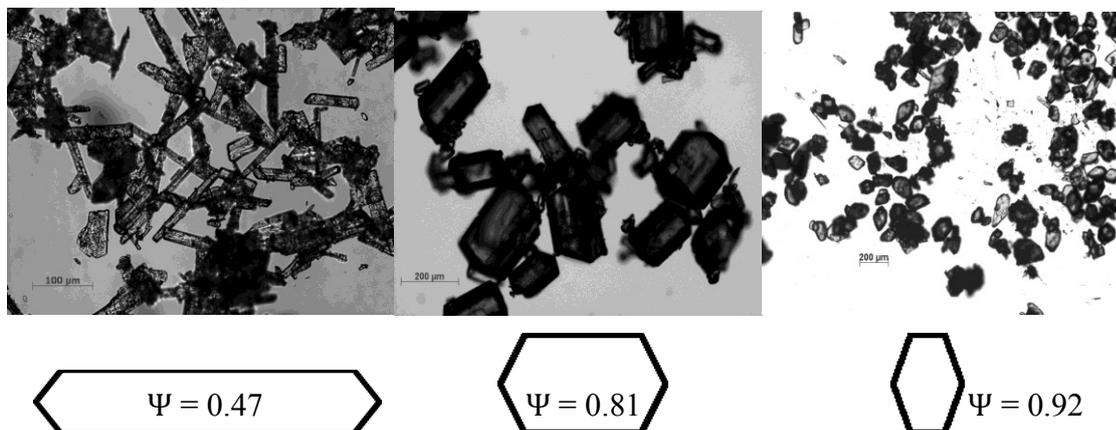


Fig. 4.20 Microscopic images of crystals of L-glu, L-asn and OABA from left to the right, taken from outlet III of the crystallizer at flow rate of 9 l/h. The corresponding calculated sphericity parameters from the crystal shapes are schematically given below.

For the determination of the sphericity parameter, Ψ , of L-glu, the third dimension of the crystal was just guessed due to the impossibility of exact measurement.

Hence, it was possible to derive the crystal dimensions, needed for the calculation of the crystal volume for all substances used.

Another validation of the simplified model was done by comparing predictions of the mean crystal sizes with the experimental data for L-asn and OABA. Hence, series of experiments were conducted, where the segregation of the crystals of L-asn and OABA according to their size was studied at outlet III of the fluidized bed crystallizer in conjunction with different solution flow rates and continuous US comminution. In Table 4.4 are given selected parameters, used for conducting the experiments and in the model for calculation of d_{50} .

Table 4.4 Selected parameters, used in the experiments & modeling.

Experimental conditions	L-asn	OABA
saturation temperature, [°C]	35	35
amount of crystals used, [g]	20	20
crystal sizes, [μm]	40 ÷ 400	40 ÷ 400
feed flow rates, [l/h]	6 ÷ 15	6 ÷ 15
ultrasonic attenuation, [kHz]	35	35
ultrasonic output power, [W]	48	48
seed generation flow rate, [l/h]	18	18
crystal density, [kg/m^3]	1568 ^a	1409 ^b

^a – data from [Lindenberg2011], ^b – data from [Brown1985]

Before the start of the experiments, a defined amount of crystals was taken from the substance storage container and additionally sieved to get a distribution between 40 and 400 μm . The experiments were initiated by the dry insertion of the resulting fraction into the top of the crystallizer, while the flow rate is shortly lowered to 1 l/h to avoid losses from crystals flown out of the crystallizer. After all crystals have settled on the bottom of the crystallizer, the flow rate was set to the desired lowest value and the US bath was turned on.

For the observation of the steady state of the fluidized bed at a constant flow rate, a FBRM probe was used for inline monitoring of the CSD through the crystallizer outlet III by keeping the flow rate constant for 15-20 min. The measured chord lengths from all experiments were additionally compared with offline light microscope image analyses. In Fig. 4.21 and 4.22 are shown the results from the conducted experiments, where the number of particle counted for the different fractions as a function of the flow rate for L-asn and OABA respectively.

Ch. 4 | Results and discussion

The in-line FBRM monitoring started after addition of the crystals from the top of the crystallizer and their complete settling on the bottom. Shortly afterwards, the flow rate was increased to 6 l/h and after 5 min the crystals in the fluidized bed were in the range of the FBRM probe. The flow rate was kept at 6 l/h for 30 min (20 min for OABA) in order to stabilize the rising fluidized bed and to establish a steady state regime.

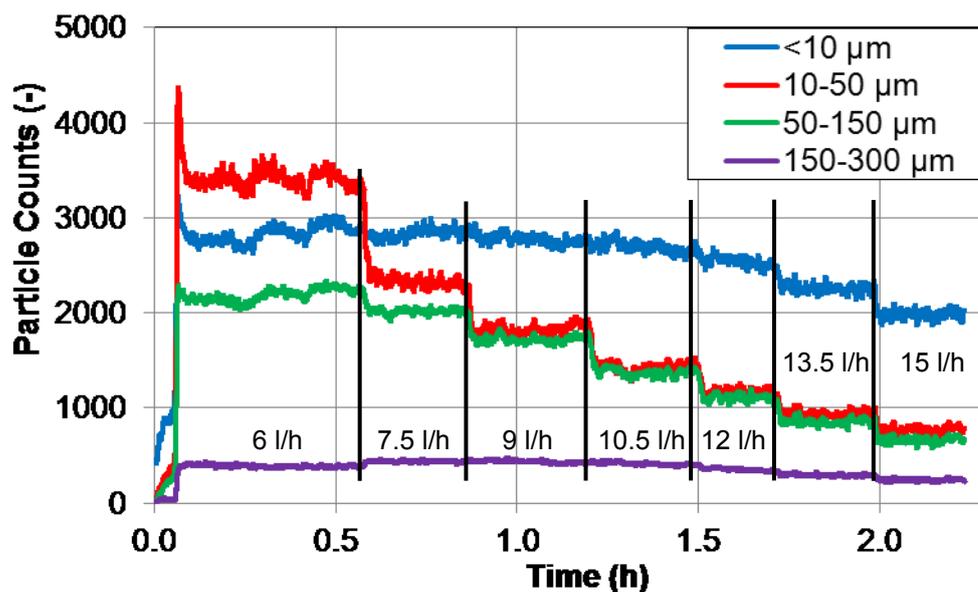


Fig. 4.21 In-line FBRM measurements of the particle counts for L-asn, represented in four size fractions, done at outlet III with flow rates 6 – 15 l/h.

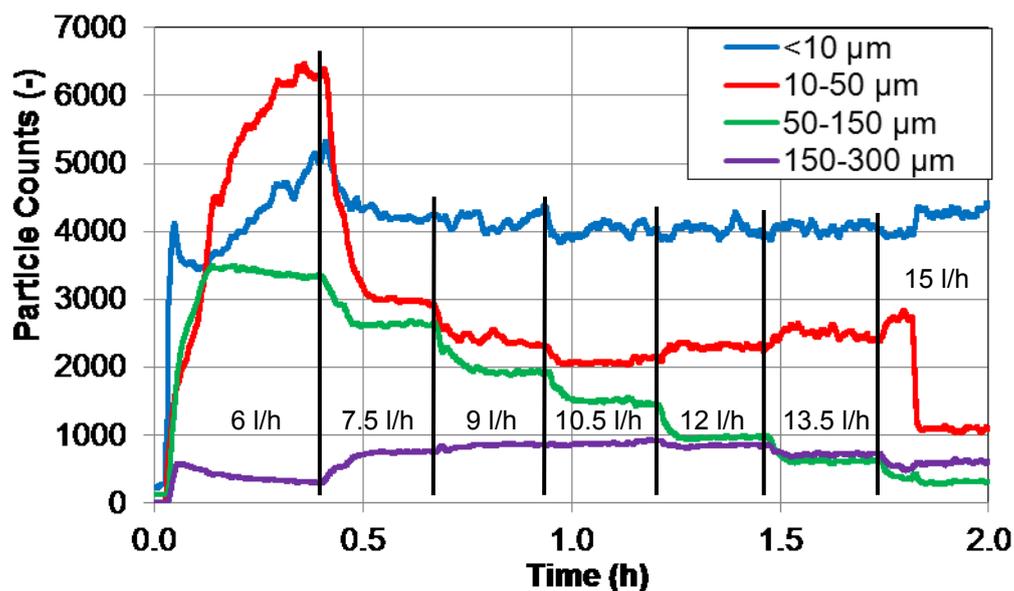


Fig. 4.22 In-line FBRM measurements of the particle counts of OABA, represented in four size fractions, done at outlet III with flow rates 6 – 15 l/h.

With the step-wise increase of the solution flow rate, followed by a 15 to 20 min steady flow, a quick establishment of a steady state regime was observed after the adjustment of the next flow rate. Hence, a decrease in particle counts was observed with the increase of the flow rate, while the particle trends for all size ranges remained constant, when the flow rate was fixed at a specific value. In the case of OABA, vast agglomeration was observed an hour after the start of the experiment. This could be traced in Fig. 4.22 by the trend of the particle size group 10-50 μm , compared to the same size group from the L-asn experiment. It can be clearly seen the deviation of this size group from the general trend of the other particle size fractions. It can be further seen from Figure 4.21, the whole crystal bed was unstable during the beginning of the measurements with drops and rises of the particle size range counts in the case of L-asn. In both experiments, the relatively constant trend of the particle size fraction $<10 \mu\text{m}$ could be due to the small crystal fragments formed during the continuous ultrasonic comminution.

The steady state data obtained from Fig. 4.21 and Fig. 4.22 were used to generate population density distributions for L-asn and OABA, from which median crystal sizes (d_{50}) for the given flow rates were estimated for the given flow rates by applying equation 4.18. The summarized results for the L-asn and OABA are given in Fig. 4.23, where the experimentally evaluated mean sizes (triangles) are compared with the predictions of the mathematical model.

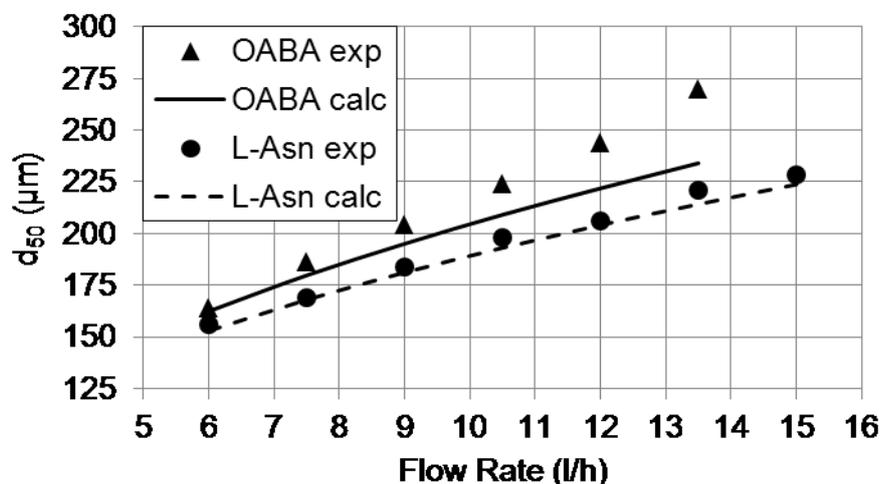


Fig. 4.23 Experimental (symbols) and calculated (lines) values for d_{50} of OABA and L-asn.

It can be seen from the figure, that with increasing flow rate, the drag force F_d (eq. 2.32) exceeds the value of the particle effective weight force W_e (eq. 2.31). Thus, the particles are 'dragged' with the flow until both forces have same values and the Richardson-Zaki relation (eq. 2.28) is fulfilled. At steady state conditions (both forces are equal), particles with a specific volume (size) will occupy the crystallizer volume at the point of the measurement. With further increase of the flow rate, particles with bigger volume will be dragged in, thus increasing the measured mean crystal sizes. As the substances have close values of particle densities (see Table 4.4), it was expected that they show similar trend concerning their CSDs. On the contrary, at same flow rate, a difference was observed between the d_{50} values of L-asn and OABA. The OABA crystals, being less dense than those of L-asn, need a bigger crystal volume (or bigger diameter) to compensate in the equations 2.31 and 2.32 and hence this is the affirmation for the difference of the measured d_{50} values for both substances. At lower flow rates, the measured d_{50} values for both substances are very close and tend to deviate stronger at higher flow rates. The same tendency can be seen for the calculated d_{50} values. Moreover, the calculated data for L-asn are in a very good agreement with the experimental data. On the contrary, the calculated d_{50} values for OABA differ at the whole range of flow rates, especially at higher values. Like for the case of L-glu, this can be assigned to the observed formation of crystal agglomerates in the crystallizer due to higher particle-particle interactions, which supposedly occur at higher flow rates.

The experimental and predicted mean crystal size values for L-asn and OABA were additionally compared with microscopic images of samples, taken from outlet IV and shown in Figure 4.24. It can be seen that the plate-like crystals of OABA seems to stick together on their big surface.

Comparing the derived mean crystal sizes with the microscopic images, it can be concluded that the results from FBRM measurements and microscopic observations are in good agreement, although measurements were conducted at two different outlets.

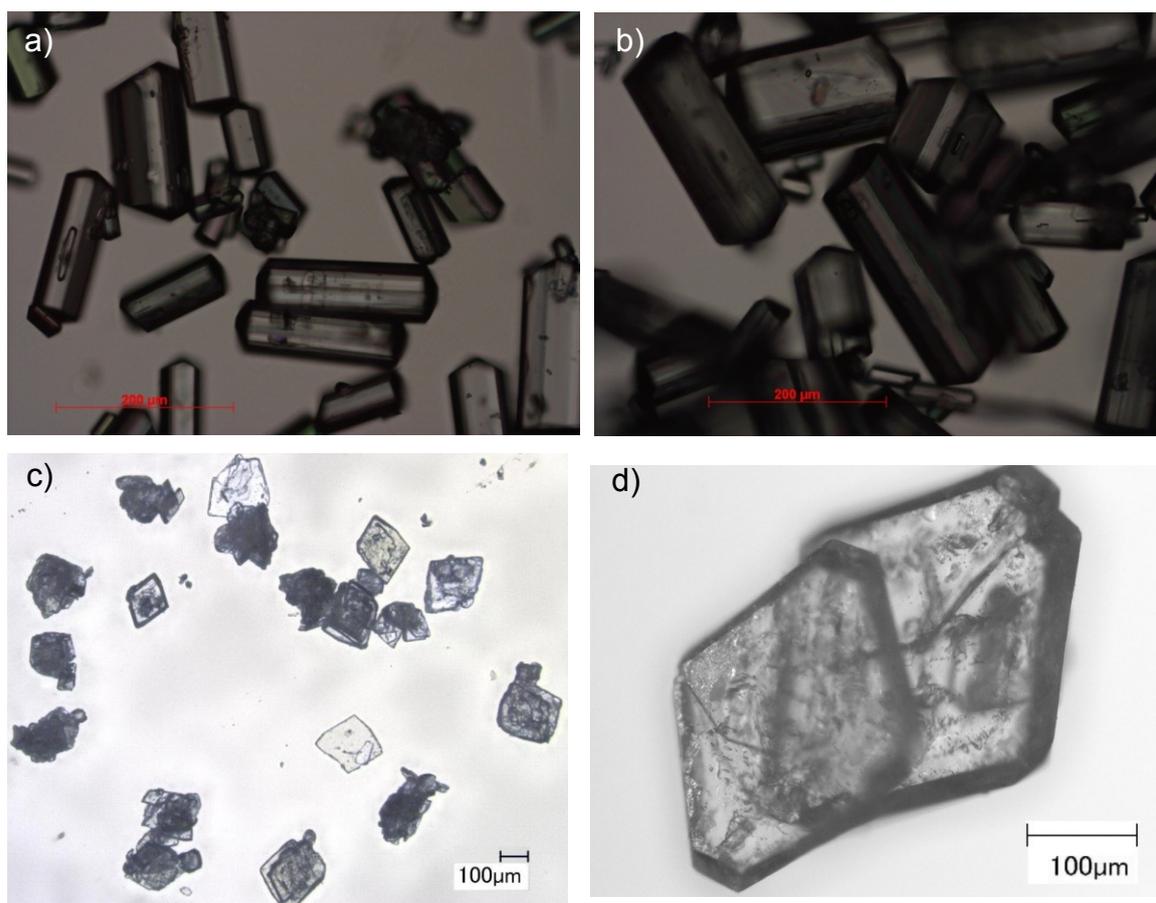


Fig. 4.24 Microscopic images of crystals of L-asn (a and b) and OABA (c and d), taken from outlet IV at flow rates of 6 l/h (a and c) and 15 l/h (b and d).

4.4.2 Temporal approach to steady state operation

To investigate the development of the CSD as function of time in the fluidized bed crystallization of L-glu, two experiments have been conducted at a constant flow rate of 9 l/h. In one, samples were collected every hour from outlet III of the crystallizer and the CSD was measured offline. In the second experiment, a FBRM probe was used for inline measuring of the CSD at outlet III of the FBC. Selected results are shown in Fig. 4.25. Figure 4.25a shows the course of the CSD, measured offline, while Fig. 4.25b represents the CSD, recorded by the inline measurements. The optical rotation and density of the solution with time is depicted in Fig. 4.26.

From figures 4.25a and 4.26 can be seen that after 10-11 h the amount of the bigger crystals ($\sim 250 \mu\text{m}$) and density (respectively concentration) were lowered, while the amount of the crystals with size $\sim 100 \mu\text{m}$ rose. Up to this time point the

Ch. 4 | Results and discussion

supersaturation of the solution in the crystallizer remains constant (there is excess of solid L-glu in the feed-tank). The lowered supersaturation and a respectively slower growth rate of the crystals in the crystallizer are due to the complete consumption of the solid phase in the reservoir after 10-11 hours.

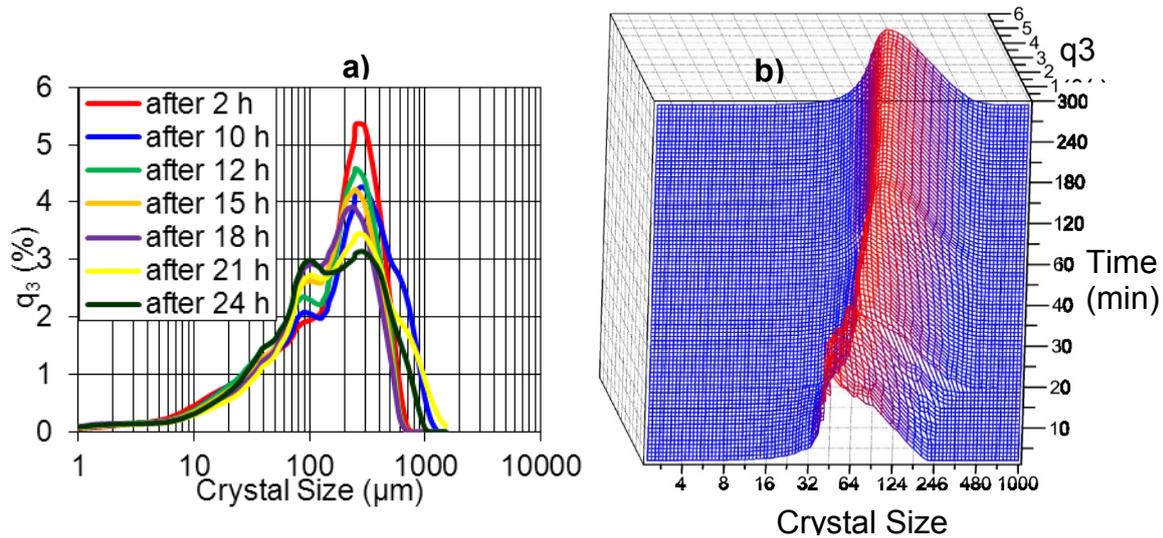


Fig. 4.25 The development of CSD of L-glu as a function of time represented as a) offline and b) in-line measurements.

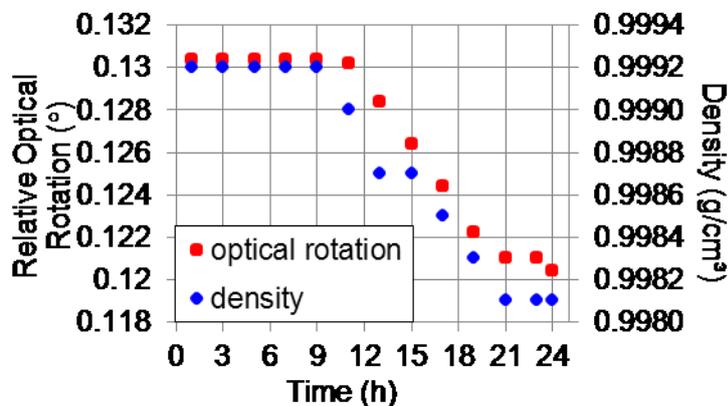


Fig. 4.26 The course of the relative optical rotation (red symbols) and solution density (blue symbols) of L-glu with time. The data corresponds to the experiment, where samples were measured offline.

At the same time, strong agglomeration effects were observed visually inside the crystallizer, thus disturbing crystal growth. Moreover, the increased sizes of the formed agglomerates lead them to the bottom of the crystallizer, where they are taken out to the US bath and crushed. Thus the amount of the crystals with size $\sim 100 \mu\text{m}$ was raised, creating a bimodal CSD. On the contrary, the values for both crystal sizes ($\sim 100 \mu\text{m}$ and $\sim 250 \mu\text{m}$) remained constant in the course of the

experiment. Therefore they were independent from the time and supersaturation respectively, even when the amount of the crystals has changed.

The measured CSDs shown in figure 4.25b represent the course of the crystallization process regarding the L-glu crystal growth in the first 5 hours of the experiment. It can be seen that in the first 60 minutes, crystals grow and the calculated d_{50} values shift slightly from $\sim 80 \mu\text{m}$ at the beginning of the process to $\sim 200 \mu\text{m}$ after 60 min. After 1 hour a steady state regarding crystal size is established and the measured CSDs have almost the same course. A comparison with the previous experiment, where samples were offline measured, it can be concluded, that no seed crystals from the US breakage are detected by the inline measurements. Moreover, the inline measured CSDs are monomodal in comparison to the bimodal CSDs from the offline measurements. This fact may be connected with the fluid dynamic of the upward solution and the placement of the FBRM probe in the crystallizer. The inline measurements are done in the middle of the crystallizer, while by offline sampling, suspension from the whole volume above the outlet III was taken out, thus collecting some of the upward floating crystal fragments from the US seed generation.

4.4.3 Summary

In this section, we discussed results from the influence of the feed rate, seed size and ultrasonic crystal breakage of L-glu, L-asn.H₂O and OABA on the process performance in a single fluidized bed crystallizer setup. The experimental data were compared with predictions, based on the Richardson-Zaki force balance model. The measured CSD of L-glu along the height of the crystallizer as well as the calculated d_{50} show the expected behavior, interrelated to the lower part of the crystallizer being conical. The results for L-asn and OABA showed that with the increase of the flow rate, the mean crystal sizes of the studied substances increase steadily. The Richardson-Zaki force balance model has shown good prediction capabilities of the expected size distributions for L-asn and an increasing diversity at higher flow rates for OABA, most probably due to crystal agglomeration. The simplified assumption of a constant void fraction, ϵ , with changing flow rates might explain the differences between the calculated d_{50}

values with the experimentally determined ones. The received information about the CSD along the height of the fluidized bed crystallizer is very useful for improving the crystallizer's geometry and the height of the product outlets. The influence of the US seed generation and different types of seeds have also shown an impact on the product CSD. Thus, bimodal CSD were obtained under the influence of the continuous US comminution, leading to unification of the CSD along the height of the crystallizer. Thus production of crystals with smaller d_{50} was achieved compared to experiments, performed without US attenuation. The uniformity of the product crystals and the width of their size distribution are directly related to the methods of producing the seed crystals. The use of sieved seed crystals followed by ultrasonic attenuation to initiate the crystallization process is derived to give optimal results, such as narrow CSD and uniform product crystals. The study on the development of the CSD as function of time in the fluidized bed crystallization has shown that for L-glu after approximately 1 h from the start of the experiment, the crystallization process was in steady state concerning the measured CSDs. This means that product crystals with uniform CSD can be collected over time from outlet III of the FBC.

4.5 Experiments in two coupled fluidized beds

In this section, results from the continuous preferential crystallization of OABA and PABA from their 50:50 aqueous solutions as well as L-asn.H₂O and D-asn.H₂O from their racemic solution will be presented. Before conducting the experiments, the results for the MSZW in the crystallization setup for both ternary systems will be summarized. The experimentally determined concentration trend will be compared with the results from the dynamical model. In order to complete this goal and based on the results from the previous section, two fluidized bed crystallizers were constructed with the same geometry as the one from the single FBC setup. Only one outlet was provided for the product removal at the height of the outlet III ($x_p = 365$ mm, see Fig. 4.1) from the single FBC setup. More information about the construction and operation of the setup is given in chapter 3.2.3.

4.5.1 Continuous crystallization of aminobenzoic acid stereomers

- Determination of MSZW in the crystallization setup

A summary of the results from the determination of the MSZW of aqueous solutions of a 50:50 mechanical mixture of OABA and PABA is shown in Table 4.5, where T_s is the saturation temperature and T_{cr} – the temperature of the crystallizer.

Table 4.5 Measurements of the nucleation time, performed isothermally in the experimental setup under the influence of the ultrasonic attenuation. The nucleation time, t_{nucl} , represents the time between the start of the experiment and the detection of nucleation in the crystallizer.

T_s [°C]	T_{cr} [°C]	Supersaturation [-]	t_{nucl} [h]
35	22	1.81	~ 2.5
35	25	1.57	~ 6.5
35	28	1.37	> 24

It can be seen that at supersaturation values of 1.81 and 1.57 the nucleation took place within a short time (2.5 and 6.5 hours respectively). It should be noted, that the formation of the nuclei could possibly happen at earlier time, than shown in the table. But due to the constant upflow of the solution in the crystallizer ($u_f = 10.5$ l/h), the newly formed nuclei are easily swept away with the flow and then dissolved in the feed tank, thus not triggering a detectable concentration shift. The critical size, above which a crystal is not swept away with the flow was not measured due to experimental difficulties, but eventually can be calculated. In chapter 4.4.1.1, it was experimentally proven that particles with sizes above 60 μm are definitely not swept away with the flow (9 l/h) and remained in the crystallizer. As the residence time of the fluid in the crystallizer is about 257 s at a flow rate of 10.5 l/h, an empirical assumption for OABA crystal growth can be made taking a supersaturation of 1.57 in account and using eq. 4.3. Thus, the calculated minimum size of newly formed at the bottom of the FBC nuclei, not flown out from the top of the crystallizer, is equal to 15 μm . In order to minimize this possibility, the following preferential crystallization experiments were performed at a crystallization temperature of 27 °C, while maintaining a supersaturation of 1.43.

- *Continuous selective preferential crystallization of OABA and PABA*

Continuous preferential crystallization in the coupled FBCs was conducted with a 50:50 mixture of OABA and PABA in water. The start parameters for the process are given in Table 4.6, while the results are presented in Table 4.7.

Table 4.6 Experimental conditions for the preferential crystallization experiments.

saturation temperature	34.9 °C
crystallization temperature	26.8 °C
solution concentration	1.52 wt. %
supersaturation	1.43
amount of initial seed crystals supply	76 µm
seed d_{50}	8 g
feed flow rate	10.5 l/h
suspension flow rate	18 l/h
excess amount of solid in tank (OABA+PABA)	10+10 g

Table 4.7 Experimental results from the preferential crystallization experiments

total product recovery OABA / PABA	11.15 / 11.59 g
product d_{50}	175 µm
purity OABA / PABA	97 / 97.9 %

As seen from Table 4.6, the initial concentration of the 50:50 aqueous solution of OABA and PABA is 1.52 wt.% at 34.9 °C, while the saturated solution concentration at 26.8 °C is about 1.00 wt.%. Thus, the concentration difference at 26.8 °C is ~ 0.52 wt.%, which corresponds to a theoretical yield of ~ 5.2 g/kg for both substances, or ~ 2.6 g/kg per single isomer (yield is equal to the concentration difference multiplied by a 1 kg solvent). Recalculated by taking into account the amount of solvent used (7460 g) and the excess solid in the feed tank (20 g), gives ~ 29.4 g product of each substance at the end of the crystallization process (yield = $(20 + 7460 * 0.0052) / 2$). Hence, the mean productivity of the coupled fluidized bed crystallization setup when the process is in steady state (see Fig. 4.29 below) is about 4.27 g/(l.h) per isomer. At steady state, the productivity per crystallizer volume per hour is given as the excess amount of solids in feed tank divided by the time the process is in steady state. In our case, a correction factor of 1.28 is used as the actual crystallizer volume is 0.78 l and the productivity is given per liter (i.e. the total collected mass of single

isomer crystals at the end of the experiment, multiplied by 1.28, and divided by the total time the process was in steady state of 3 h).

As seen from Table 4.7, the collected mass of OABA (11.15 g) and PABA (11.59 g) is less than the theoretical yield. Hence, the product outlet is 365 mm above the bottom of the fluidized bed crystallizer, thus forming a volume of about 125 ml filled with crystal suspension, which cannot be collected. Moreover, the loop, connecting bottom of the crystallizer with the ultrasonic bath has also a volume of 120 ml, again filled with crystal suspension. A prediction of the crystal mass in this nonrecoverable suspension volume could be made, based on the calculated void fraction at the bottom outlet of the crystallizer, by using the equation

$$m_{s,cr}^* = V_{cr}^*(1 - \varepsilon_{us})\rho_p \quad (4.18)$$

where $m_{s,cr}^*$ is the mass of the remaining crystals in the crystallizer; V_{cr}^* is the total volume ($V_{cr}^* = 125 + 120$ ml) of the crystal suspension, that cannot be recovered; and ε_{us} is the calculated void fraction at the bottom of the fluidized bed crystallizer. The calculated mass value of 16.1 g is in good agreement with the value, subtracted from the calculated theoretical yield with the experimental yield thus resembling the mass of the nonrecoverable crystals from the suspension (~ 18 g). The difference of 1.9 g between both values can be due to discrepancies in the solid density in the suspension, leading to divergence of the values for the void fraction in the bottom of the crystallizer and the one in the tubing. To initiate the crystallization process, 8 g of seeds of each substance were used. This is about 27% of the expected theoretical product yield. The needed seed mass can be calculated using equation 2.18 and is usually between 0.1 and 4 % of the expected product mass [Beckmann2000, Heffels1999]. In our case, this is not applicable, as more particles are needed in order to form a fluidized bed. As already shown in chapter 4.4.2 for the case of crystallization of L-glu, the steady state condition is achieved within 1 h after the initiation of the crystallization process through seeding as well as steady continuous seed generation through the US bath to maintain the growth of the fluidized bed.

From table 4.6 can be seen, that suspension flow rate is relatively high (18 l/h), in comparison with the one (2 l/h) for the crystallization experiments, done with L-

glu in the single FBC setup (see chapter 4.4). The need for higher flow rate is due to the fast formation of crystal agglomerates in the tubes to/from US bath and to avoid their settling in the tubing, thus blocking the suspension flow. Because of the higher suspension flow rate, the residence time of the bigger crystals and agglomerates in the US seed generation loop is increased. According to the results from the US comminution experiments (chapter 4.3), the necessary residence time needed to comminute a suspension of crystals, having a median size of $\sim 200 \mu\text{m}$ to the half of it, is 5 to 10 min. With the suspension flow rate of 18 l/h, the crystals and agglomerates from the bottom part of the crystallizer are forced to loop multiple times through the US bath in order to get broken into smaller crystals. Thus, the amount of generated seeds per time is lowered, which directly impacts the productivity of the FBC setup.

During the crystallization process, several observations were made. At the beginning of the process, the introduced seeds were forming agglomerates inside the crystallizer. For this reason, the fluid flow was set to a lower flow rate in order to take the agglomerated seed suspension out of the crystallizer to the ultrasonic bath, where all the agglomerates were fractured into individual seed crystals. After 1 hour, crystal agglomerates start to form again, see Fig. 4.27.

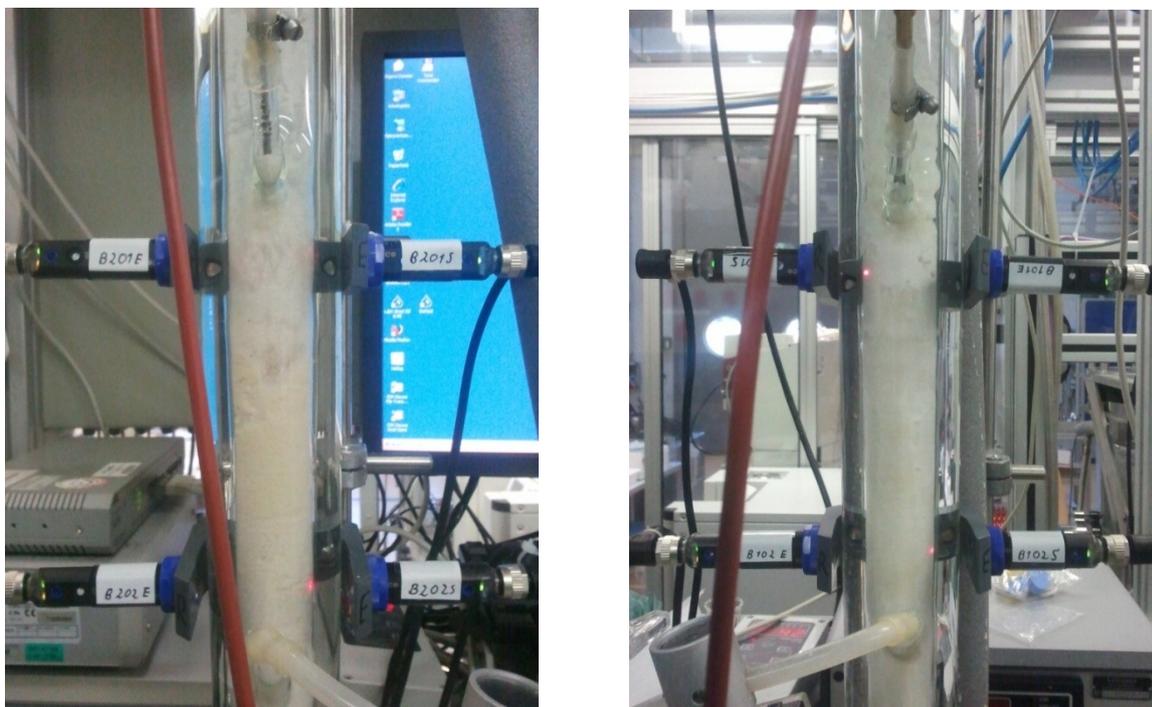


Fig. 4.27 Formation of crystal agglomerates inside both fluidized bed crystallizers (**left:** crystallization of PABA, **right:** crystallization of OABA).

Moreover, the incrustation on the internal crystallizer wall clamped the formed agglomerates, thus partially obstructing the fluidized crystal bed. As a consequence, the detector signals were permanently blocked, which kept the product outlet permanently open. As already mentioned in chapter 3.2.3, product crystals were collected batchwise (about once per hour). Because of that, the automatic takeout of the product crystals was set to manual. During the process, the OABA product crystals were collected two times and PABA product crystals – three times.

Important requirements of the crystallization processes are the quality and the purity of the product crystals. In figure 4.28, the experimental crystal size distributions for the OABA seeds and product crystals are shown along with their respected calculated CSDs. The latter are derived from the product crystal size, L_p , by applying the cumulative distribution function (CDF). In the figure is shown for comparison a microscopic photograph of product crystals.

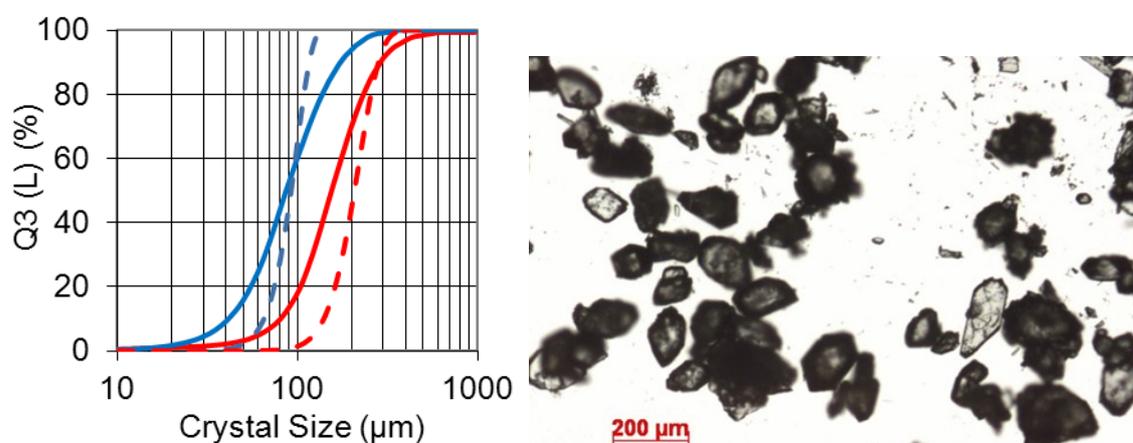


Fig. 4.28 Left: Experimental (solid line) and calculated (dashed line) cumulative CSDs for OABA seed (blue color) and product (red color) crystals. **Right:** Microscopic photograph of the OABA product crystals.

From the microscopic image in fig. 4.28 can be seen that the produced product crystals are more or less uniform in size and show relatively narrow CSD. The calculated CSDs are in fairly good agreement with the experimental ones. The derived values are based on the calculated crystal size, L , and extended to CSD using the CDF. The measured experimental CSD include the seed crystals from the US loop, seen also in the photograph, hence the difference of the experimental cumulative distribution with the predicted one. This was expected

as seeds from the US fracturing float from the bottom of the crystallizer to the top through the fluidized bed and were captured with the product takeout. The CSD of the biggest crystals, found at the bottom of the fluidized bed crystallizer can be predicted from the calculated crystal size, taking into account equations 2.31 and 2.32. These values were used to generate the CSD for the seeds from the ultrasonic bath as well as for the tuning of the calculation of the total number of crystals in the crystallizer in eq. 4.14.

A prediction of the crystallization process development was also done by using the simplified dynamical model, described in chapter 4.1 with process parameters given in Tables 4.6 and 4.8. Along with the prediction of the product CSD, the total time when the process is in steady state can be predicted.

Table 4.8 Parameters needed for the mathematical calculations.

Solution density at 35 °C	994.6 kg/m ³
Solution viscosity ¹	6.531*10 ⁻⁴ Pa.s
Standard gravity	9.80665 m/s ²
Growth rate of OABA [Temmel2014]	1.7524*10 ⁻⁷ m/s
Total solution volume	8 l

¹ – the viscosity of water at 40 °C was taken as the solution viscosity

In figure 4.29 are shown the experimental and predicted solution concentration changes with time from the preferential crystallization of OABA and PABA in a 50:50 solution of both substances. It can be seen that the solution concentration, that at the start of the process remains unchanged for 3 hours. In this time frame, the solution from the return flow from the FBC is constantly saturated from the dissolution of the solid OABA and PABA in the feed tank. After 3 hours the mass of the solid substance in the feed tank is depleted, thus the concentration of the feed solution drops as well as the supersaturation in the crystallizer. After the solution concentration in the crystallizer equals the solubility concentration of the substance, the crystallization process stops. Hereby, the measurement of the solution concentration during the process was done through a densitometer. The collected density values were then converted to weight percent.

It can be seen, the calculated concentration is in fairly good agreement with the experimental one. From the beginning of the process until 2.5 hours both show straight line, as the excess of solids in feed tank are not dissolved. After this time

the calculated concentration values start to decrease due to the assumptions taken into account (see chapter 4.1).

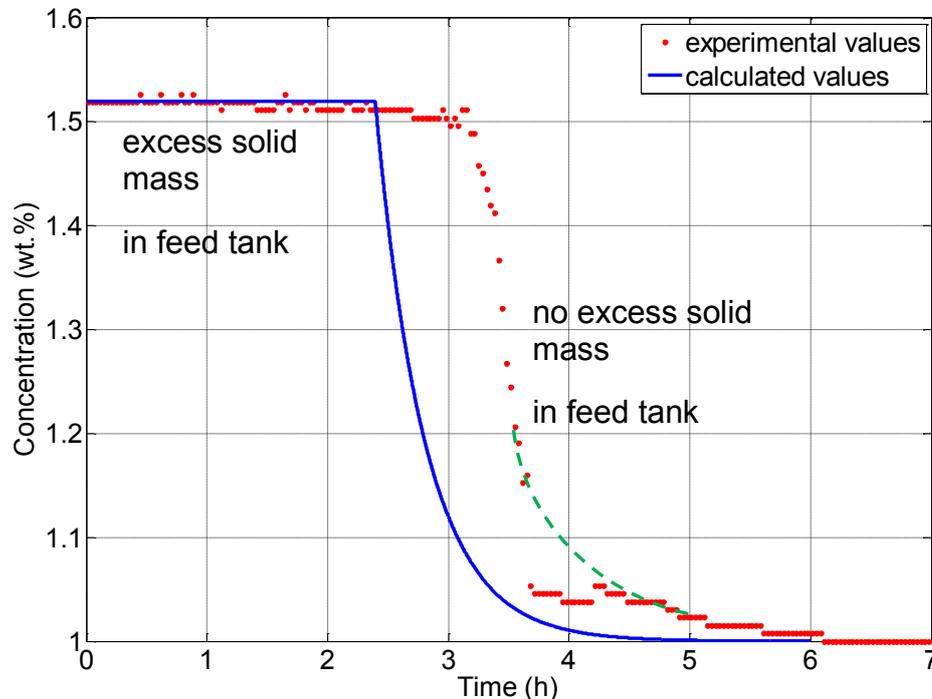


Fig. 4.29 Experimental and calculated (model described in section 4.1) solution concentration development of OABA and PABA in the fluidized bed crystallizer with time. Conditions are shown in Table 4.6.

The calculated with eq. 4.7 amount of the solids in the crystallizer is subtracted from the amount of the excess solid in the feed tank. Because the speed of the desolvation process is quicker than the crystallization one, no change in the solution concentration is calculated. When the amount of the crystallized solid exceeds the amount of excess solid in the feed tank, the concentration development is then calculated with eq. 4.6. At this point, the fluidized bed crystallization process continues in batch mode with respect to the solution concentration. The increase of the particle quantity in the crystallizer due to the generated seed crystals in the US-bath is empirically estimated and its change is included in eq. 4.14. Hence, the removal of product crystals is implemented with eq. 4.8, thus also making an impact on the particle quantity in the crystallizer and indirectly influencing the solution concentration development after depletion of the excess solid in the feed tank. After depletion of the excess solids in the feed tank, both concentration development curves show almost the same behavior until

concentration value of about 1.15. At this point the shift to the lower concentration values from the experiment could be eventually due to clogged filter, thus contaminating the density measurement. A possible trend of the experimental concentration development is shown with the green dashed line. After 6 hours the crystallization process is over with only fluidization process running. The total time duration of the experiment was almost 17 hours, from which the last 11 hours only fluidization of the crystal bed took place. In figure 4.30, the measured temperatures of both crystallizers, feed tank and US bath are shown (left y-axis), along with the concentration development (right y-axis).

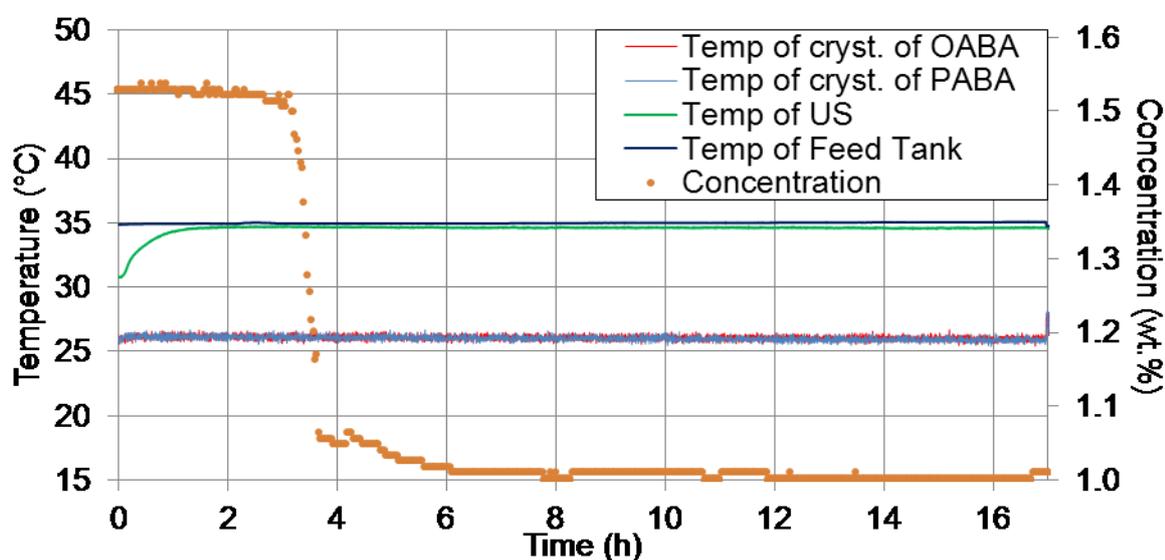


Fig. 4.30 Trajectories of the temperature in the both crystallizers, feed tank and US bath and solution concentration development with time for the whole experiment.

It can be concluded from the figure that except for the time of the concentration development after the depletion of excess solid in feed tank, the whole experiment was conducted with almost no change of the parameters shown. A temperature offset of 4 K was set for the US bath tempering, which was estimated during the US seed generation experiments given in chapter 4.3. Under continuous ultrasonication, the temperature in the bath slowly rises with time due to the local formations of cavities, resulting in high energy implosions. This phenomenon is also reported from other research groups [Dennehy2003, Rucroft2005].

4.5.2 Continuous crystallization of asparagine enantiomers

- *Determination of MSZW in the crystallization setup*

Before conducting the crystallization experiments, a determination of the MSZW in the crystallization setup is needed additionally to the measurements done in the laboratory (see chapter 4.2). Hence, the stability of the supersaturated solution over time was studied under the influence of the ultrasonic attenuation in the seed generation loop. The results from the experiments performed at different temperatures are shown in Table 4.9.

Table 4.9. Stability of the supersaturated solution under the influence of the ultrasonic attenuation expressed as time until nucleation occurs (t_{nucl}). The nucleation time, t_{nucl} , represents the time between the start of the experiment and the detection of nucleation in the crystallizer.

T_s [°C]	T_{cr} [°C]	Supersaturation [-]	t_{nucl} [h]
35	20	1.88	1
35	24	1.55	3
35	27	1.37	> 24

All the experiments were performed isothermally by setting the temperature of the crystallizers at the specific value (T_{cr}) and without seeding. It can be seen that at supersaturations of 1.88 and 1.55 the nucleation took place within a short time (1 or 3 hours respectively). To avoid the unwanted nucleation and thus contamination in the continuous crystallization, all following separation experiments were performed at a crystallization temperature of 27°C and a supersaturation of 1.37 respectively.

As already pointed out earlier in this subsection, the critical size of a crystal, which is not swept away with the flow, can be calculated. Thus, an empirical assumption from L-asn.H₂O crystal growth can be made, using eq. 4.3, by taking a supersaturation of 1.37 into account and further applying the Richardson-Zaki relation (eq. 2.28). Thus at a flow rate of 9 l/h (fluid residence time in FBC is 312 s), the calculated minimum size of newly formed at the bottom of the FBC nuclei, not flown out from the top of the crystallizer, is equal to 37 μm. Hence, by the chosen supersaturation level of 1.37, it is highly unlikely for the nucleation process to occur at the chosen experimental conditions.

- *Continuous selective preferential crystallization of asparagine monohydrate enantiomers*

Continuous preferential crystallization of L-asn.H₂O and D-asn.H₂O from an aqueous solution of DL-asn.H₂O in coupled fluidized bed crystallizers setup was conducted. The start parameters of the process are given in Table 4.10 and the results from the experiments are summarized in Table 4.11. The trajectories of the solution concentration and relative optical rotation in both crystallizers are presented in Figure 4.31. The analytical equipment (densitometer and polarimeter) was calibrated prior to the experiments. The measured optical rotation is relative to the initial value, which for DL-asn.H₂O is equal to zero. The time, shown in Fig. 4.31 is relative to the start of the crystallization process (time = 0) by adding seeds to both fluidized bed crystallizers.

Table 4.10 Experimental conditions for the preferential crystallization process.

Saturation temperature	35 °C
Crystallization temperature	27 °C
Solution concentration	8.76 wt. %
Supersaturation	1.37
Mass of seed crystals	4 g
Seed d ₅₀ (both enantiomers)	55 µm
Feed flow rate	9 l/h
Suspension flow rate	4 l/h
Excess of solid DL-asn.H ₂ O in tank	80 g
Solution density at 35 °C	1031 kg/m ³
Solution viscosity at 35 °C [Seebach2011]	8.5*10 ⁻⁴ Pa.s
Growth rate of L-asn.H ₂ O [Seebach2011]	1.117*10 ⁻⁶ m/s

Table 4.11 Results from the preferential crystallization experiments.

Total product recovery L-asn.H ₂ O / D-asn.H ₂ O	46.2 / 49 g
Product d ₅₀ (both enantiomers)	184 µm
Enantiomer purity L-asn.H ₂ O / D-asn.H ₂ O	97 / 97.9 %

After addition of 4 g of seed crystals of the pure enantiomers in the respected crystallizer, the crystallization process was initiated, indicated by a small change in the solution density (i.e. concentration) values, detected in both crystallizers. Afterwords, a steady state operation was observed confirmed by both analytical circles, which show nearly the same values for the solution concentration.

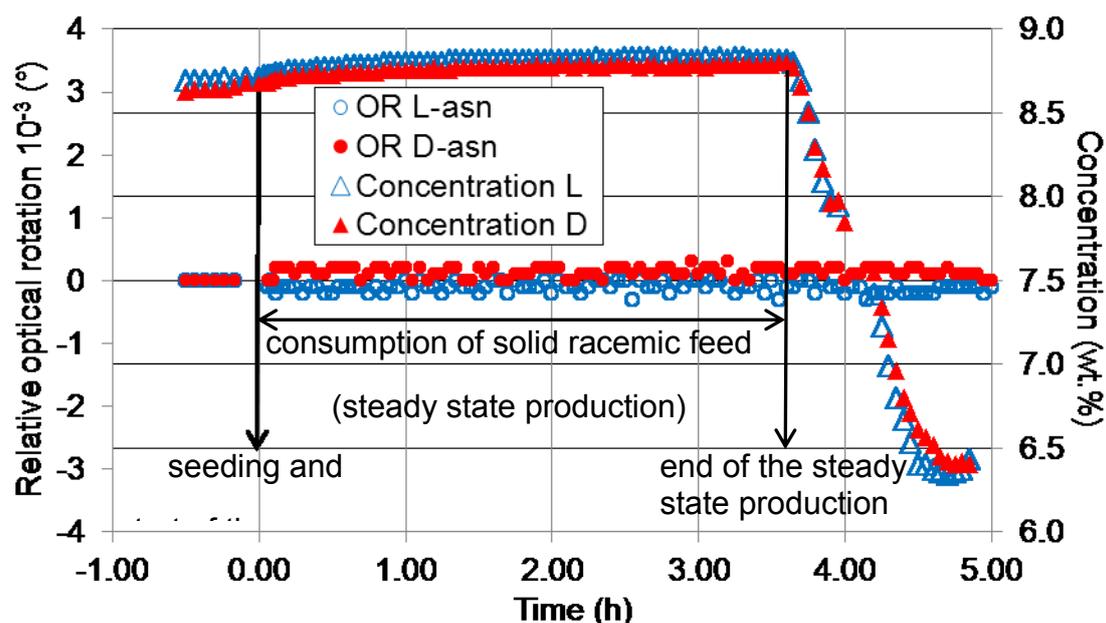


Fig. 4.31 Trajectories of the total solution concentration and relative optical rotation with time for the preferential crystallization experiment. Solution measurements, done in the crystallizer, where L-asn.H₂O crystallized are shown in blue color and solution measurements, done in the crystallizer, where D-asn.H₂O crystallized are shown in red color. Time axle is zeroed at the point, when respected seeds are added to respected crystallizer.

The constancy of the solution concentration shows that the dissolution rate of the excess solid DL-asparagine monohydrate in the feed tank is equal to the crystallization rate in the crystallizers. The two absolute values for the optical rotation are very close, just with the opposite sign. This means that a very small excess of the counter enantiomer is detected in the mother liquor. The almost constant optical rotation values show that the enantiomer ratio remains stable with the time. The two asparagine enantiomers clearly possess equal crystallization kinetics. Every hour a 150 ml fraction of the crystallization suspension was collected from the product outlets of the crystallizers. After 220 min the excess racemic solid in the feed tank was completely depleted and the supersaturation started to decrease, thus lowering the crystallization rate. After further 60 min the crystallization process was stopped (at 4.7 h in Fig. 4.31) and residual product crystals were collected. The crystallized product recovery was in total 95.2 g (46,2 g of L-asn.H₂O and 49 g of D-asn.H₂O). The mean enantiomer purity of the product enantiomer crystals exceeded 97% (measured by HPLC). A productivity of 28 g/(l.h) (or 14 g/(l.h) per enantiomer) was calculated by taking into account only the steady state of the crystallization process (i.e. the total

collected mass of enantiomer crystals at the end of the experiment divided the total time the process was in steady state of 3.67 h or 220 min). A comparison with the calculated theoretical yield, based on the solubility data of DL-asn.H₂O for 35°C (8.76 wt.%) and 27°C (6.324 wt.%), shows that about 24.4 g/kg of DL-asn.H₂O can be crystallized (yield is equal to the concentration difference multiplied by a 1 kg solvent). Recalculated for the amount of solvent used (7700 g) plus the excess solid in the feed tank (80 g), gives a total mass of 267.6 g of DL-asn.H₂O, or ~ 133.8 g of each enantiomer at the end of the process (enantiomer yield = $(80 + 7700 * (0.0876 - 0.06324)) / 2$). As already mentioned, the possible crystal mass recovery of each substance is less than the theoretical yield. The reason for this was already elucidated in the discussion of the preferential crystallization of ABA. Nevertheless, the residual crystal mass can be calculated by applying eq. 4.19 and taking into account the substance respected parameters. The calculated value of 76 g ($\epsilon_{us} = 0.8$) of the nonrecoverable enantiomer crystals is in fair agreement with the theoretical yield of 87.6 g of the remaining amount of crystals (total theoretical yield of 133.8 g subtracted with 46.2 g experimental recovery) for L-asn.H₂O.

From table 4.10 can be seen, that suspension flow rate is relatively low, compared to the one used for preferential crystallization of ABA stereomers (4 l/h in comparison with 18 l/h, respectively). In this case almost no agglomerates were formed and no crystal settling was detected in the tubing. Thus, the residence time of the bigger crystals and agglomerates in the US bad is sufficient with respect to seed generation.

Microscopic photographs of the collected L-asn.H₂O product crystals as well as the experimental crystal size distributions for the L-asn.H₂O seeds, L-asn.H₂O / D-asn.H₂O product crystals are shown in Fig. 4.32 together with their calculated cumulative CSDs. Again, the calculated CSDs are derived from the calculated mean product size, L_p . Obviously besides product crystals, a small portion of seed crystals can be noticed as already shown in previous chapter (Fig. 4.28). A possible reason for the presence of the seeds generated by ultrasonic attenuation is when floating from the bottom of the crystallizer through the crystal bed to its top, they were partly captured by the product separation process. The

CSD of the product crystals shows that crystals with mean size of $\sim 180 \mu\text{m}$ are collected.

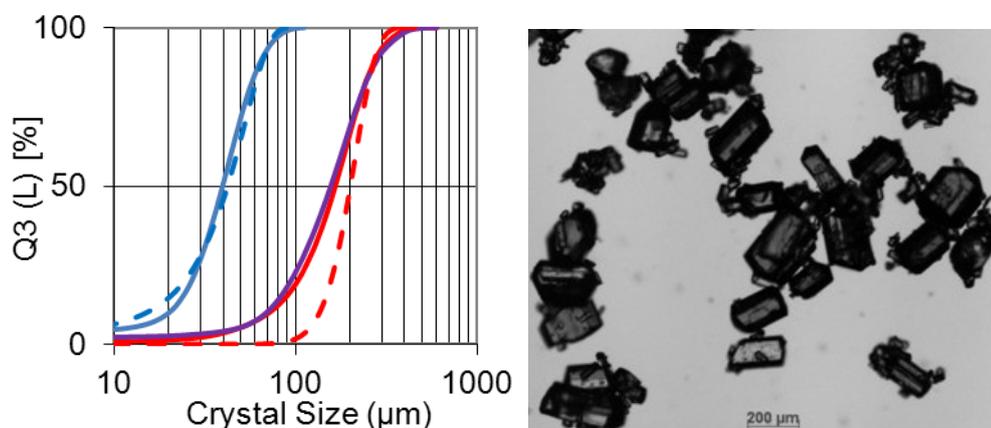


Fig. 4.32 Left: Experimental (solid line) and calculated (dashed line) cumulative CSDs for L-asn.H₂O seed (blue color), L-asn.H₂O / D-asn.H₂O product crystals (red / violet color respectively). **Right:** Microscopic photographs of the L-asn.H₂O product crystals.

In Figure 4.33 are shown the predicted solution concentration development with time and compared with the experimentally measured one. The measurement of the solution concentration during the process was done through a densitometer. The collected density values are then converted to weight percent. For the prediction of the solution concentration, the simplified dynamical model presented in chapter 4.1 was used with process parameters given in Table 4.10. As already elucidated by the discussion of the preferential crystallization of OABA and PABA, the calculated predictions for the preferential crystallization of L- and D-asn.H₂O could be seen as a validation of the mathematical method introduced.

The predicted solution concentration development is in good agreement with the experimentally measured one, as both curves show almost the same behavior. From the beginning of the process until about 3.5 hours both show straight line, as the excess of solids in feed tank are not dissolved. After this time the concentration values start to decrease, after depletion of the excess solids in the feed tank. After ~ 5 hours the crystallization process is over with only fluidization process running.

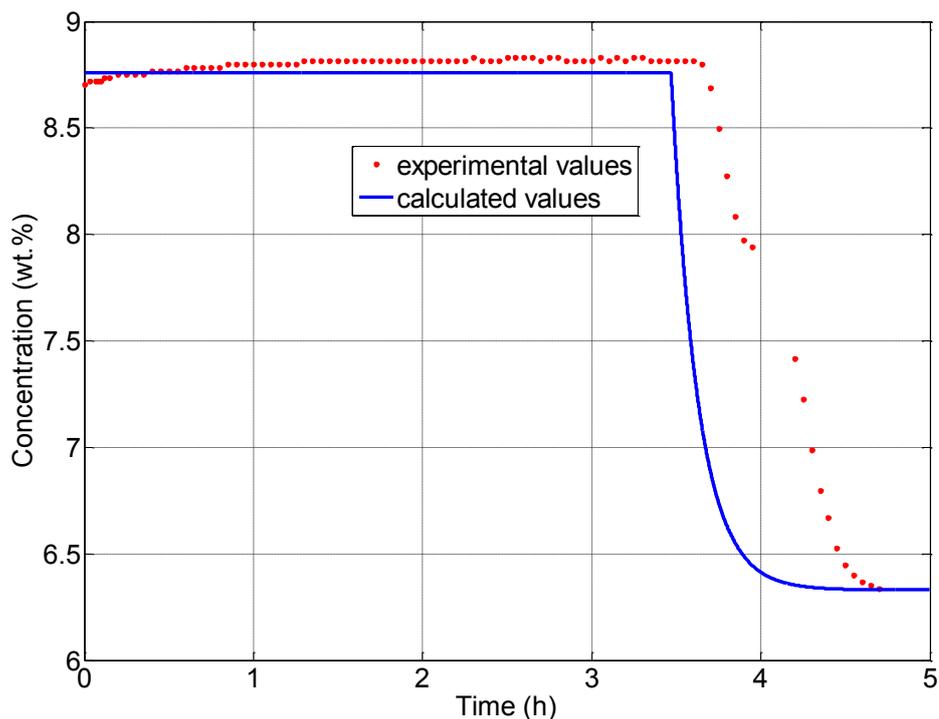


Fig. 4.33 Experimental and calculated (model described in section 4.1) solution concentration development in the fluidized bed crystallizer for the DL-asparagine monohydrate solution with time. Conditions are shown in Table 4.10.

4.5.3 Summary

A continuous selective preferential crystallization in two coupled fluidized bed crystallizers was conducted in conjunction with a fluidized bed process on the example of the two ternary systems OABA / PABA / water and L-asn.H₂O / D-asn.H₂O / water at the eutectic point. The resultant product crystals featured high purity and sustained a stable and narrow crystal size distribution throughout the duration of the process. The productivity of the crystallization process depends on the kinetic parameters of the specific substance and for the time, the process was in steady state, has shown 4.27 g/(l.h) for the aminobenzoic acid isomers, and 14 g/(l.h) for the asparagine enantiomers. For comparison, the productivity of L-threonine was 12 g/(kg.h) from the continuous selective preferential crystallization in the threonine ternary system in a coupled batch crystallizer setup by applying similar initial conditions ($T_{cr} = 26\text{ }^{\circ}\text{C}$, $T_s = 33\text{ }^{\circ}\text{C}$, exchange flow rate between crystallizers $\sim 34\text{ l/h}$ and initial seed mass of 2.5 g) [Elsner2007,

Elsner2011]. The build-up of strong agglomeration in both crystallizers and the probable seed crystals flowing out from the top of the crystallizers could be the main issue for the low productivity of the aminobenzoic isomers in comparison with the asparagine enantiomers. By the crystallization of the aminobenzoic acid isomers, only polymorphs of type I for OABA and α -form for PABA were produced and no polymorph transitions were detected. The introduced simplified mathematical model has shown good prediction capabilities of the solution concentration development in both cases. Moreover, the predicted product CSDs are in very good agreement with the experimentally measured ones.

It can be concluded that the constructed fluidized bed crystallization setup, consisting of two coupled fluidized bed crystallizers, is capable of continuous production of substances. Continuous selective preferential crystallization was successfully conducted for two ternary systems, forming simple eutectic in their solubility phase diagram.

4.6 Equipment based recommendations

This work aims to expand the current knowledge and to provide a detailed study on the continuous production of pure crystals with defined and possibly narrow size distribution in a novel crystallization setup, based on the fluidized bed technology.

In order to increase the scale of operation and to further extend the applicability of the proposed crystallization method and setup, more investigations are required, because current understanding of the actual behavior of the fluidized bed process is still limited. Based on the current state of research in this work, possible process enhancements and setup improvements can be proposed:

1. The experimentally collected information about the CSD along the height of the fluidized bed crystallizer is very useful for improving the reactors geometry and the height of the product outlets. Still comprehensive studies on the fluid dynamics inside the FBC are needed. Moreover, the loss of the small crystals due to the flow rate could be reduced by enlarging of the top part of the crystallizer. Then, the flow rate is reduced, based on the Bernoulli's principle, thus increasing the residence time of the crystals in the respected crystallizer volume, leading to an increase in their sizes due

to crystal growth and thus resulting in an increase of the productivity through the reduction of the amount of crystals, flown away from the top of the FBC. However, this could lead to accumulation and growth of the eventually formed nuclei, which in the case of the selective preferential crystallization process is undesirable. The geometry of the whole fluidized bed crystallizer could be also further optimized and improved. This includes: an increase of the crystallizer diameter; a change of the proportion of the conical bottom part to the tubular upper part; an integration of the US transmitters in the bottom part of the FBC.

2. The almost horizontally conducted suspension transport between the bottom of the crystallizer and the US bath in its actual assembly is incapable of longer operating times due to the formations of agglomerates and relatively high chances of blocking the tubing. The implementation of an inclination of the suspension transport by lowering the position of the US bath against the FBC could lead to accumulation of the suspended crystals in the US-bath and therefore increasing their residence time there. Thus, only smaller crystals could be transported through the inclined tubes and reach the bottom part of the FBC.
3. The generated seed crystals are supplied at the bottom of the crystallizer, thus by the product takeout some of them are withdrawn with the suspension, leading to productivity loss and influencing the product size distribution. On the other side, longer residence time for the freshly generated seeds is needed to reach their critical size and not to be flown away from the top of the crystallizer. An inlet of the crystal suspension above the product outlet could avoid collecting of the seed crystals with takeout flow and when combined with an enlargement of the top part of the crystallizer as proposed in point 2, thus enough residence time for seed crystals to grow can be assured, as well as increased productivity and narrow product size distribution.
4. In order to keep the crystallization process running, solid raw material should be supplied in the feed tank. This leads to a formation of a suspension with a variable density and thus to an increasing probability of clogging the suction filters with time. As a result, the operation of the gear

pump is endangered and fluctuations in the flow rate could be registered. In order to overcome this imperfection a second feed tank can be attached between the actual feed tank and the tubing from the crystallizers, where the dissolution of the solid material could take place. Moreover, the slightly undersaturated solution, which may contain fine solid particles, can be also collected and used to dissolve the solids. As a result, solid-free feed tank could be operated.

5. By the construction of the double jacketed vacuum filters, its bottom part is currently made flat, which could lead to possible formation of crystal clusters and agglomerates and thus clogging the filter outlet to the feed tank. A reconstruction of the filter geometry in a funnel-like form is suggested in order for the mother liquor directly to flow out without a possibility of crystal settling.

5. Conclusions

In the frame of this work a concept for performing selective crystallization in a fluidized bed was studied, where under specific conditions (supersaturation, temperature, flow rate, etc.) crystals can increase their size and can be in parallel classified due to their distribution along the height of a specifically shaped crystallizer. The idea for this work originates from publications of Midler, who successfully realized the combination of a continuous crystallization process with a fluidized bed regime. The constant generation of seed crystals, needed to maintain a growth dominated continuous crystallization process, was realized in this work externally through ultrasonic comminution of crystals and crystal agglomerates, continuously removed from the bottom of the crystallizer. Product crystals with specific sizes could be collected from an outlet at a specific height of the crystallizer. A systematic study of the applicability of the joint action of these processes with respect to the properties of the product crystal size distribution was conducted.

In the following, the main contributions of this work are summarized:

1. Three industrially relevant substances have been used for testing the concept. Two of them are exhibiting chirality (the chiral systems of glutamic acid and asparagine), while the third (aminobenzoic acid) is a stereomeric system, featuring three positional isomers.
2. In order to optimally conduct the crystallization process, fundamental preliminary studies of solubility equilibria and metastable zone width of the three substances in water were performed using isothermal and polythermal methods. The collected data reveal that the solubilities of the substances increase with the increase of the temperature, although they remain relatively low in comparison with inorganic salts even at high temperatures. Further, ternary solubility phase diagrams were constructed for the systems L-asn.H₂O / D-asn.H₂O / water and OABA / PABA / water. The results indicate that in both cases a simple eutectic is formed based on the shape of the solubility isotherms, the course of the corresponding tie lines, and particularly on the

measured XRPD diffractograms of the resultant solid phases. The type of both ternary phase diagrams corresponds to conglomerate-forming systems of type I.

3. In further preliminary experiments devoted to maintain the continuity of the crystallization process, the ultrasonic comminution of crystals was studied as an alternative to the commonly used wet milling. Two different experimental setups were constructed. In the batch experimental setup, the pure crystal breakage process was studied and its effectiveness in lowering the mean crystal sizes with time was shown. The construction of the continuous experimental setup was needed to check the implementation of the ultrasonic seed generation, when crystal suspension is continuously transported through the ultrasonic bath. Hence, the continuous seed generation has shown even better results in comparison with those from the batch process, as the process was facilitated by the peristaltic pump used. By applying 10% of the maximum power of the ultrasonic bath, a mean residence time of 5 min was demonstrated to be sufficient for producing seed crystals of desired size.
4. Inspired by Midler's work, a pilot-plant experimental setup having a double jacketed glass-made tubular fluidized bed crystallizer with several outlets along its height was designed, constructed and applied. For collection of product crystals under appropriate conditions, a double jacketed glass-made vacuum filter was also designed, constructed and applied.
5. Crystallization experiments using L-glutamic acid as the model substance were conducted in a single fluidized bed crystallizer setup with embedded seed generation loop. During the experiments, the influence of the feed rate, ultrasonic crystal breakage and type of seeds on the product size distribution was studied. Three different feed flow rates were used to study the crystal size distribution of L-glu along the height of the crystallizer. It was shown, that with increase of the flow rate, the d_{50} values, calculated from the respected CSDs, also increase. As a result, a substantial linear function of the increasing mean crystal size was achieved with the increasing volume flow for all substances. In addition, the influence of the ultrasonic breakage on the total CSD in the crystallizer was studied by using the same flow rates. The use of the ultrasonic attenuation has led to unification of the CSD along the

height of the crystallizer and production of crystals with smaller d_{50} (compared to experiments without ultrasonic attenuation). It was proven that the uniformity of the product crystals and the width of their size distribution are directly related to the methods of producing the seed crystals. Further, it was proven that the characteristic crystal sizes are maintained over time during the process, thus a continuous production of crystals with reproducible size was facilitated.

6. An estimation of the mean sizes of L-glu crystals along the crystallizer height could be done with the Richardson-Zaki force balance model. The comparison of the calculated results with the experimentally determined mean crystal sizes shows good agreement. Moreover, studies on the influence of the different crystal shapes on the predictability of the model were conducted by performing experiments with different flow rates and inline measuring the development of the CSDs of the model substances L-asn.H₂O and OABA in the fluidized bed crystallizer. A validation of the model was achieved and it has shown good prediction capabilities in the case of L-asn.H₂O and an increasing diversity at higher flow rates for OABA, most probably due to crystal agglomeration. It is very difficult to predict and calculate the complex mass and heat flows within the bed. The proposed mathematical modelling is still simple and depends on various parameters, which are only experimentally available.
7. A pilot plant facility, consisting of two coupled FBCs was constructed with just one product outlet and operated. The parallel performance of the kinetically controlled continuous selective (“preferential”) crystallization of L-asn.H₂O and D-asn.H₂O as well as OABA and PABA in both crystallizers was realized and the process principles were demonstrated. Although strong agglomeration was observed in the case of OABA / PABA, high purities of all product crystals for both model systems were achieved. The productivity of the pilot plant facility varies with the type of the substance used, a steady and continuous production for several hours was achieved. A comparison with the coupled batch crystallizer setup reveals that the productivities of the continuous selective preferential crystallization process of enantiomers in both facilities are comparable.

8. A dynamical model considering the crystallization process in conjunction with the fluidized bed regime is proposed. The model takes care of the supersaturation generation with respect to solution concentration, temperature, crystal growth, and crystal segregation. The evaluation of the solution concentration development for both model systems was thus realized. Along with the prediction of the product CSD, the total time when the process is in steady state was predicted and proved good agreement with the experimental data.

A short recommendation can be implied for a possible expansion of the proposed empirical models, using them as basis for development of a more reliable mathematical model of the whole process, including solid-liquid equilibria equations, growth kinetics, crystallizer fluid dynamics models, and the complete simulation of the crystallizer set-up. Such project is already in progress and is supported by the German Research Foundation by the program emphasis “Dynamische Simulation vernetzter Feststoffprozesse”.

9. Suggestions for further improvements of the equipment are finally given, based on the results of the experimental study. Thus, further productivity enhancements appear to be possible.

References

- [Al-Dibouni1979] Al-Dibouni, M.R., Garside, J., Particle classification and mixing in liquid fluidized beds. *Trans. Inst. Chem. Eng.*, 1979, 57, 94–103.
- [Aldaco2006] Aldaco R., Garea A., Irabien A., Fluoride Recovery in a Fluidized Bed: Crystallization of Calcium Fluoride on Silica Sand, *Ind. Eng. Chem. Res.* 2006, 45, 796–802.
- [Apelblat1997] Apelblat A., Manzurola E., Solubilities of L-aspartic, DL-aspartic, DL-glutamic, p-hydroxybenzoic, o-anistic, p-anistic, and itaconic acids in water from T = 278 K to T = 345 K, *J. Chem. Thermodyn.*, 1997, 29, 1527–1533.
- [Apelblat2002] Manzurola E., Apelblat A., Solubilities of L-glutamic acid, 3-nitrobenzoic acid, p-toluic acid, calcium-L-lactate, calcium gluconate, magnesium-DL-aspartate, and magnesium-L-lactate in water, *J. Chem. Thermodyn.*, 2002, 34, 1127–1136.
- [Bari2014] Bari A., Pandit A., Ultrasound-Facilitated Particle Breakage: Estimation of Kinetic Parameters Using Population Balance Modelling, *Can. J. Chem. Eng.*, 2014, 9999, 1–7.
- [Battistoni1997] Battistoni P., Fava G., Pavan P., Musacco A., Cecchi F., Phosphate removal in anaerobic liquors by struvite crystallization without addition of chemicals: Preliminary results, *Wat. Res.*, 1997, 31(11), 2925–2929.
- [Bauer2001] Bauer J., Spanton S., Henry R., Quick J., Dziki W., Porter W., Morris J., Ritonavir: An Extraordinary Example of Conformational Polymorphism. *Pharmaceut. Res.*, 2001, 18(6), 859–866.
- [Beckmann2000] Beckmann W., Seeding the Desired Polymorph: Background, Possibilities, Limitations and Case Studies, *Org. Process Res. Dev.* 2000, 4(5), 372–383.
- [Beckmann2013] Beckmann W. (Ed.), *Crystallization: Basic Concepts and Industrial Applications*, Wiley-VCH, Weinheim, Germany, 2013.
- [Belcu1996] Belcu M., Turtoi D., Simulation of the fluidized bed crystallizers (I) influences of parameters, *Cryst. Res. Technol.*, 1996, 31, 1015–1023.
- [Bernstein2002] Bernstein J., *Polymorphism in Molecular Crystal*, Oxford University Press: New York, 2002.
- [Beyreuther2007] Beyreuther K., Biesalski H. K., Fernstrom J. D., Grimm P., Hammes W. P., Heinemann U., Kempfski O., Stehle P., Steinhart H., Walker R., Consensus meeting: monosodium glutamate – an update, *Eur. J. Clin. Nutr.*, 2007, 61, 304–313.
- [Binev2011a] Binev D., Lorenz H., Seidel-Morgenstern A., Crystal Size Distribution of L-Glutamic Acid In a Fluidized Bed Crystallizer, *Produktgestaltung in der Partikeltechnologie*, 2011, Bd. 5, 445–456.
- [Binev2011b] Binev D., Lorenz H., Seidel-Morgenstern A., Production of Crystals with Specific Size from L-Glutamic Acid in a Fluidized Bed Crystallizer, *Proceedings of 18th Int. Workshop on Industrial Crystallization (BIWIC 2011)*, Delft, 2011, 330–335.
- [Binev2012] Binev D., Lorenz H., Seidel-Morgenstern A., Enantiomer separation by preferential crystallization in coupled fluidized bed reactors, *Proceedings of 19th Int. Workshop on Industrial*

- [Borissova2009] Crystallization (BIWIC 2012), Tianjin, 2012, 87–94.
Borissova A., Khan S., Mahmud T., Roberts K. J., Andrews J., Dallin P., Chen Z.-P., Morris J., In Situ Measurement of Solution Concentration during the Batch Cooling Crystallization of L-Glutamic Acid using ATR-FTIR Spectroscopy Coupled with Chemometrics, *Cryst. Growth Des.*, 2009, 9(2), 692–706.
- [Braga2009] Braga D., Grepioni F., Maini L., Polito M., Crystal Polymorphism and Multiple Crystal Forms in: Structure and Bonding, ed. D. M. P. Mingos, Springer-Verlag Berlin Heidelberg, 2009.
- [Bransom1965] Bransom S. H., Continuous crystallizer design, *Chem. Proc. Eng.*, 1965, 46(12), 647–653.
- [Brown1985] Brown C. J., Ehrenberg M., Anthranilic acid, C₇H₇NO₂, by neutron diffraction, *Acta Crystallogr., Sect. C*, 1985, 41, 441–443.
- [Boone1977] Boone C. D. G., Derissen J. L., Schoone J. C., Anthranilic acid II (o-aminobenzoic acid), *Acta Crystallogr., Sect. B*, 1977, 33, 3205–3206.
- [Cahn1966] Cahn R. S., Ingold S. C., Prelog V., Specification of Molecular Chirality, *Angew. Chem. Int. Ed.*, 1966, 5(4), 385–415.
- [Chemspider222] <http://www.chemspider.com/Chemical-Structure.222.html>
- [Chemspider231] <http://www.chemspider.com/Chemical-Structure.231.html>
- [Chemspider591] <http://www.chemspider.com/Chemical-Structure.591.html>
- [Chemspider953] <http://www.chemspider.com/Chemical-Structure.953.html>
- [Chen2000] Chen J. P., Yu H., Lead removal from synthetic wastewater by crystallization in a fluidized-bed reactor, *J. Environ. Sci. Health., Part A*, 2000, 35(6), 817–835.
- [Collins1997] Collins A. N., Sheldrake G. N., Crosby J., Chirality in Industry II: Developments in the Manufacture and Applications of Optical Active Compounds, John Wiley & Sons, Chichester, 1997.
- [Cooney1970] Cooney D. A., Handschumacher R. E., L-Asparaginase and L-Asparagine metabolism, *Annu. Rev. Pharmacol.*, 1970, 10, 421–440.
- [Coppola1987] Coppola G. M., Schuster H. F., Asymmetric Syntheses, Construction of Chiral Molecules Using Amino Acids, John Wiley & Sons, New York, 1987.
- [Coquerel2007] Coquerel G., Preferential Crystallization, *Top. Curr. Chem.* 2007, 269, 1–51.
- [Crawhall1979] Crawhall J. C., Lecavaler D., Ryan P., Penicillamine, its metabolism and therapeutic applications: A review, *Biopharm. Drug. Dispos.*, 1979, 1, 73–95.
- [Czapla2008] Czapla F., Lorenz H., Seidel-Morgenstern A., Efficient design of preferential crystallization processes. In "17th International Symposium on Industrial Crystallization" – ISIC 17th, Maastricht, 2008, 803–810.
- [Czapla2010] Czapla F., Polenske D., Klukas L., Lorenz H., Seidel-Morgenstern A., Cyclic auto seeded polythermal preferential crystallization – Effect of impurity accumulation. *Chem. Eng. Process.*, 2010, 49, 22–28.
- [Dalton1933] Dalton J. B., Schmidt C. L. A., The solubilities of certain amino acids in water, the densities of their solutions at twenty-five degrees, and the calculated heats of solution and partial molal volumes, *J. Biol. Chem.*, 1933, 103, 549–578.
- [Dalton1935] Dalton, J. B., Schmidt C. L. A., The solubilities of certain amino acids and related compounds in water, the densities of their

References

- solutions at twenty-five degrees, and the calculated heats of solution and partial molal volume. II, *J. Biol. Chem.*, 1935, 109, 241–248.
- [DeCastro2007] De Castro M. D. L., Priego–Capote F., Ultrasound-assisted crystallization (sonocrystallization)., *Ultrason. Sonochem.* 2007, 14, 717.
- [Dennehy2003] Dennehy R. D., Particle Engineering Using Power Ultrasound, *Org. Process Res. Dev.*, 2003, 7, 1002–1006.
- [Elgarhy2006] Elgarhy K., The Separation of the Enantiomers of Asparagine by Crystallization, PhD Thesis, McGill University (Canada), 2006, ISBN 9780494251386.
- [Elsner2007] Elsner M. P., Ziomek G., Seidel–Morgenstern A., Simultaneous preferential crystallization in a coupled, batch operation mode—Part I: Theoretical analysis and optimization, *Chem. Eng. Sci.*, 2007, 62(17), 4760–4769.
- [Elsner2009] Elsner M. P., Ziomek G., Seidel–Morgenstern A., Efficient separation of enantiomers by preferential crystallization in two coupled vessels, *AIChE Journal*, 2009, 55(3), 640–649.
- [Elsner2011] Elsner M. P., Ziomek G., Seidel–Morgenstern A., Simultaneous preferential crystallization in a coupled batch operation mode, *Chem. Eng. Sci.*, 2011, 66(6), 1269–1284.
- [Epstein2003] Epstein, N., Applications of liquid–solid fluidization, *Int. J. Chem. Reactor Eng.*, 2003, 1, 1–16.
- [Ergun1949] Ergun S., Orning A. A., Fluid flow through randomly packed columns and fluidized beds, *Ind. Eng. Chem.*, 1949, 41(6), 1179–1184.
- [EU2011] http://ec.europa.eu/food/international/trade/docs/CU_SPS_requirements_customs_union_chap2_22_en.pdf
- [Fan1989] Fan L.S., Gas–Liquid–Solid Fluidization Engineering, Butterworths, Stoneham, 1989.
- [Filippone2002] Filippone S., Heimanna F., Rassat A., A highly water–soluble 2+1 b–cyclodextrin–fullerene conjugate, *Chem. Commun.*, 2002, 14, 1508–1509.
- [Formisani2001] Formisani B., De Cristofaro G., Girimonte R., A fundamental approach to the phenomenology of fluidization of size segregating binary mixtures of solids, *Chem. Eng. Sci.*, 2001, 56, 109–119.
- [Formisani2008] Formisani B., Girimonte R., Longo T., The fluidization process of binary mixtures of solids: Development of the approach based on the fluidization velocity interval, *Powder Technol.*, 2008, 185, 97–108.
- [Frances1994] Frances C., Biscans B., Laguerie, C., Modeling of a continuous fluidized–bed crystallizer. *Chem. Eng. Sci.* 1994, 49, 3269–3276.
- [Fritsche1839] J. Fritsche, Vorläufige Notiz über ein neues Zersetzungsprodukt des Indigo durch Salpetersäure, *J. Prakt. Chem. /Chem–Ztg*, 1839, 16(1), 507–508.
- [Gibbs1948] Gibbs J. W., Collected Works, Vol. 1 in: Thermodynamics, Yale University Press, New Haven, 1948.
- [Gibilaro2001] Gibilaro L. G., Fluidization Dynamics, Butterworth–Heinemann, Oxford, UK, 2001.
- [Glasby1968] Glasby J., Ridgway K., The crystallization of aspirin from ethanol, *J. Pharm. Pharmacol.*, 1968, 20, 94S–103S.
- [Gou2011] Gou L., Robl S., Leonhard K., Lorenz H., Sordo M., Butka A., Kesselheim S., Wolff M., Seidel–Morgenstern A., Schaber K., A

- hybrid process for chiral separation of compound-forming systems, *Chirality*, 2011, 23, 118–127.
- [Gracin2004] Gracin S., Rasmuson Å. C., Polymorphism and Crystallization of p-Aminobenzoic Acid, *Cryst. Growth Des.*, 2004, 4(5), 1013–1023.
- [Greenstein1961] Greenstein J. P., Winitz M., *Chemistry of the Amino Acids*, Wiley & Sons: New York, 1961.
- [He2005] He Y., Wu C., Kong W., Theoretical and Experimental Studies of Water Complexes of p- and o-Aminobenzoic Acid, *J. Phys. Chem. A*, 2005, 109(12), 2809–2815.
- [Heffels1999] Heffels S. K., Kind M., Seeding Technology: An Underestimated Critical Success Factor for Crystallization in Proceedings of the 14th International Symposium on Industrial Crystallization, Cambridge/U. K., 1999.
- [Heinrich2002] Heinrich S., Peglow M., Ihlow M., Henneberg M., Mörl L., Analysis of the start-up process in continuous fluidized bed spray granulation by population balance modelling, *Chem. Eng. Sci.*, 2002, 57(20), 4369–4390.
- [Hertweck2011] Hertweck C., Biosynthesis and charging of pyrrolysine, the 22nd genetically encoded amino acid, *Angew. Chem. Int. Ed.*, 2011, 50(41), 9540–9541.
- [Hill1999] Hill J. W., Petrucci R. H., *General Chemistry*, 2nd edition, Prentice Hall, 1999.
- [Hill1995] Hill P. J., Ng K. M., New discretization procedure for the breakage equation, *AIChE J.* 1995, 41(5), 1204–1216.
- [Hoffman1993] Hoffman A. C., Janssen L. P. M., Prins J., Particle segregation in fluidized binary mixtures, *Chem. Eng. Sci.*, 1993, 48(9), 1583–1592.
- [Hofmann2005] Hofmann G., Situation of Plant Construction in Industrial Crystallization – A Process Intensification, *VDI-Berichte* 1901, 2005, Bd. 2, 759–772.
- [Howley2002] Howley M. A., Glasser B. J., Hydrodynamics of a uniform liquid-fluidized bed containing a binary mixture of particles, *Chem. Eng. Sci.*, 2002, 57, 4209–4226.
- [Isaachsen1925] Isaachsen I., Jeremiassen F., Ein neues industrielles Kristallisierungs-verfahren, *Zeitsch. Ang. Chem.*, 1925, 38, 317–322.
- [Jacques1994] Jacques J., Collet A., Wilen S. H., *Enantiomers, Racemates, and Resolutions*, Krieger Publishing Company, Malabar, Florida, 1994.
- [Jiang2010] Jiang S., Jansens P. J., ter Horst J. H., Control over Polymorph Formation of o-Aminobenzoic Acid, *Cryst. Growth Des.*, 2010, 10(6), 2541–2547.
- [Jones2002] Jones A. G., *Crystallization process systems*, Butterworth-Heinemann, Oxford, UK, 2002.
- [Kaemmerer2013] Kaemmerer H., Seidel-Morgenstern A., Lorenz H., Chiral separation of systems of high eutectic composition by a combined process: Case study of serine enantiomers, *Chem. Eng. Process.*, 2013, 67, 71–79.
- [Kawai2012] Kawai M., Sekine-Hayakawa Y., Okiyama A., Ninomiya Y., Gustatory sensation of L- and D-amino acids in humans, *Amino Acids*, 2012, 43(6), 2349–2358.
- [Kee2009] Kee N. C. S., Tan R. B. H., Braatz R. D., Selective Crystallization of the Metastable r-Form of L-Glutamic Acid using Concentration

References

- [Khamskii1969] Feedback Control, *Cryst. Growth Des.*, 2009, 9(7), 3044–3051.
Khamskii E., Tybulewicz A., *Crystallization from Solution*, Consultants Bureau, New York, 1969.
- [Kofler1957] Kofler A., Delande N., Lacourt A., *Thermomicromethods for identification of glutamic acid antipodes*, *Microchem. J.*, 1957, 1(1), 55–57.
- [Kossel1934] Kossel W., *Zur Energetik von Oberflächenvorgängen*, *Annalen der Physik*, 1934, 21, 457–480.
- [Kuchinskas1957] Kuchinskas E. J., Horvath A., Du Vigneaud V., *An anti-vitamin B6 action of l-penicillamine*, *Arch. Biochem. Biophys.*, 1957, 68(1), 69–75.
- [Kusters1994] Kusters K. A., Pratsinis S. E., Thoma S. G., Smith D. M., *Energy Size Reduction Laws for Ultrasonic Grinding*, *Powder Technol.*, 1994, 80, 253–263.
- [Leitereg1971] Leitereg T. J., Guadagni D. G., Harris J., Mon T. R., Teranishi R., *Evidence for the Difference between the Odours of the Optical Isomers (+)- and (-)-Carvone*, *Nature*, 1971, 230, 455–456.
- [Leuchtenberger2005] Leuchtenberger W., Huthmacher K., Drauz K., *Biotechnological production of amino acids and derivatives: current status and prospects*, *Appl. Microbiol. Biotechnol.* 2005, 69, 1–8.
- [Levilain2010] Levilain G., Coquerel G., *Pitfalls and rewards of preferential crystallization*, *Cryst. Eng. Comm.*, 2010, 12, 1983–1992.
- [Li1997] Li Z. J., Grant D. J. W., *Relationship between physical properties and crystals structures of chiral drugs*, *J. Pharm. Sci.*, 1997, 86, 1073–1078.
- [Lindenberg2011] Lindenberg C., Mazzotti M., *Continuous precipitation of L-asparagine monohydrate in a micromixer: Estimation of nucleation and growth kinetics*, *AIChE Journal*, 2011, 57(4), 942–950.
- [Liu2002] Liu M., Sibi M. P., *Recent advances in the stereoselective synthesis of β -amino acids*, *Tetrahedron*, 2002, 58(40), 7991–8035.
- [Lorenz2006a] Lorenz H., Perlberg A., Sapoundjiev D., Elsner M. P., Seidel-Morgenstern A., *Crystallization of enantiomers*, *Chem. Eng. Process.*, 2006, 45, 863–873.
- [Lorenz2006b] Lorenz H., Polenske D., Seidel-Morgenstern A., *Application of preferential crystallization to resolve racemic compounds in a hybrid process*, *Chirality*, 2006, 18(10), 828–840.
- [Lorenz2011] Lorenz H., Ulrich J., *Meißener Klausurtagung, Positionierung des Fachausschusses Kristallisation zu Zukunftsthemen*. *Chem. Ing. Tech.*, 2011, 83, 2089–2092.
- [Lorenz2013] Lorenz H., *Solubility and Solution Equilibria in Crystallization*, in Beckmann W. (Ed.), *Crystallization: Basic Concepts and Industrial Applications*, Wiley-VCH, Weinheim, Germany, 2013, 35–74.
- [Maier2007] Maier N. M., Lindner W., *Chiral recognition applications of molecularly imprinted polymers: a critical review*, *Anal. Bioanal. Chem.*, 2007, 389(2), 377–397.
- [Maki2000] Maki T., Takeda K., *Benzoic Acid and Derivatives*, *Ullmann's Encyclopedia of Industrial Chemistry.*, 2000, 5, 329–341.
- [Marković2008] Marković S., Mitrić M., Starčević G., Uskoković D., *Ultrasonic de-agglomeration of barium titanate powder*, *Ultrason. Sonochem.*, 2008, 15, 16–20.
- [Matz1964] Matz G., *Untersuchungsmethoden für die klassifizierende Kristallisation*, *Wärme*, 1964, 70(3), 99–107.

- [Mayer2004] Meyer V. R., Practical High-performance Liquid Chromatography, 4th ed., John Wiley and Sons, 2004.
- [Meierhenrich2008] Meierhenrich U., Amino Acids and the Asymmetry of Life, Springer-Verlag, Berlin Heidelberg, 2008.
- [Mersmann2001] Mersmann A., Crystallization technology handbook, 2ed, Marcel Dekker Inc., New York, 2001.
- [Midler1970] Midler M., Production of Crystals in a Fluidized Bed with Ultrasonic Vibrations, United States Patent 3510266, 1970.
- [Midler1975] Midler M., Process for Production of Crystals in Fluidized Bed Crystallizers, United States Patent No. 3892539, 1975.
- [Midler1976] Midler M., Crystallization System and Method Using Crystal Fracturing External to a Crystallization Column, No. 3996018, 1976.
- [Miller1999] Miller M. T., Strömmand K., Teratogen update: thalidomide: a review, with a focus on ocular findings and new potential uses, *Teratology*, 1999, 60, 306–321.
- [Mougin2002] Mougin P., Wilkinson D., In Situ Measurement of Particle Size during the Crystallization of L-Glutamic Acid under Two Polymorphic Forms: Influence of Crystal Habit on Ultrasonic Attenuation Measurements, *Cryst. Growth Des.*, 2002, 2(3), 227–234.
- [Mullin1970] Mullin J. W., Nývlt J., Design of classifying crystallizers, *Trans. Inst. Chem. Eng.*, 1970, 48, T7–T14.
- [Mullin2001] Mullin J. W., Crystallization, Oxford, Butterworth-Heinemann, 4ed, 2001.
- [Myerson2001] Myerson A. S. (Ed.), Handbook of Industrial Crystallization, 2ed, Elsevier, Oxford, 2001.
- [Ndzié1998] Ndzié E., Cardinael P., Petit M.-N., Coquerel G., Enantiomeric resolution of (\pm)-5-ethyl-5-methylhydantoin by means of preferential nucleation, *Enantiomer*, 1998, 4, 97–101.
- [Nienow1980] Nienow A.W., Naimer N.S., Continuous mixing of two particulate species of different density in a gas fluidized bed, *Trans. Inst. Chem. Eng.*, 1980, 58, 181–186.
- [Noyes1897] Noyes A. A., Whitney W. R., Rate of solution of solid substances in their own solution, *J. Am. Chem. Soc.*, 1897, 19, 930–934.
- [Nývlt1970] Nývlt J., Mullin J. W., The periodic behaviour of continuous crystallizers, *Chem. Eng. Sci.*, 1970, 25(1), 131–147.
- [Ogawa2009] Ogawa K., Matsui J., Suzuki E., Doki N., Shimizu K., Orientation and Surface Topography of L-Alanine Crystals in Fluidized-Bed Crystallizer in a Magnetic Field, *J. Chem. Eng. Jpn.*, 2009, 42(12), 878–883.
- [Omar2003] Omar W., Ulrich J., Influence of crystallization conditions on the mechanism and rate of crystal growth of potassium sulphate, *Cryst. Res. Technol.*, 2003, 38(6), 34–41.
- [Orella1991] Orella C. J., Kirwan D. J., Correlation of Amino Acid Solubilities in Aqueous Aliphatic Alcohol Solutions, *Ind. Eng. Chem. Res.*, 1991, 30, 1040–1045.
- [Palis2013] Palis S., Binev D., Lorenz H., Seidel-Morgenstern A., Kienle A., Population balance modeling of crystallization in a fluidized bed, Proceedings of 20th Int. Workshop on Industrial Crystallization (BIWIC2013), Odense, Denmark, 2013, 252–259.
- [Patel2009] Patel S. R., Murthy Z. V. P., Ultrasound assisted crystallization for the recovery of lactose in an anti-solvent acetone, *Cryst. Res.*

References

- Technol., 2009, 44(8), 889–896.
- [Patil2008] Patil M. N., Gore G. M., Pandit A. B., Ultrasonically controlled particle size distribution of explosives: a safe method, *Ultrason. Sonochem.* 2008, 15, 177–187.
- [Paul2005] Paul E. L., Tung H. H., Midler M., Organic crystallization processes. *Powder Tech.*, 2005, 150, 133–143.
- [Perry1997] Perry R. H., Green D. W., *Perry's Chemical Engineers' Handbook*, 7th ed., New York: McGraw–Hill, 1997.
- [Plaitakis2001] Plaitakis A., Zaganas I., Regulation of human glutamate dehydrogenases: Implications for glutamate, ammonia and energy metabolism in brain, *J. Neurosci. Res.*, 2001, 66(5), 899–908.
- [Plazanet2006] Plazanet M., Dean M., Merlini M., Hüller A., Emerich H., Meneghini C., Johnson M. R., Trommsdorff H. P., Crystallization on heating and complex phase behavior of α -cyclodextrin solutions, *J. Chem. Phys.* 2006, 125(15), 154504.
- [Polenske2009] Polenske D., Lorenz H., Seidel–Morgenstern A., Potential of different techniques of preferential crystallization for enantioseparation of racemic compound forming systems, *Chirality*, 2009, 21, 728–737.
- [Predel1982] Predel B., *Heterogene Gleichgewichte – Grundlagen und Anwendungen*, Steinkopff Verlag, Darmstadt, 1982.
- [Rahaman2014] Rahaman M. S., Mavinic D. S., Meikleham A., Modeling phosphorus removal and recovery from anaerobic digester supernatant through struvite crystallization in a fluidized bed reactor, *Water Research*, 2014, 51, 1–10.
- [Raman2011] Raman V., Abbas A., Zhu W., Particle grinding by high-intensity ultrasound: Kinetic modeling and identification of breakage mechanisms, *AIChE J.*, 2011, 57(8), 2025–2035.
- [Randolph1988] Randolph A. D., Larson M. A., *Theory of particulate processes*, 2nd ed., Academic Press, San Diego, 1988.
- [Richardson1954] Richardson J. F., Zaki W. N., Sedimentation and fluidisation. Part 1, *Trans. Inst. Chem. Eng.*, 1954, 32, 35–53.
- [Robinson1987] Robinson M. R., Coyle J. T., Glutamate and related acidic excitatory neurotransmitters: from basic science to clinical application, *FACEB J.*, 1987, 446–455.
- [Roozeboom1899] Roozeboom H. W. B., Löslichkeit und Schmelzpunkt als Kriterien für razemische Verbindungen, pseudorazemischen Mischkristalle und inaktive Kongomere, *Z. Phys. Chem.*, 1899, 28, 494.
- [Ruecroft2005] Ruecroft G., Hipkiss D., Ly T., Macted N., Cains P. W., Sonocrystallization: the use of ultrasound for improved industrial crystallization. *Org. Process Res. Dev.*, 2005, 9, 923–932.
- [Kaspereit2008] Seidel–Morgenstern A., Keßler L. C., Kaspereit M., New Developments in Simulated Moving Bed Chromatography, *Chem. Eng. Technol.* 2008, 31(6), 826–837.
- [Scoog2007] Scoog D. A., Holler F. J., Crouch S. R., *Principles of Instrumental Analysis*, 6ed., Thomson Brooks/Cole, Canada, 2007.
- [Seebach2011] Petrusevska–Seebach K., Seidel–Morgenstern A., Elsner M. P., Preferential Crystallization of L–Asparagine in Water, *Cryst. Growth Des.*, 2011, 11(6), 2149–2163.
- [Seibert1998] Seibert K. D., Burns M. A., Simulation of Structural Phenomena in Mixed–Particle Fluidized Beds, *AIChE*, 1998, 44(3), 528–537.
- [Sheldon1990] Sheldon R., Industrial synthesis of optically active compounds, *Chem Ind.*, 1990, 7, 212–219.

- [Shiau2001] Shiau L. D., Lu T. S., Interactive effects of particle mixing and segregation on the performance characteristics of a fluidized bed crystallizer, *Ind. Eng. Chem. Res.*, 2001, 40, 707–713.
- [Shiau1999] Shiau L. D., Cheng S. H., Liu Y. C., Modeling of a fluidized bed crystallizer operated in a batch mode. *Chem. Eng. Sci.*, 1999, 54, 865–871.
- [Sistla2011] Sistla Venkata S., von Langermann J., Lorenz H., Seidel–Morgenstern A., Analysis and Comparison of Commonly Used Acidic Resolving Agents in Diastereomeric Salt Resolution – Examples for DL–Serine., *Cryst. Growth Des.*, 2011, 11(9), 3761–3768.
- [Soderberg2012] Soderberg T., *Organic Chemistry with a Biological Emphasis Vol. I*, University of Minnesota, Morris, 2012.
- [Svärd2010] Svärd M., Nordström F. L., Jasnobulka T., Rasmuson A. C., Thermodynamics and Nucleation Kinetics of *m*–Aminobenzoic Acid Polymorphs, *Cryst. Growth Des.*, 2010, 10, 195–204.
- [Swernath2013] Swernath S., Kaspereit M., Kienle A., Dynamics and Control of Coupled Continuous Chromatography and Crystallization Processes for the Production of Pure Enantiomers, *Chem. Eng. Technol.*, 2013, 36(8), 1417–1429.
- [Tai1999] Tai C. Y., Chien W. C., Chen C. Y., Crystal growth kinetics of calcite in a dense fluidized–bed crystallizer, *AIChE J.*, 1999, 45, 1605–1614.
- [Takara2005] Takara M., Ito A. S., General and Specific Solvent Effects in Optical Spectra of *ortho*–Aminobenzoic Acid, *Journal of Fluorescence*, 2005, 15(2), 171–177.
- [Takazawa1986] Takazawa H., Ohba S., Saito Y., Structure of monoclinic *o*–aminobenzoic acid, *Acta Crystallogr., Sect. C*, 1986, 42, 1880–1881.
- [Tammel2014] Tammel E., unpublished results from joint work, 2014.
- [Tavare1990] Tavare N.S., Matsuoka M., Garside J, Modelling a continuous column crystallizer: dispersion and growth characteristics of a cooling section. *J. Cryst. Growth*, 1990, 99, 1151–1155.
- [Teipel2002] Teipel U., Mikonsaari I., Size Reduction of Particulate Energetic Material, *Propellants, Explosives, Pyrotechnics*, 2002, 27, 168–174.
- [Tripathi1996] Tripathi G. N. R., Su Y., Spectroscopic and kinetic properties of the radical zwitterion and related intermediates in the one–electron oxidation of *p*–aminobenzoic acid., *J. Am. Chem. Soc.*, 1996, 118(9), 2235–2244.
- [Tung2009] Tung H. H., Paul E. L., Midler M. Jr., McCauley A., *Crystallization of Organic Compounds: An Industrial Perspective*, Wiley, Hoboken, New Jersey, 2009.
- [Vauquelin1806] Vauquelin L. N., Robiquet P. J., La découverte d'un nouveau principe végétal dans le suc des asperges, *Annales de Chimie*, 1806, 57, 88–93.
- [Vironea2006] Vironea C., Kramer H. J. M., van Rosmalen G. M., Stoop A. H., Bakker T. W., Primary nucleation induced by ultrasonic cavitation, *J. Crystal Growth*, 2006, 294, 9–15.
- [Vragov1999] Vragov A. P., Simulating and designing cylinder–cone classifying crystallizers, *Chem. Pet. Eng.*, 1999, 35(4), 189–198.
- [Wadell1933] Wadell H., Sphericity and Roundness of Rock Particles, *J. Geol.*, 1933, 41(3), 310–331.

References

- [Wang2012] Wang S., Guo S., Gao J., Lan X., Dong Q., Li X., Simulation of flow behavior of liquid and particles in a liquid–solid fluidized bed, *Powder Technol.*, 2012, 224, 365–373.
- [Wattanakit2014] Wattanakit C., Côme Y. B. S., Lapeyre V., Bopp P. A., Heim M., Yadnum S., Nokbin S., Warakulwit C., Limtrakul J., Kuhn A., Enantioselective recognition at mesoporous chiral metal surfaces, *Nat. Commun.*, 2014, 5, 1–8.
- [WHO1994] World Health Organization (WHO), *Fluorides and Oral Health*, Geneva, 1994.
- [Winkler1926] Winkler F., *Verfahren zur Herstellung von Wassergas*, DRP437970, 1926.
- [Xie2008] Xie R., Chu L.–Y., Deng J.–G., Membranes and membrane processes for chiral resolution, *Chem. Soc. Rev.*, 2008, 37, 1243–1263.
- [Xu2002] Xu R., *Particle Characterization: Light Scattering Methods*, Kluwer Academic Publishers, Moscow, 2002.
- [Yamada2005] Yamada T., Terashima T., Okubo T., Juneja L. R., Yokogoshi H., Effects of theanine, *r*–glutamylethylamide, on neurotransmitter release and its relationship with glutamic acid neurotransmission, *Nutr. Neurosci.*, 2005, 8(4), 219–226.
- [Yang2003] Yang W. C. (ed.), *Handbook of Fluidization and Fluid–Particle Systems*, Marcel Dekker Inc., New York, 2003.
- [Yokota2006] Yokota M., Doki N., Shimizu K., Chiral Separation of a Racemic Compound Induced by Transformation of Racemic Crystal Structures: DL-Glutamic Acid, *Cryst. Growth Des.*, 2006, 6(7), 1588–1590.
- [Zeiger2011] Zeiger B. W., Suslick K. S., Sonofragmentation of Molecular Crystals, *J. Am. Chem. Soc.*, 2011, 133(37), 14530–14533.
- [Zhang2009] Zhang Y., Ren B., Jin B., Xiao R., Zhong W., Characterization of Fluidization and Segregation of Biomass Particles by Combining Image Processing and Pressure Fluctuations Analysis, *Int. J. Chem. React. Eng.*, 2009, 7, A81.

Nomenclature

Symbols

A	component A
A	surface or cross-sectional area (m^2)
A	absorbance in eq. 3.7 (a.u.)
a	constant in eq. 3.3 (-)
AB	solution of component A and component B
AxBy	solid solution of component A in component B
Ar	Archimedes number (-)
BxAy	solid solution of component B in component A
B	component B
B°	nucleation rate (-)
b	constant in eq. 3.3 (-)
c	solution concentration (g/kg, wt.%)
c^*	solution concentration at equilibrium (g/kg, wt.%)
c_i	interfacial concentration (g/kg, wt.%)
C	component C (-)
C	number of independent components (-)
C_D	drag coefficient (-)
D	dextrorotatory enantiomer
D	diffusion coefficient (-)
DL	racemic mixture
d	crystallizer diameter (m)
d_{50}	mean particle diameter (m)
E	eutectic point
E_a	activation energy (kJ mol^{-1})
ee	enantiomer excess (%)
F	number of degrees of freedom (-)
f	frequency (Hz)
f_b	Archimedean buoyancy force (kg m s^{-1})
f_d	total drag force (kg m s^{-1})
F_d	complete drag force for all flow regimes (kg m s^{-2})

Nomenclature

f_e	particle effective force (kg m s^{-1})
f_p	fluid-particle interaction force (kg m s^{-1})
g	standard gravity (m s^{-2})
G	Gibbs free energy (J or J mol^{-1})
G	linear growth rate (m s^{-1})
H	fluidized bed crystallizer height (m)
I	transmitted intensity ($\text{W}\cdot\text{m}^{-2}$)
I_0	intensity of the light at a given wavelength ($\text{W}\cdot\text{sr}^{-1}\cdot\text{m}^{-1}$)
K_c	measuring cell constant in eq. 3.3 (-)
$K\epsilon$	extinction coefficient in eq. 3.7 (-)
k_n	nucleation rate constant (-)
k_d	coefficient of mass transfer by diffusion (-)
K_G	overall crystal growth coefficient (-)
k_m	coefficient of mass transfer (-)
k_r	rate constant of for the surface reaction (-)
L	levorotatory enantiomer
L	crystal size (m)
l	length of the sample tube in eq. 3.4 (m)
l_s	path length through the sample in eq. 3.7 (m)
m	mass (kg)
m_t	tube mass in eq. 3.3 (kg)
n	particle number distribution (-)
\dot{n}	particle flux (m s^{-1})
n_A	mole amount of component A (mol)
n_i	mole amount of component i (mol)
n_{RZ}	Richardson-Zaki parameter (-)
N	particle quantity (-)
P	number of phases (-)
P	peritectic point
R	universal gas constant ($\text{J mol}^{-1} \text{K}^{-1}$)
Re_p	Reynolds number (-)
R_G	overall crystal growth rate ($\text{kg m}^{-2} \text{s}^{-1}$)
r_c	critical size of a nuclei (m)
S	solvent
S	supersaturation (-)

SD_T	standard temperature deviation ($^{\circ}\text{C}$, K)
T	temperature ($^{\circ}\text{C}$, K)
T_o	oscillation period (s)
\bar{T}	mean temperature ($^{\circ}\text{C}$, K)
T_s	temperature of solution at equilibrium ($^{\circ}\text{C}$, K)
T_N	temperature of nucleation ($^{\circ}\text{C}$, K)
T_c	temperature of crystallization ($^{\circ}\text{C}$, K)
t	time (h)
u_f	fluid superficial velocity (m s^{-1})
u_p	particle segregation velocity (m s^{-1})
\dot{V}	flow rate ($\text{m}^3 \text{s}^{-1}$)
V_{sus}	suspension volume (m^3)
V_{cr}	total crystallizer volume (m^3)
V_t	tube volume in eq. 3.3 (m^3)
W_e	particle effective weight (kg m s^{-2})
wt. %	weight percent (g g^{-1} in %)
x	height along the fluidized bed crystallizer (mm)
x_m	height of the fluidized bed crystallizer, where conical part ends (mm)
x_p	product outlet height of the fluidized bed crystallizer (mm)

Greek symbols

α	optical rotation ($^{\circ}$)
$[\alpha]_Y^T$	specific optical rotation in eq. 3.4 ($^{\circ}$)
δ	Dirac delta distribution (-)
Δc	concentration driving force (g/kg, wt. %)
ΔG	change in Gibbs free energy (J)
ΔG_{crit}	critical change in free energy (J)
ΔP	unrecoverable pressure loss ($\text{kg m}^{-1} \text{s}^{-1}$)
ε	void fraction (-)
μ_f	fluid viscosity (Pa s)
ρ_f	fluid density (kg m^{-3})
ρ_p	particle density (kg m^{-3})
τ	residence time (s)
τ_{US}	mean residence time in the ultrasonic bath (s)

Nomenclature

σ	relative supersaturation (-)
γ	interfacial tension or surface energy (J m^{-2})
γ	wavelength in eq. 3.5 (m)
Ψ	sphericity factor (-)
χ_A	mole fraction of component A (-)
χ_B	mole fraction of component B (-)
χ_C	mole fraction of component C (-)

Indices

bm	back mixing
cg	crystal growth
cr	crystallizer
eff	effective
f	fluid (solution)
g	'order' of the overall crystal growth
i	component i
j	'order' of the overall nucleation rate
in	to the crystallizer from the ultrasonic bath
n	Richardson and Zaki parameter
out	from the crystallizer to the ultrasonic bath
p	particle
s	solid
T	specific temperature
seg	segregation
us	ultrasonic

Abbreviations

ABA	aminobenzoic acid
CSD	crystal size distribution
D-asn.H ₂ O	D-asparagine monohydrate
DL-asn.H ₂ O	DL-asparagine monohydrate
D-glu	D-glutamic acid
DL-glu	DL-glutamic acid
EtOH	Ethanol

FBC	fluidized bed crystallizer
FBRM	Focused Beam Reflectance Measurement
H ₂ O	water
HCOOH	methanoic acid (formic acid)
HPLC	High-Performance Liquid Chromatography
L-asn.H ₂ O	L-asparagine monohydrate
L-glu	L-glutamic acid
MeOH	methanol
MSZW	metastable zone width
OABA	<i>ortho</i> -aminobenzoic acid
PABA	<i>para</i> -aminobenzoic acid
PBE	population balance equation
PSD	particle size distribution
TG-DSC	thermogravimetric differential scanning calorimetry
US	ultrasonic
XRPD	X-ray powder diffraction

Temperature programs, used for determination of MSZW and solubility equilibria.

Temperature program 1

1. Heating the suspension to 60°C (or over the expected saturation temperature).
2. Waiting at 60°C for 10 min (to dissolve the remaining solid).
3. Cooling the solution to 10°C with a rate of 3 K/h.
4. Keeping the suspension at 10°C for 30 min (to equilibrate the suspension).
5. Heating the suspension to 60°C with a rate of 3 K/h.

Temperature program 2

1. Heating the suspension to 40°C.
2. Waiting at 40°C for 10 min.
3. Cooling the solution to 5°C with a rate of 3 K/h.
4. Keeping the suspension at 5°C for 30 min.
5. Heating the suspension to 40°C with a rate of 3 K/h.

Temperature program 3

1. Heating the suspension to 50°C.
2. Waiting at 50°C for 10 min.
3. Cooling the solution to 35°C with a rate of 20 K/h.
4. Cooling the solution to 5°C with a rate of 3 K/h.
5. Keeping the suspension at 5°C for 30 min.
6. Heating the suspension to 50°C with a rate of 3 K/h.

The reproducibility of the measurements was studied carrying out at least 3 experiments under same conditions (or same temperature program).

$$SD_T = \sqrt{\frac{1}{N-1} \sum_{i=1}^N (T_i - \bar{T})^2} \quad (\text{A1.1})$$

In the equation, the standard deviation of the saturation temperature SD_T is given, where $\{T_1, T_2, \dots, T_N\}$ are the observed temperature values for each measurement and \bar{T} is the mean value of these observations.

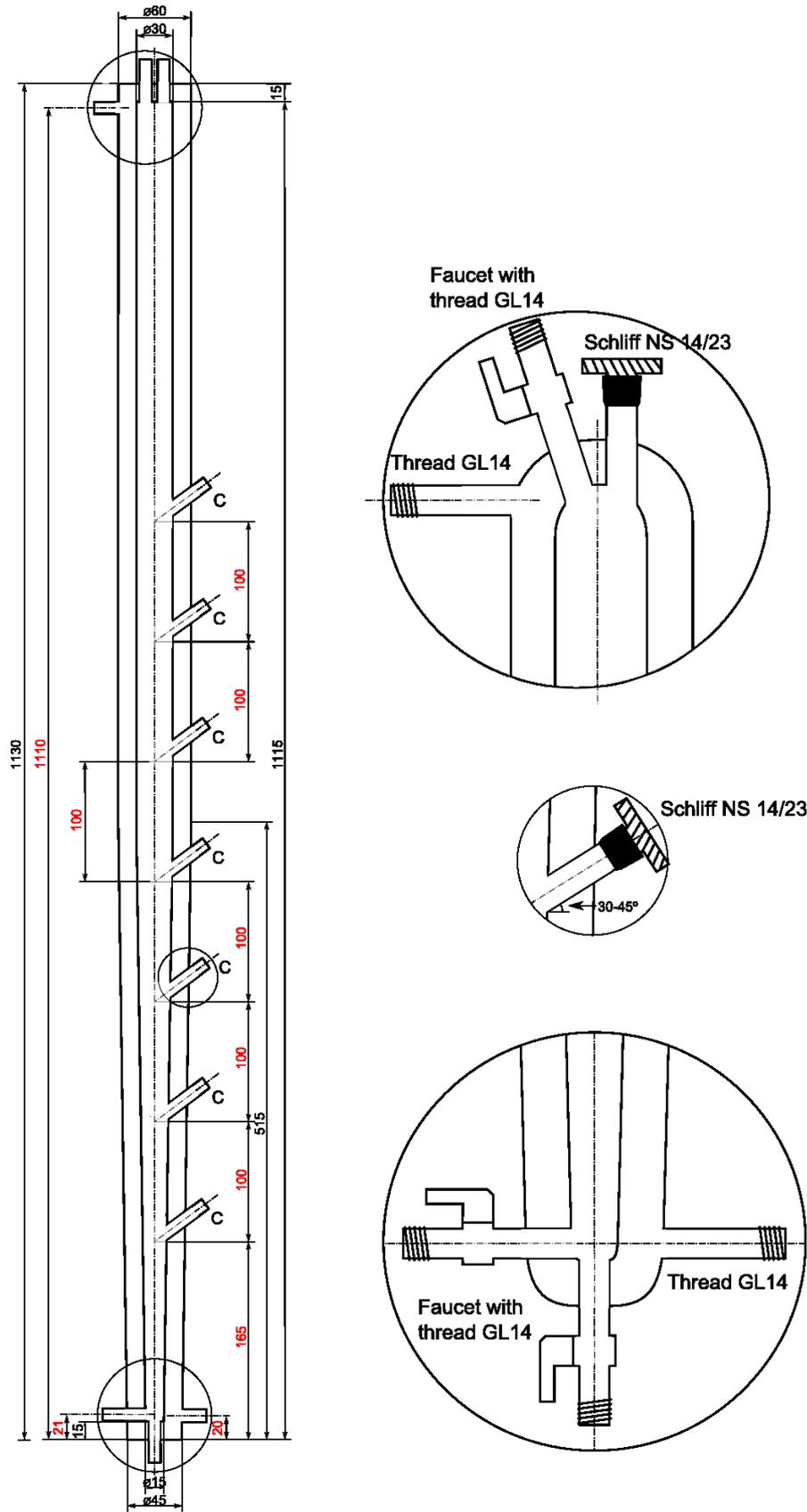


Fig. A1.1 Scheme of a fluidized bed crystallizer with seven product outlets along its height

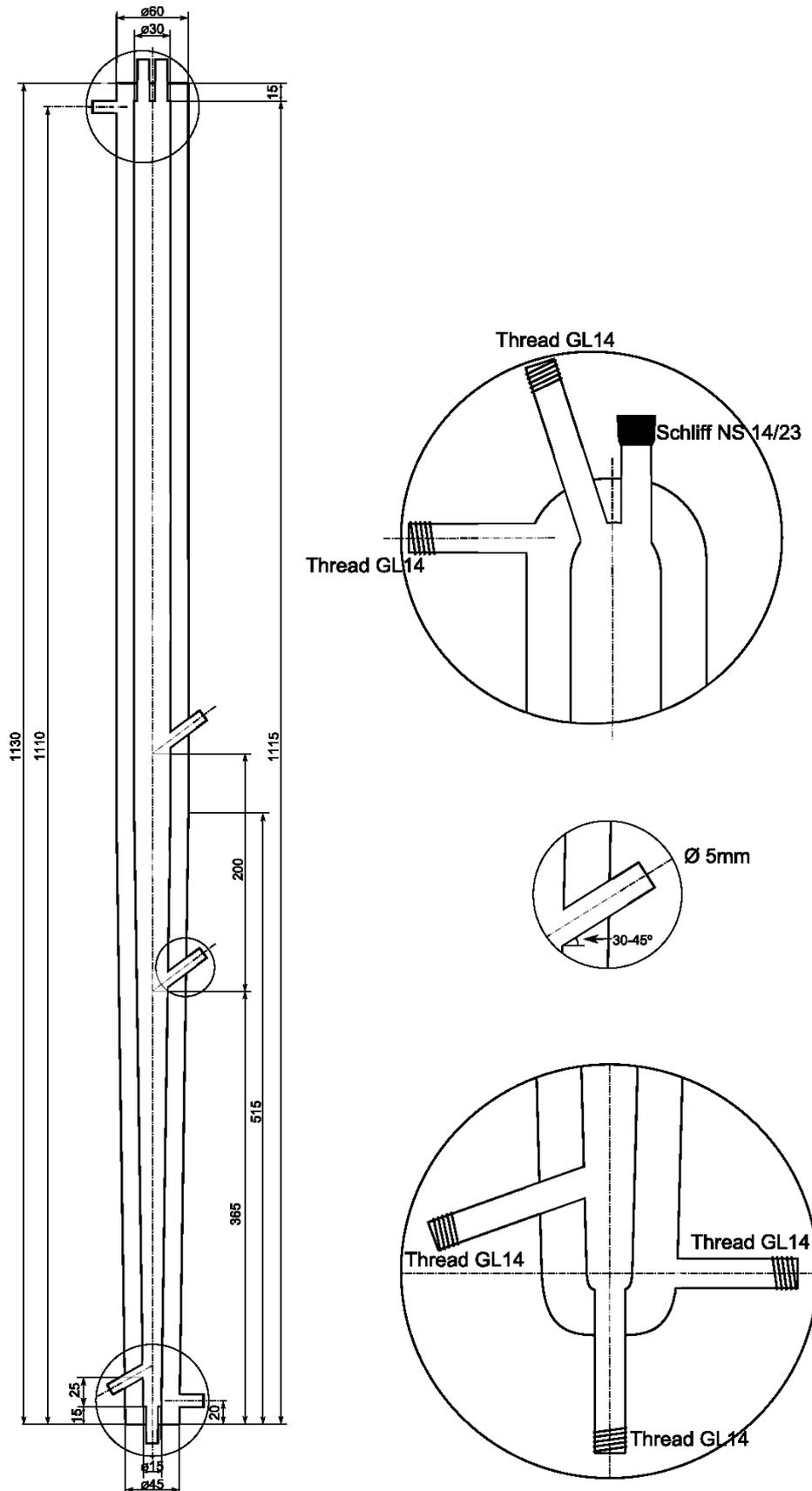


Fig. A1.2 Scheme of a fluidized bed crystallizer, used in the coupled FBC-equipment.

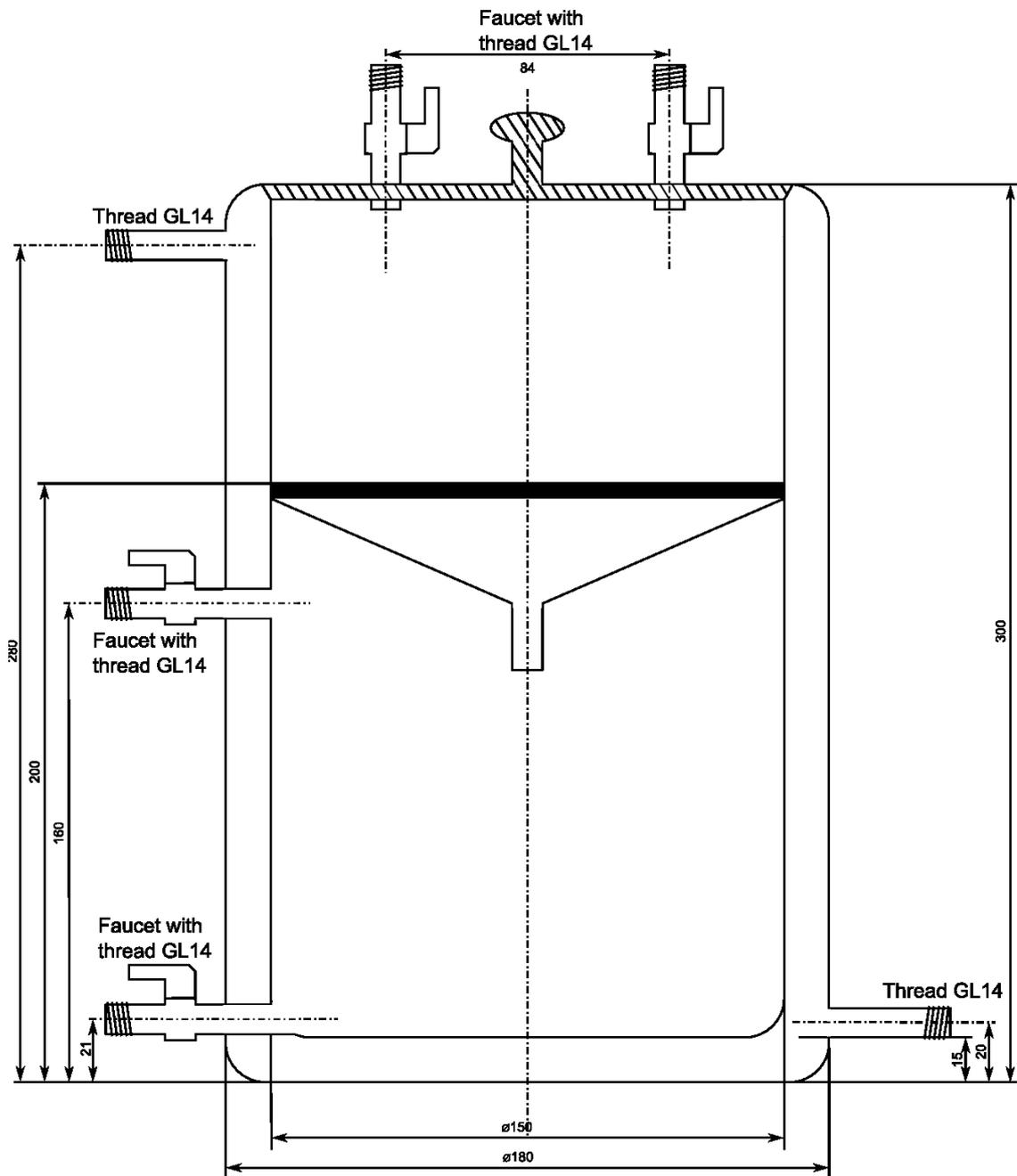


Fig. A1.3 Scheme of the vacuum filter

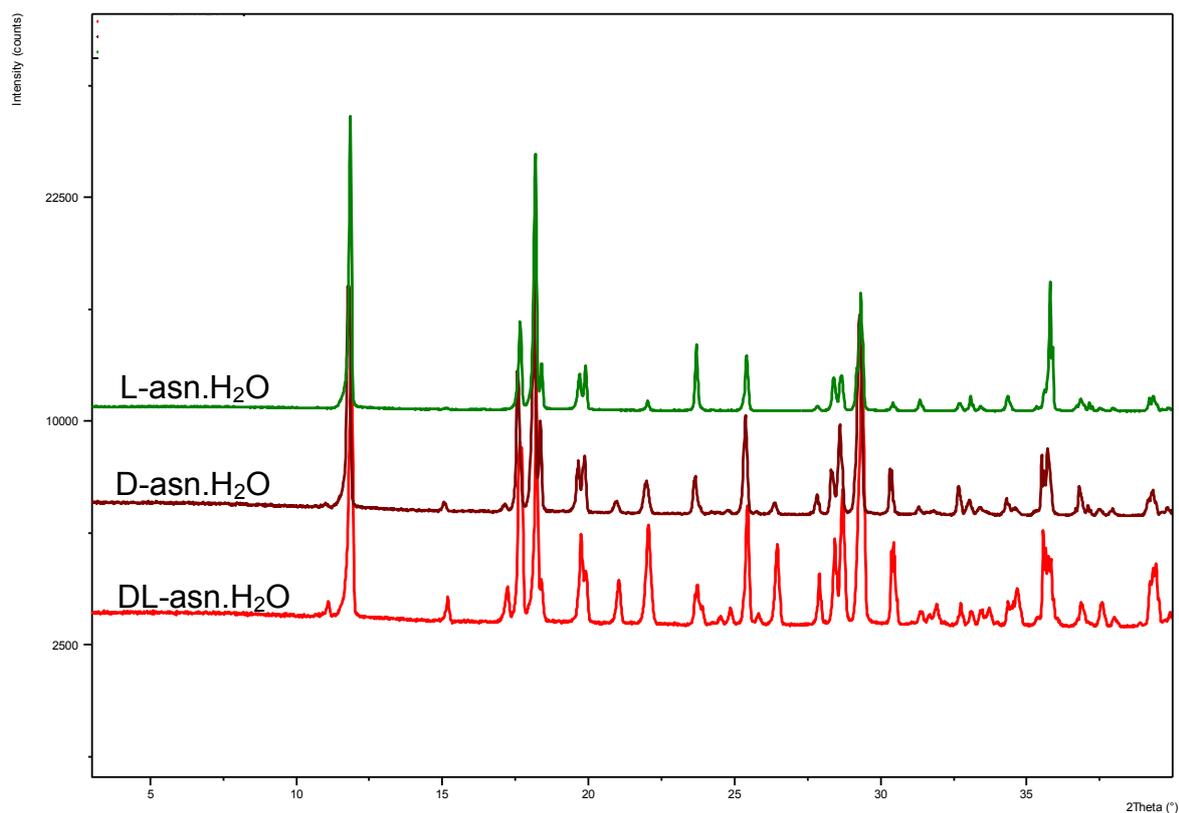


Fig. A2.1 XRPD pattern of asparagine enantiomers and racemate

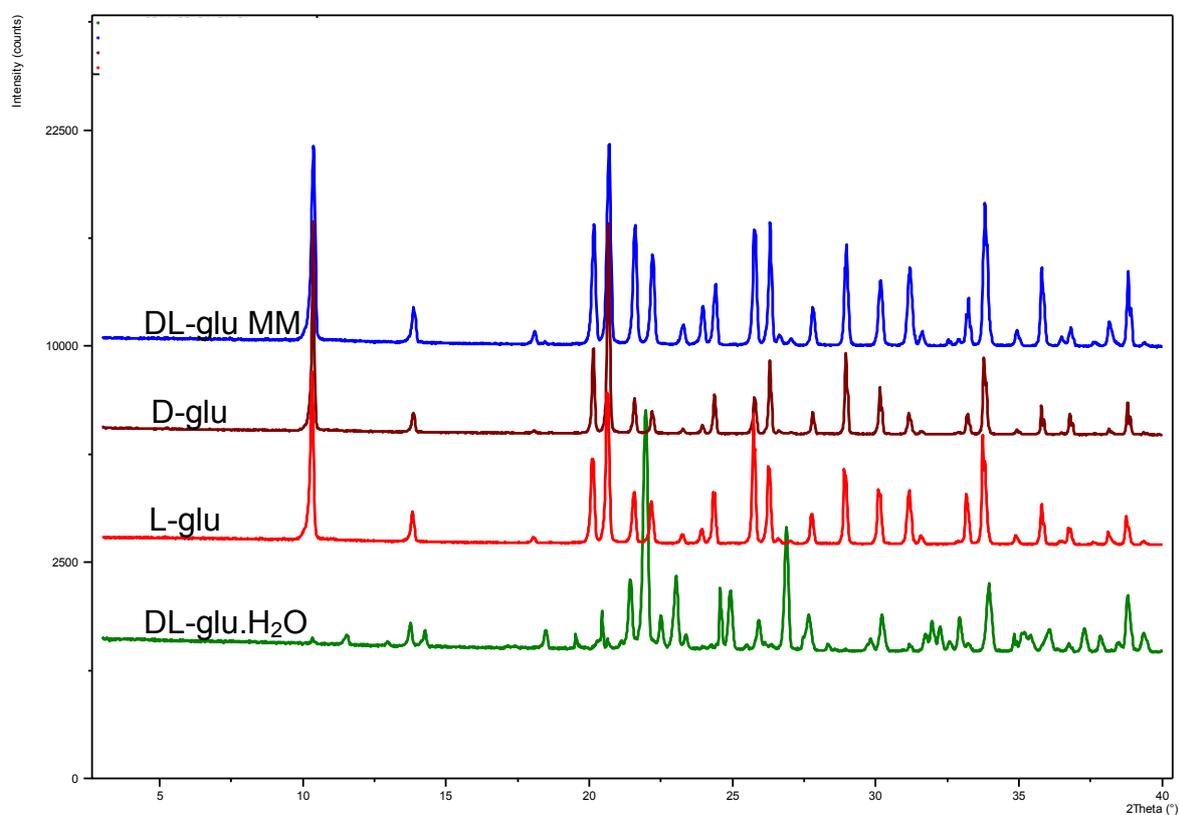


Fig. A2.2 XRPD pattern of glutamic acid enantiomers, a 50:50 mechanical mixture of both enantiomers and a racemic compound, which is monohydrate

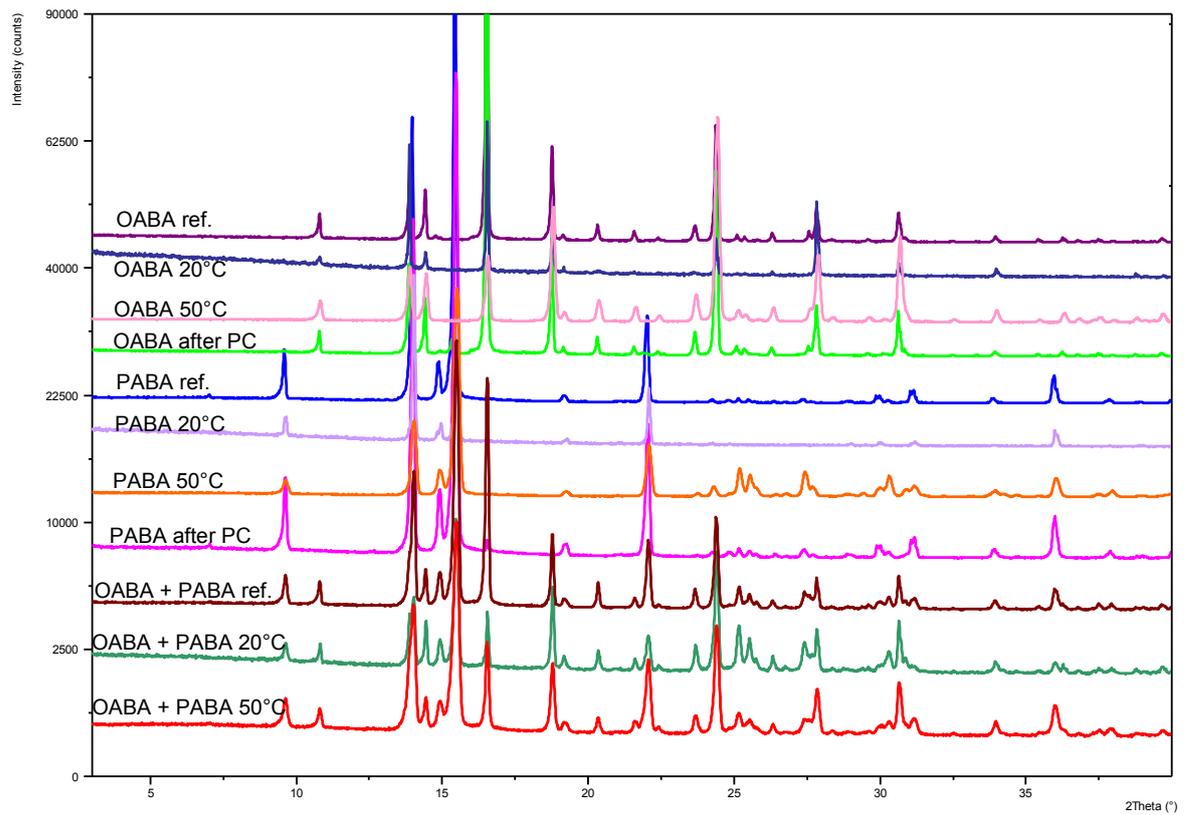


Fig. A2.3 XRPD patterns of: OABA, PABA, and 50:50 mechanical mixtures of OABA and PABA, crystals produced at 20°C and 50°C. Crystals from the respective storage container measured as reference. XRPD patterns of product crystals of OABA and PABA from the continuous preferential crystallization are also shown.

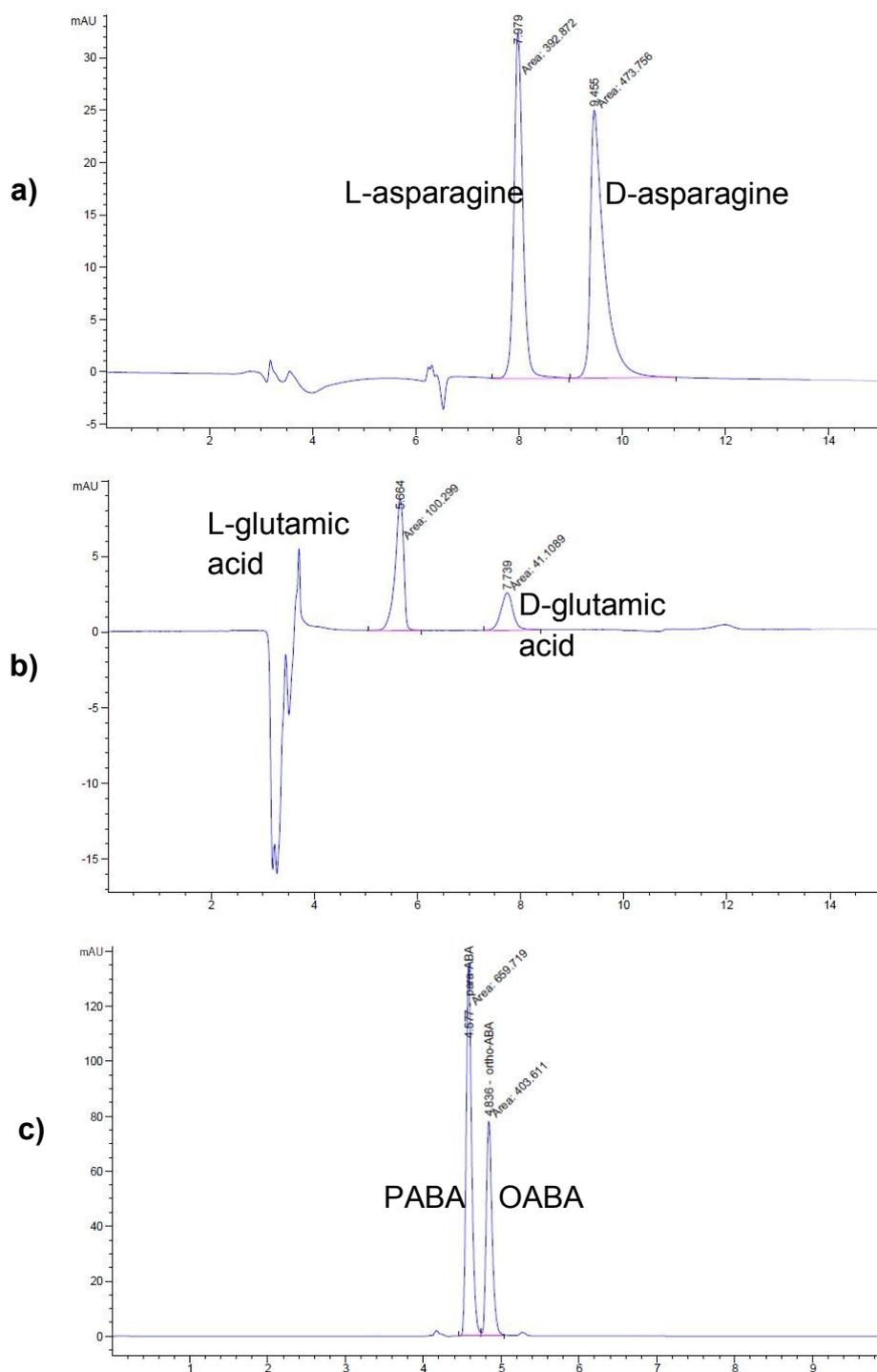


Fig. A2.4 HPLC measurements of aqueous solutions of:

- a) DL-asparagine
- b) DL-glutamic acid
- c) A 50:50 mixture of OABA and PABA